Homogeneous Rotating Turbulence

Inverse Energy Cascade and the Dissipation Scaling Law

Pestana, T.

DOI
10.4233/uuid:d3e7f749-08a3-47a8-a3a3-22fe90b5df4e

Publication date
2020

Document Version
Final published version

Citation (APA)
Pestana, T. (2020). *Homogeneous Rotating Turbulence: Inverse Energy Cascade and the Dissipation Scaling Law*. [Dissertation (TU Delft), Delft University of Technology]. https://doi.org/10.4233/uuid:d3e7f749-08a3-47a8-a3a3-22fe90b5df4e

Homogeneous Rotating Turbulence

Inverse Energy Cascade and the Dissipation Scaling Law

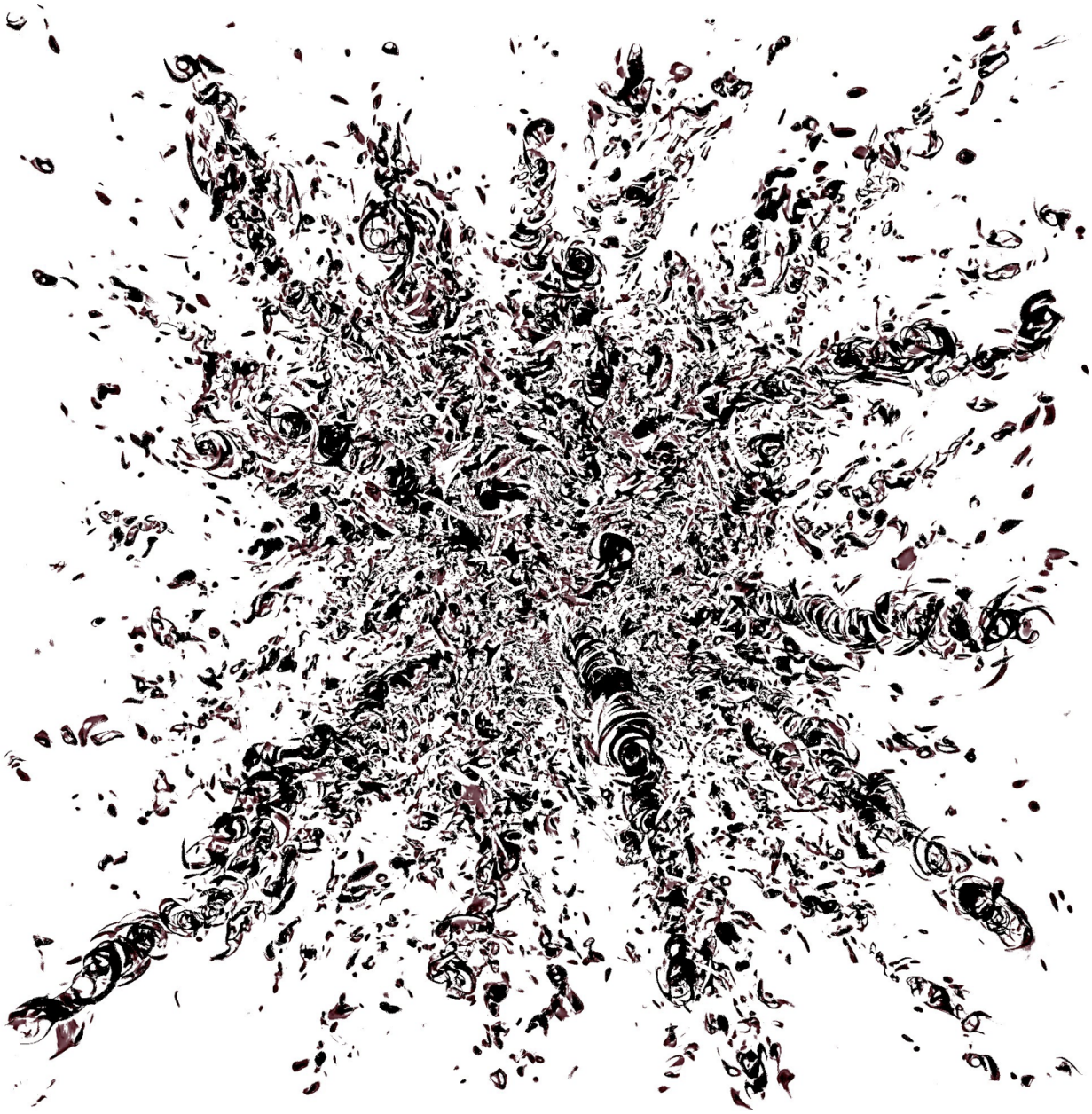

Tiago Cabral Santos Pestana

Homogeneous Rotating Turbulence

Inverse Energy Cascade and the Dissipation Scaling Law

Tiago CABRAL SANTOS PESTANA

Homogeneous Rotating Turbulence

Inverse Energy Cascade and the Dissipation Scaling Law

Proefschrift

ter verkrijging van de graad van doctor
aan de Technische Universiteit Delft,
op gezag van de Rector Magnificus prof. dr. ir T.H.J.J. van der Hagen
voorzitter van het College voor Promoties,
in het openbaar te verdedigen op
Donderdag 3 September 2020 om 15:00 uur

door

Tiago CABRAL SANTOS PESTANA

Master of Science in Mechanical Engineering,
Karlsruher Institut für Technologie, Germany
geboren te Salvador, Bahia, Brazilië

Dit proefschrift is goedgekeurd door de

promotor: Prof. Dr.-Ing. habil. S. Hickel

Samenstelling promotiecommissie:

Rector Magnificus	voorzitter
Prof. Dr.-Ing. habil. S. Hickel	Technische Universiteit Delft
Onafhankelijke leden:	
Prof. dr. B. Boersma	Technische Universiteit Delft
Prof. Dr.-Ing. habil. M. Oberlack	Darmstadt University of Technology, Germany
Prof. dr. C. Vuik	Technische Universiteit Delft
Dr. A. Alexakis	École Normale Supérieure, France
Dr. F. Godeferd	École Centrale de Lyon, France
Dr. S. Hulshoff	Technische Universiteit Delft
Reservelid:	
Prof. dr. D. von Terzi	Technische Universiteit Delft

Keywords: Turbulence, Homogeneous Rotating flows, Energy Cascade

Cover: Top view of a strong rotating turbulent flow illustrating the prevalence of columnar flow structures

ISBN 978-94-6366-306-9

Printed by Rijnja Repro, Delft

An electronic version of this dissertation is available at
http://repository.tudelft.nl/.

To the memory of my uncle César
a symbol of humbleness and a true source of inspiration

Contents

Samenvatting

Dit proefschrift bestudeert fundamentele aspecten van atmosferische turbulentie door middel van direct numerieke simulaties van homogene roterende turbulentie en van een brekende traagheid-zwaartekrachtgolf in de middelste atmosfeer. De numerieke experimenten werden uitgevoerd met een nieuwe computationele tool, specifiek ontworpen voor dit onderzoek en bedoeld om te profiteren van massaal parallel verwerking op supercomputer hardware.

Ten eerste is de overgang van een gespleten naar een voorwaarts kinetisch energie cascade systeem onderzocht in de context van homogene roterende turbulentie met een driedimensionale isotrope willekeurige kracht die niet gecorreleerd is met het snelheidsveld. De parametrische studie behandelt begrenzing effecten in domeinen met grote aspectverhoudingen, die in de draairichting ongeveer 340 keer groter zijn dan de typische initiële wervelgrootte, en een breed scala aan rotatiesnelheden. De huidige gegevens voegen substantieel toe aan eerdere werken, die daarentegen gericht waren op kleinere en ondiepere domeinen. Resultaten geven aan dat voor vaste geometrische afmetingen het Rossby nummer als controle parameter fungeert, terwijl voor een vast Rossby nummer het product van de domeingrootte langs de rotatie-as met het forcerende golfgetal de hoeveelheid energie regelt die gedeeltelijk omgekeerd wordt overgedragen. Onze resultaten laten zien dat het criterium voor regime overgang afhangt van beide controle parameters.

Ten tweede, met behulp van de vorige database, twee aspecten van homogeen roterende turbulentie worden gekwantificeerd. Door de tijdevolutie van de integrale lengteschaal langs de rotatie-as $\ell_\parallel$ te volgen, de groeisnelheid van de zuilvormige wervelingen en zijn afhankelijkheid van het Rossby nummer Ro_ε wordt bepaald als $\gamma = 3.90\exp(-16.72\,Ro_\varepsilon)$ voor $0.06 \leq Ro_\varepsilon \leq 0.31$ waarbij γ de niet-dimensionale groeisnelheid is. Daarna wordt een schaalwet voor de energie dissipatie snelheid ε_ν gezocht. Een vergelijking met de huidige beschikbare schaalwetten laten zien dat de relatie die voorgesteld wordt door Baqui & Davidson (2015), namelijk $\varepsilon_\nu \sim u'^3/\ell_\parallel$, waarbij u' de r.m.s. snelheid is, onze gegevens gedeeltelijk goed benadert, daarbij specifiek in het bereik $0.39 \leq Ro_\varepsilon \leq 1.54$. Echter, de voorgestelde relaties in de literatuur slagen er niet in de gegevens te modelleren voor het tweede en meest interessante bereik, namelijk $0.06 \leq Ro_\varepsilon \leq 0.31$, die gekenmerkt zijn door de formatie van zuilvormige wervels. Om een overeenkomstige relatie te vinden voor het laatste, maken wij gebruik van het concept van een spectrale overdrachtstijd die geïntroduceerd is door Kraichnan (1965). Binnen dit kader wordt de energie dissipatie snelheid beschouwd af te hangen aan zowel de niet-lineaire tijdschaal als de ontspanningstijdschaal. Dus door onze gegevens te analyseren zijn uitdrukkingen voor deze verschillende tijdschalen verkregen die resulteren in $\varepsilon_\nu \sim u'^4/(\ell_\perp^2\, Ro_\varepsilon^{0.62} \tau_{nl}^{\mathrm{iso}})$, waarbij $\ell_\perp$ de integrale lengteschaal is in de richting loodrecht op de draaias, en τ_{nl}^{iso} de niet-lineaire tijdschaal is van het initiële homogene isotrope veld.

Ten derde onderzoeken we een testcase waarin rotatie- en stratificatie-effecten gecombineerd optreden. Daarom simuleren we traagheidszwaartekrachtgolven die in de midden-bovenste mesosfeer breken, namelijk op hoogtes die overeenkomen met het Reynolds nummer van 28 647 en 114 591 die gebaseerd zijn op de golflengte en de periode geassocieerd met het opwaartse drijfvermogen. Terwijl het eerste al bestudeerd is door Remmler *et al.* (2013), wordt deze hier herhaald met een hogere resolutie en dient als basis voor vergelijking met de hoge Reynolds nummer testcase. De simulaties zijn ontworpen op basis van de studie van Fruman *et al.* (2014), en worden geïnitialiseerd door optimale verstoringen bovenop de onstabiele convectieve basisgolf te plaatsen. Binnen één golfperiode, vergankelijke groei leidt tot een bijna onmiddellijke golfbreking en secundaire uitbarsting van turbulentie. We laten zien dat dit proces gekenmerkt wordt door de vorming van fijnstroomstructuren die zich voornamelijk in de omgeving bevinden van het minst stabiele punt van de golf. Tijdens de golfafbraak, de energie dissipatie snelheid neigt naar een isotrope tensor, terwijl dit sterk anisotropisch is tussen de brekende gebeurtenissen. We vinden dat de verticale kinetische energie spectra een duidelijke 5/3 schaalwet vertonen bij instanties van intensieve energie dissipatie snelheid en een kubieke machtswet in rustigere periodes. Het term-voor-term energiebudget laat zien dat de drukterm de belangrijkste bijdrage levert aan het globale energiebudget, aangezien het de verticale en horizontale kinetische energie koppelt. Tijdens de brekende gebeurtenissen is de lokale energieoverdracht voornamelijk van het gemiddelde tot het fluctuerende veld en de kinetische energie productie is in evenwicht met de pseudo-kinetische energie dissipatie snelheid. De laatstgenoemde studie is gericht op de gecombineerde effecten van rotatie en stratificatie.

Summary

This thesis studies fundamental aspects of atmospheric turbulence through direct numerical simulations of homogeneous rotating turbulence and of an inertia-gravity wave breaking in the middle atmosphere. The numerical experiments were performed with a new computational tool designed for the sole purpose of this research and meant to take advantage of massively parallel processing on supercomputer hardware.

First, transition from a split to a forward kinetic energy cascade system is explored in the context of homogeneous rotating turbulence with a three-dimensional isotropic random force uncorrelated with the velocity field. The parametric study covers confinement effects in large aspect ratio domains, which is in the direction of rotation about 340 times larger than the typical initial eddy size, and a broad range of rotation rates. The present data adds substantially to previous works, which, in contrast, focused on smaller and shallower domains. Results indicate that for fixed geometrical dimensions the Rossby number governs the amount of energy that cascades inversely, whereas for a fixed Rossby number the product of the domain size along the rotation axis and forcing wavenumber acts as the control parameter. Our results show that the regime transition criterion depends on both control parameters.

Second, using the previous database, two aspects of homogeneous rotating turbulence are quantified. By following the time evolution of the integral lengthscale along the axis of rotation $\ell_\parallel$, the growth rate of the columnar eddies and its dependency on the Rossby number Ro_ε is determined as $\gamma = 3.90\exp(-16.72\,Ro_\varepsilon)$ for $0.06 \leq Ro_\varepsilon \leq 0.31$ where γ is the non-dimensional growth rate. Then, a scaling law for the energy dissipation rate ε_ν is sought. A comparison with current available scaling laws shows that the relation proposed by Baqui & Davidson (2015), i.e., $\varepsilon_\nu \sim u'^3/\ell_\parallel$, where u' is the r.m.s. velocity, approximates well part of our data, more specifically the range $0.39 \leq Ro_\varepsilon \leq 1.54$. However, relations proposed in the literature fail to model the data for the second and most interesting range, i.e., $0.06 \leq Ro_\varepsilon \leq 0.31$, which is marked by the formation of columnar eddies. To find a similarity relation for the latter, we exploit the concept of a spectral transfer time introduced by Kraichnan (1965). Within this framework, the energy dissipation rate is considered to depend on both the nonlinear timescale and the relaxation timescale. Thus, by analyzing our data, expressions for these different time-scales are obtained that results in $\varepsilon_\nu \sim u'^4/(\ell_\perp^2 Ro_\varepsilon^{0.62}\tau_{nl}^{\mathrm{iso}})$, where $\ell_\perp$ is the integral lengthscale in the direction normal to the axis of rotation and τ_{nl}^{iso} is the nonlinear timescale of the initial homogeneous isotropic field.

Third, we explore a test case where rotation and stratification effects appear combined. Therefore, we simulate inertia-gravity waves breaking in the middle-upper mesosphere, namely at altitudes which correspond to the Reynolds number of

28 647 and 114 591 based on wavelength and buoyancy period. While the former was studied by Remmler *et al.* (2013), it is here repeated at a higher resolution and serves as a baseline for comparison with the high Reynolds number case. The simulations are designed based on the study of Fruman *et al.* (2014), and are initialized by superimposing primary and secondary perturbations to the convectively unstable base wave. Transient growth leads to an almost instantaneous wave breaking and secondary bursts of turbulence. We show that this process is characterized by the formation of fine flow structures that are predominantly located in the vicinity of the wave's least stable point. During the wave breakdown, the energy dissipation rate tends to be an isotropic tensor, whereas it is strongly anisotropic in between the breaking events. We find that the vertical kinetic energy spectra exhibit a clear 5/3 scaling law at instants of intense energy dissipation rate and a cubic power law at calmer periods. The term-by-term energy budget reveals that the pressure term is the most important contributor to the global energy budget, as it couples the vertical and the horizontal kinetic energy. During the breaking events, the local energy transfer is predominantly from the mean to the fluctuating field and the kinetic energy production is in balance with the pseudo kinetic energy dissipation rate.

1

Introduction

If it works once, it's a trick.
If it works twice, it's a method.
If it works three times, it's a law.

Source Unknown

1

1.1. The Study of Turbulent Flows

The word turbulence is often used to describe situations full of commotion and it appears in different contexts. For instance, we may all have heard the expression "a turbulent life" as a synonym for a life marked by accidents and unplanned events. Or, the reader might be familiar with the term "turbulent financial market", which basically means economists can not accurately predict the future. In fluid mechanics, the field we deal with in this thesis, the term turbulent flows has been coined to describe the chaotic multiscale motion of fluids (gases and liquids). Like everything in life, it also has a contrary, namely laminar flows, which symbolizes the calm fluid motion, just like the water flow in the Dutch canals.

The laws governing fluid motion were first revealed in 1822 by C.L. Navier and later shown to be valid for a number of experiments by G.G. Stokes (see Dugas (2012) for details of the historical facts). However, knowing the governing equations was not sufficient. The rules which fluids obey were found, but the reason for specific flow behavior could not be inferred directly from the rules. Due to nonlinearities in the equations of motion, solutions were only found for elementary problems. It was then not until the experiments by Reynolds (1883), roughly 60 years later, that the notion of *direct* (now referred to as laminar) and a *sinuous* (now referred to as turbulent) flow stream was clarified. In that seminal work, O. Reynolds introduced what today is known as the Reynolds number and pinpointed that the different flow regimes are a consequence of the balance between the inertial and the viscous forces.

In nature, as well as in most engineering systems, we are more likely to find turbulent flows, i.e., situations in which the inertial forces prevail over the viscous forces. The importance of turbulent flows is therefore utmost. It has driven the curiosity of many researches and paved the way to a number of discoveries. Situations in which turbulent flows are encountered range from simple things in our daily lives to more complicated ones which are harder to grasp. Classical examples are the ones of stirring a cup of coffee or blowing out a strike-anywhere match (Fig. 1.1a). More sophisticated examples are found in the atmosphere and oceans of planets

(a) (b)

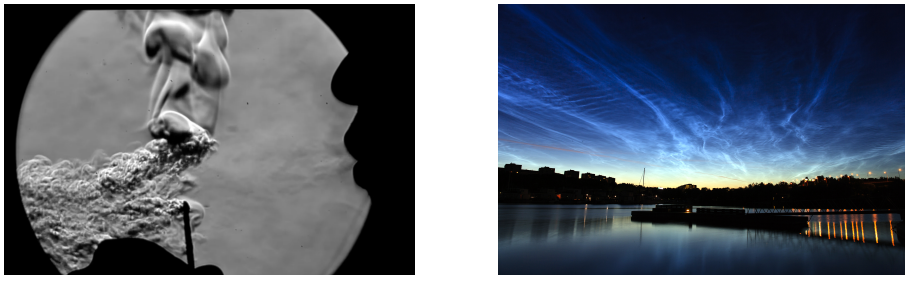

Figure 1.1: (a) A strike-anywhere match being blown out; the image shows the interaction of turbulent structures from the air and the flame itself (Miller *et al.*, 2014). (b) Polar meshosperic clouds (aka Noctilucent clouds) over the sky of Solna (Stockholm/Sweden) showing turbulence in the atmosphere.

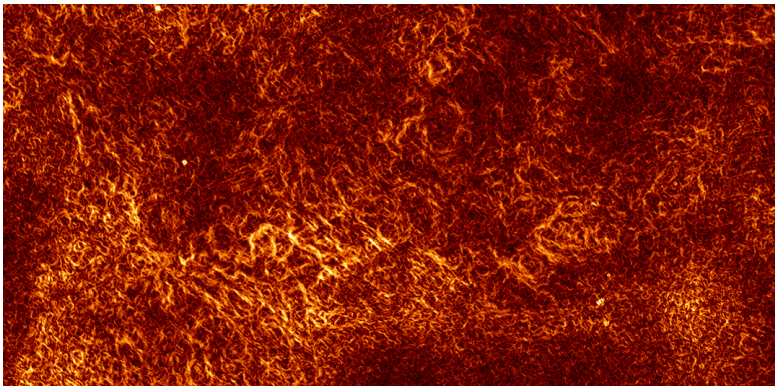

Figure 1.2: Turbulent gas in the interstellar medium of the Milky Way. The picture shows regions of intense density and magnetic field variations. (Gaensler *et al.*, 2011).

(e.g., on Earth Fig. 1.1b), where turbulence promotes mixing and influences the climate and the dynamics of oceanic currents; or in the cosmos (Fig. 1.2), where turbulence is vital for sustaining magnetic fields. Incidentally, we can still mention turbulent flows over surfaces (viscous boundary layers), which occurs in any kind of transportation system we may think of (e.g., boats, cars and airplanes).

Similarly to other fields in science, turbulence is studied by both theoreticians and experimentalists. Progress in this field, however, is slow and often smoothed out over the years, with major breakthroughs far from being the rule. Advances are accomplished by small victories and the big wins follow from contributions of different parties. For a good part of the 20th century, the scientific community experienced great advances towards an universal turbulence theory. During this time, progress was mainly led by the outburst of ideas from the Russian School (see e.g., Davidson *et al.* (2011) for a historical overview), which is nowadays probably best known due to the work of A. N. Kolmogorov. Unfortunately, an universal theory of turbulence has not emerged, and the question whether one even exists remains open. Currently, advances in this field are powered by a continuous technical progress, which allows for improved measurement techniques and unprecedented computational power — although at the cost of new programming paradigms. This has enabled the scientific community to harvest unprecedented data, both numerically and in laboratories, which can help elucidate unsolved problems and unveil new flow physics.

By envisioning the potential of computers in the study of turbulence, R. Kraichnan and S. Orszag were the pioneers in what today is called Direct Numerical Simulations (DNS) — see e.g. Orszag & Patterson (1972) for the first simulations of fluid turbulence. In this kind of experiment, numerical techniques are employed to accurately solve the laws of motion. Whereas classical experiments provide measurements of the real world, and can always be argued to represent in some sense reality, there is no doubt that numerical experiments have contributed (and will continue) to understanding the underlying physics of turbulent flows. In fact, nu-

merical and experimental techniques complement each other. Whereas the former can provide highly accurate temporal and spatial data, the latter can, for example, probe flows at much higher Reynolds number.

In this thesis, we deal with a very small part of this vast and exciting field. In particular, we focus our attention mainly on flow physics that can potentially lead to a better comprehension of atmospheric and oceanic flows. Our plan of attack relies exclusively on a computational approach that employs highly accurate and state-of-the-art numerical techniques for solving the equations of motion. In the following, we give a brief overview of the fundamentals of rotating flows. The experienced reader can skip ahead to Section 1.3, where we present the aim and outline this thesis.

1.2. Fundamentals of Rotating Flows

1.2.1. Preliminaries

Whether in engineering, geophysical or in astrophysical flows, rotation can influence and shape fluid motion. In engineering systems, classical examples of rotating flows are found in turbomachinery, like in wind/water turbines, or in turbofan reactors where rotation rates are as high as 10^5rpm (Godeferd & Moisy, 2015). In geophysical flows, it is planetary rotation that engenders the atmosphere and the ocean of planets with special traits and characteristic coherent structures. On Earth, hurricanes are perhaps the simplest example of the consequences of a rotating atmosphere. But a rotating atmosphere is not limited to our rock. On Jupiter, the dynamics induced by rotation are often called to explain the existence of a persistent red spot in its atmosphere. And, on icy moons like Enceladus, the effects of rotation are also important for the mixing of saline oceans that are conjectured to exist; there is hope that some sort of life could be found in these oceans.

The rules that govern the motion of incompressible fluids in an inertial frame of reference and in the absence of external forces are given by

$$\nabla \cdot \mathbf{u} = 0 \tag{1.1}$$

$$\frac{\partial \mathbf{u}}{\partial t} + \nabla \cdot (\mathbf{u} \otimes \mathbf{u}) = -\nabla p + \nu \nabla^2 \mathbf{u}, \tag{1.2}$$

where $\mathbf{u}$ is the fluid's velocity, t denotes time, p is the hydrodynamic pressure normalized by the fluid's constant density ρ, ν is the kinematic viscosity, and $\otimes$ denotes the dyadic product. Strictly speaking, these laws could be applied anywhere, as long as we obey the condition that the observer rests upon an inertial frame of reference. Obeying this condition, however, is not an easy task. For instance, since our planet is continuously rotating (with a period of $T_{earth} = 86\,400\,\mathrm{s}$), any motion on its frame of reference is continuously accelerated, and therefore it does not qualify as an inertial frame of reference. Thus, depending on the problem of interest, it might be convenient to consider non-inertial frames of reference and the above laws (Eqs. (1.1) and (1.2)) must be corrected to include the so-called *fictious* or *inertial* forces (see Appendix A for the mathematical details).

In a frame rotating with angular velocity $\mathbf{\Omega}$, there are two *fictitious* forces: the Coriolis and the centrifugal force. Under these conditions, Eqs. (1.1) and (1.2) become

$$\nabla \cdot \mathbf{u} = 0 \tag{1.3}$$

$$\frac{\partial \mathbf{u}}{\partial t} + \nabla \cdot (\mathbf{u} \otimes \mathbf{u}) + 2(\mathbf{\Omega} \times \mathbf{u}) = -\nabla q + \nu \nabla^2 \mathbf{u}, \tag{1.4}$$

in which, the Coriolis force appears explicitly added to the left-hand-side of Eq. (1.4) through the cross product between the angular velocity and the fluid's velocity, and the centrifugal force has been written in form of a potential and combined with the hydrodynamic pressure to yield the reduced pressure

$$q = p - \frac{\Omega R^2}{2}. \tag{1.5}$$

In the equation above, Ω is the norm of the angular velocity $\mathbf{\Omega}$, and R is the shortest distance to the axis of rotation. Whereas the centrifugal force acts in the plane of motion and pulls the fluid elements outward, the Coriolis force acts perpendicularly to the plane containing the axis of rotation and the velocity vector, and deflects the motion of the fluid particles. The centrifugal force depends only on the angular velocity of the frame and on the distance between the fluid particle and the axis of rotation; it does not introduce kinematic changes and it simply modifies the existing pressure field without altering the velocity field (cf. Eq. (1.5)). The Coriolis force, on the other hand, is the one that imparts different dynamics to incompressible rotating flows.

Although for the reason cited above any motion occurring on Earth takes place in a rotating frame of reference, depending on the scales of the physical process of interest, the influence of Earth's rotation can be neglected. This statement is clarified if the equations of motion are made non-dimensional by defining characteristic scales of motion such as a velocity scale u_0 and a lengthscale l_0. By introducing these quantities, Eqs. (1.3) and (1.4) can be alternatively written as

$$\nabla \cdot \mathbf{u}^* = 0 \tag{1.6}$$

$$\frac{\partial \mathbf{u}^*}{\partial t^*} + \nabla \cdot (\mathbf{u}^* \otimes \mathbf{u}^*) + \frac{1}{Ro}(\mathbf{e}_\Omega \times \mathbf{u}^*) = -\nabla q^* + \frac{1}{Re}\nabla^2 \mathbf{u}^*, \tag{1.7}$$

where the star as superscript denotes non-dimensional quantities. The Reynolds and the Rossby numbers, which are the two non-dimensional numbers governing the problem, appear naturally in Eq. (1.7) and are (for now and without specifying u_0 and l_0) defined as

$$Re = \frac{u_0 l_0}{\nu} \quad \text{and} \quad Ro = \frac{u_0}{2\Omega l_0}. \tag{1.8}$$

The Rossby number, named after the Swedish meteorologist Carl-Gustaf Arvid Rossby, represents the ratio between the timescale for fluid motion $t_f = l_0/u_0$ and the timescale induced by the system's rotation $\tau_\Omega = 1/\Omega$. For large Ro, i.e., $\tau_\Omega \gg t_f$, the fluid particles move as if in a fixed frame of reference, without noticing the effects of rotation. Conversely, for small Ro, i.e., $\tau_\Omega \ll t_f$, the effects of system

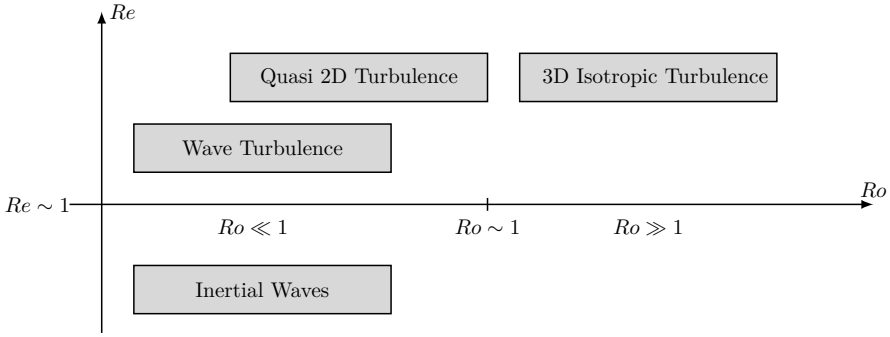

Figure 1.3: Map of the different regimes in homogeneous rotating turbulence. Inspired by Godeferd & Moisy (2015).

rotation modulate the flow. Indeed, from Eq. (1.7) we see that that the Coriolis force is proportional to $1/Ro$, thus vanishing for $Ro \gg 1$, and becoming more relevant the smaller Ro is. In many cases, Eq. (1.7) can be approximated by Eq. (1.4). But generally speaking, the importance of rotational effects depends on a balance of timescales.

1.2.2. Flow Regimes

From the previous section, we have seen that the Rossby number plays an important role, since it can change the form of the governing equations. As probably already expected, this may lead to different flow regimes which depend on the Reynolds and on the Rossby number. A qualitative description of the possible regimes is given in Godeferd & Moisy (2015), here reproduced in Fig. 1.3.

In the both low Reynolds and Rossby number limits, inertial waves are expected to dominate the flow. By increasing the Reynolds number and making the flow more energetic, while $Ro \ll 1$, we have rotating turbulence. For relatively low Re, the Coriolis force shapes the dynamics of both small and large scales, and the flow is marked by the interplay between turbulent eddies and inertial waves (wave turbulence). For higher Re, the effects of the Coriolis are felt only by the large scales, and the result is a quasi 2D turbulent flow.

Next, we first discuss what happens in the limit of very strong rotation and low Re, and subsequently we review the foundations of rotating turbulence.

Inertial Waves as Product of the Linear Dynamics

Let us consider first the case of rapidly rotating flows. One of the features that make rotating flows special is that the Coriolis force endows the fluid with wave motions. These waves, commonly referred to as inertial waves, are dispersive and can propagate energy anisotropically throughout the fluid.

For inviscid rapidly rotating fluids, such that the magnitude of the Coriolis force is much larger than of the inertial forces, conservation of linear momentum in a

rotating frame of reference, i.e., Eq. (1.4), assumes the following form:

$$\frac{\partial \mathbf{u}}{\partial t} + 2(\boldsymbol{\Omega} \times \mathbf{u}) = -\nabla q. \tag{1.9}$$

It can be shown that the equation above supports plane wave solutions of the type

$$\mathbf{u} = \Re\{\hat{\mathbf{u}} \exp\left[I(\boldsymbol{\kappa} \cdot \mathbf{x} - \sigma t)\right]\}, \tag{1.10}$$

where $\hat{\mathbf{u}}$ is the wave amplitude vector, I is the unit imaginary number, $\boldsymbol{\kappa}$ is the wavenumber vector, σ is the wave frequency and $\Re$ denotes the real part (see Appendix B for the details). The frequencies of the inertial waves depend on the wavenumber $\boldsymbol{\kappa}$, and are given as

$$\sigma = \pm \frac{2(\boldsymbol{\Omega} \cdot \boldsymbol{\kappa})}{\kappa}, \tag{1.11}$$

from which follows that the phase and the group velocity are

$$\mathbf{c}_p = \pm 2 \frac{(\boldsymbol{\kappa} \cdot \boldsymbol{\Omega})}{\kappa^3} \boldsymbol{\kappa} \quad \text{and} \quad \mathbf{c}_g = \pm 2 \frac{\boldsymbol{\kappa} \times (\boldsymbol{\Omega} \times \boldsymbol{\kappa})}{\kappa^3}, \tag{1.12}$$

respectively. Note that throughout this work $\kappa = \|\boldsymbol{\kappa}\|$ and that both symbols are used interchangeably to denote the 2-norm of $\boldsymbol{\kappa}$. From the relations appearing in Eq. (1.12), it can be seen that $\mathbf{c}_p$ and $\mathbf{c}_g$ are orthogonal vectors, and therefore the wavepackets travel in the direction perpendicular to the phase velocity. A visual confirmation of their existence and of their anisotropic characteristic can be obtained

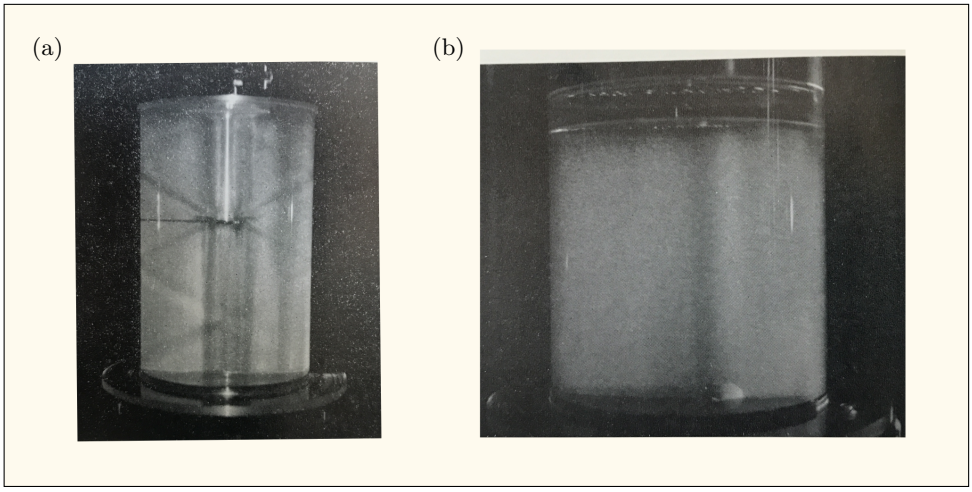

Figure 1.4: Flow field visualizations of a rapidly rotating fluid showing the inertial waves due an oscillating disk (a), and the formation of a Taylor-Proudman column on top of a slowly moving spherical object (b). Both figures have been taken from Greenspan (1968).

in a simple experimental setup: if we place a cylindrical container filled with water on a spinning turntable, and we induce a small oscillatory disturbance at the center of the container, we observe the formation of two cones that meet at the source, and bound the region along which energy is transported (Fig. 1.4a).

Another important feature of rapidly rotating fluids is that the steady-state regime does not allow for straining motions along the axis of rotation. This statement is often referred to as the Taylor-Proudman theorem, a reference to the two scientists who experimentally demonstrated it (Taylor, 1921) and derived it mathematically (Proudman, 1916). A simpler mathematical derivation can be obtained from the vorticity equation. An evolution equation for the vorticity field can be obtained by taking the curl of Eq. (1.9) to yield

$$\frac{\partial \boldsymbol{\omega}}{\partial t} - 2(\boldsymbol{\Omega} \cdot \nabla \mathbf{u}) = 0, \tag{1.13}$$

where $\boldsymbol{\omega} = (\epsilon_{ijk} \partial u_k / \partial x_j)\, \tilde{\mathbf{e}}_i$ is the vorticity vector, ϵ_{ijk} is the permutation symbol and $\tilde{\mathbf{e}}_i$ is the Cartesian versor. By neglecting temporal variations in Eq. (1.13), we find that the vorticity field is orthogonal to the gradient of the velocity field. If we consider (for simplicity), that the rotation vector is oriented upwards, i.e., $\boldsymbol{\Omega} = \Omega\, \tilde{\mathbf{e}}_3$, this implies that

$$\frac{\partial u_i}{\partial x_3} = 0, \tag{1.14}$$

and therefore in the limit of rapid rotation, velocity gradients in the direction of the rotation axis are not allowed. This feature can be experimentally demonstrated by slowly towing a solid object across a rapidly rotating fluid, and with the aid of dye (Fig. 1.4b). In such a set-up, a column of fluid, known as the Taylor-Proudman column, forms on the top of the object such that the motion of all other fluid particles are constrained to the plane horizontal to the axis of rotation. The column moves as if it were attached to the object, and no other fluid particle enters it, in agreement with Eq. (1.14).

The first evidences of this phenomenon in rotating flows dates back to the experiments by Lord Kelvin. In that experiment, two corks were placed in a rotating tank, one on top of the other. By displacing the upper cork with the aid of a thin wire, it was observed that the cork below also moved. As the fluid could not be strained, it behaved like a rigid body and propagated the force from one cork to the other. Note that although the Taylor-Proudman theorem (Eq. (1.14)) states that the flow is two-dimensional, it does not impose any restriction regarding the magnitude of the velocity component along the axis of rotation. Hence it does not prohibit the existence of 2D-3C (two-dimensional three-component) flows.

Rotating Turbulence

The first observations on rotating turbulence were made by Ibbetson & Tritton (1975), Hopfinger *et al.* (1982), S. C. Dickinson (1982). Although these experiments brought insight to the topic and motivated further studies, they were far from the idealized flow, i.e., statistically homogeneous turbulence (Davidson *et al.*, 2013). A common finding in these early experiments, nevertheless, was that rotation induces

the formation of long-lived columnar eddies aligned with the rotation axis. Experiments of statistically homogeneous rotating turbulence were later reported by Jacquin *et al.* (1990), whose configuration used an axial wind-tunnel in the presence of a rotating fine mesh. Jacquin *et al.* (1990) carried out measurements and reported that for small Ro, the integral lengthscale in the direction of the rotation axis grew linearly with time, thus verifying the observations of early experiments related to the formation of elongated structures. Moreover, they noted that rotation reduced the rate of energy decay, suggesting that rotation inhibits energy dissipation. These findings have also been confirmed more recently in the experiments of Staplehurst *et al.* (2008). Following Davidson *et al.* (2013) and Sagaut & Cambon (2018), we can summarize the main features of rotating turbulence as:

- for $Ro \approx 1$ and smaller, columnar eddies form;
- the integral lengthscale parallel to the rotation axis grows linearly during the formation of columnar eddies;
- rotation reduces the kinetic energy dissipation rate
- distinct anisotropy characterized by a transition from a three-dimensional to a two-dimensional state.

Among the features above, the formation of columnar eddies is the most interesting trait of rotating turbulence. The growth of the flow structures preferentially along the axis of rotation renders the flow anisotropy and is a visual confirmation of the tendency towards a two-dimensional three-component (2D-3C) state. The reason for transition towards a 2D flow is often wrongly attributed to the Taylor-Proudman theorem, which can not predict transition from a 3D state to a 2D state. Due to its linear and inviscid equations, it yields conservation of energy and enstrophy and therefore does not allow inter-scale energy transfer (Cambon *et al.*, 1997). However, other explanations of the formation of these columnar eddies have appeared in literature.

Works like Davidson *et al.* (2006) and Staplehurst *et al.* (2008) claim that the linear dynamics can contribute to the formation of columnar structures. These authors, for instance, performed experiments where an initially quiescent fluid is spun. In this scenario, they observed that the size of the turbulent regions grew in time in the direction of rotation. The growth rate was linear and they associated it with the group velocity of the inertial waves. In contrast, several other authors affirm that the formation of columnar eddies is a nonlinear phenomena. Their hypothesis is that the Coriolis force, which does not appear in the kinetic energy evolution equation, but does plays a role in the energy exchange among the different velocity components, modulates energy transfers and favors the accumulation of energy in the slow-manifold — $\kappa_3 = 0$ plane, where κ_3 is the wavenumber along the direction of rotation. This process was early suggested to lead to two-dimensionalization of the flow in the work of Cambon & Jacquin (1989), who was able to account for the rotational effects in an initial isotropic field by employing a modified Eddy Damped Quasi-normal Markovian Theory (EDQNM2). The accumulation of energy in the

plane normal to the axis of rotation has since then been confirmed by different Direct Numerical Simulations, see e.g., Mininni *et al.* (2009); Morinishi *et al.* (2001) or Alexakis & Biferale (2018) for a review.

Direct Numerical Simulations have therefore proven to be an important pillar for the study of rotating turbulence. These kind of simulations provide easy and accurate access throughout the domain to quantities which are often called upon to explain the dynamics of rotating turbulence, e.g., directional two-point correlations, transfer functions (triad interactions) and multidirectional energy spectra. By using directional two-point correlations for example, Yoshimatsu *et al.* (2011) reported the evolution of lengthscales. Longitudinal and transverse lengthscales, which are related when rotation is not present, were reported to differ when $Ro < 1$. The longitudinal lengthscale was observed to grow faster, which is in accordance with previous observations of long elongated structures aligned with the rotation axis. This evolution from an isotropic to an anisotropic flow is associated with a progressive loss of dependence in the direction parallel to the axis of rotation, i.e., a decrease of the variations $\partial/\partial z$ (Godeferd & Moisy, 2015), upper left regime in Fig. 1.3.

In rotating turbulence at moderate Ro numbers, however, not every scale of motion becomes anisotropic. The scales of motion affected by rotation are delimited by the Zeman wavenumber κ_Ω, "a cut-off wavenumber that delimits the region of the spectrum where rotation effects are important" (Zeman, 1994). Mininni *et al.* (2012) confirmed indeed that wavenumbers smaller than κ_Ω were affected by rotation and became highly anisotropic, whereas isotropy was recovered for wavenumbers larger than κ_Ω. This result should also be taken into account when performing forced simulations of rotating turbulence. In large scale forced simulations, energy is artificially injected into the large scales (small wavenumbers). This means that large scales are modeled by the chosen forcing scheme, whereas the smallest scales of motion are resolved. It should be noted that if the forcing acts on wavenumbers smaller than κ_Ω, the forcing method would be in competition with the true dynamics of rotating turbulence.

The observation of an inverse energy cascade in rotating turbulence, with energy being transferred from small to large scales, is also noteworthy. In turbulent flows, energy transfer is ruled by triadic interactions, which involve energy exchange between three wavenumbers. In order to analyze the energy transfers in turbulence, Waleffe (1993) introduced the instability assumption. According to this hypothesis, energy is always released by the most unstable wavenumber and leads to two different types of transfer: forward and reverse. In the forward type, energy is released from small wavenumbers and handed to larger ones, whereas in the reverse type, energy is transferred in the opposite direction. In the absence of rotation and in the inertial range, the forward type of interactions dominate, and results in a forward energy cascade characterized by the $-5/3$ Kolmogorov scaling law for the energy spectrum (Sagaut & Cambon, 2018). The results obtained by Waleffe (1993) were also believed to be applicable to rotating turbulence, but with a modified set of possible triadic interactions altered by the Coriolis force. An analysis of the possible interactions leads to the conclusion that energy is mostly transferred from

modes with wavenumbers aligned with the rotation axis to modes whose wavenumbers are closer to the transverse plane. These hypotheses were also confirmed by Smith & Waleffe (1999) and Morinishi *et al.* (2001) in more recent numerical studies. In addition, Delache *et al.* (2014) also report multidirectional energy spectra, which supports the idea that energy is drawn from the longitudinal direction and accumulates in the transverse plane.

The presence of an inverse energy cascade leads also to different spectra scaling laws. Smith & Waleffe (1999), for instance, argue that for scales of motion where rotational effects are much more important, the only dimensional parameters to be considered are the wavenumber itself and the rate of rotation. Non-dimensional analysis then yields a -3 power law for the region $\kappa < \kappa_f$, where κ_f is the wavenumber associated to the force. In an early study, Zhou (1995) suggested that in the presence of strong rotation, if the time scale of energy transfer is taken to be equal to the frequency of rotation, one obtains a -2 power law for the inertial range of the energy spectrum. Such scaling laws are indeed different from the $-5/3$ power law based on Kolmogorov hypothesis. However, in the DNS of Mininni *et al.* (2012) a $-5/3$ power law is recovered for wavenumbers larger than the Zeman wavenumber, motivating the authors to refer to the presence of a "Coriolis" and a Kolmogorov range. Baqui & Davidson (2015) have recently revisited the aforementioned laws and investigated the regime for which $Ro \approx 1$. Intriguingly a $-5/3$ power law is obtained for this regime when rotation is introduced to the system. The scaling law, however, has nothing to do with the Kolmogorov spectra, since the simulations were carried for a relatively small Reynolds number, for which an inertial range is not yet present. In passing, let us also mention that the weak inertial-wave theory of Galtier (2003) predicts anisotropic scaling, with the longitudinal energy spectra proportional to $\kappa_\parallel^{-1/2}$ and the transversal energy spectrum proportional to $\kappa_\perp^{-5/2}$.

1.3. Aim and Overview

The main goals of this thesis are: (a) find whether the inverse energy cascade in homogeneous rotating turbulence can vanish for a combination of the non-dimensional parameters, (b) obtain predictive laws for the growth rate of columnar eddies, and (c) propose a correction for the scaling of the kinetic energy dissipation rate. Additionally, having in mind that rotation often appears in combination with stratification, we explore the physics associated with the breaking events of inertia-gravity waves in the atmosphere.

As a first step towards our goals, we have designed an entirely new single-purpose DNS solver to simulate homogeneous rotating and stratified flows in unbounded domains. The details regarding the solver, i.e., governing equations, numerical approach and performance, are laid out in Chapter 2, in which we also present results that verify and validate our numerical tool. This numerical tool was tailored to perform the present numerical experiments and efficiently use high-performance computing resources. For the simulations of rotating homogeneous turbulence, we design experiments that allow us to focus solely on the interaction between the Coriolis force and an initial cloud of homogeneous isotropic eddies. Our numerical

experiments are intended to be as clean as possible, in the sense that we minimize the influence of secondary effects on the flow, as typically occurs in numerical studies due to artificial boundary conditions. The present database generated in this work is unprecedented and accounts for variation in the domain size and Rossby number, totalizing more than 50 new direct numerical simulations.

In Chapter 3, the effects of the non-dimensional parameters on the direction of the energy cascade are investigated, more specifically the influence of the domain aspect ratio and the Rossby number. This chapter shows for the first time simulations of rotating turbulence in elongated domains, in which the typical eddy size is about 340 times smaller than the computational domain. Chapter 4 builds upon the preceding chapter and analyzes one dataset for fixed domain size and 21 different rotation rates. The growth rate of columnar eddies is investigated, and a comparison with current scaling laws for the energy dissipation rate is presented. Faced with the fact that different theories fail to collapse our data for the energy dissipation rate into a single curve, we follow the ideas introduced by Kraichnan (1965) and propose a correction in terms of a power law of the Rossby number. In both of the aforementioned chapters, we also present results of the energy spectra in this large-box limit.

Additionally, we also explore a problem of atmospheric turbulence where rotation appears in combination with stratification. Chapter 5 studies the case of two inertia-gravity waves breaking in the middle-upper atmosphere and highlights the possible difficulties that basic turbulence models might encounter when employed to simulate anisotropic flows. Lastly, Chapter 6 offers a summary and conclusions of the work.

This dissertation is arranged in such a way that Chapters 3 to 5 can be read separately; each chapter begins with a brief introduction to the topic together with a review of the relevant literature.

2

Numerical Framework

2.1. A Numerical Tool for Homogeneous Flows

Although several tools are available in the scientific community to numerically simulate turbulent homogeneous flows, we decided to start from scratch and concept a computational code that could bring together up-to-date programming techniques. In the most general case, we consider as numerical domain cuboids of arbitrary size, i.e., $\mathcal{L} = [0, L_1] \times [0, L_2] \times [0, L_3]$, that are filled with an incompressible rotating and stratified fluid. The equations governing the fluid dynamics are

$$\nabla \cdot \mathbf{u} = 0 \tag{2.1}$$

$$\frac{\partial \mathbf{u}}{\partial t} + \nabla \cdot (\mathbf{u} \otimes \mathbf{u}) + 2(\mathbf{\Omega} \times \mathbf{u}) = -\nabla q + \nu \nabla^2 \mathbf{u} + b\,\mathbf{n} \tag{2.2}$$

$$\frac{\partial b}{\partial t} + \nabla \cdot (b\,\mathbf{u}) = -B_f^2 (\mathbf{u} \cdot \mathbf{n}) + \alpha \nabla^2 b, \tag{2.3}$$

where, apart from the already defined quantities, b represents the buoyancy field, α is the thermal diffusivity, B_f is the Brunt-Väisälä frequency and $\mathbf{n}$ is a unit vector that points in the direction of gravity. Equations (2.1) and (2.2) are the conservation of mass and momentum, whereas Eq. (2.3) follows from conservation of energy along with Boussinesq's approximation. As before, the effects of the centrifugal forces in Eq. (2.2) have been added to the reduced pressure q (cf. Eq. (1.5)).

Our numerical approach for numerically solving Eqs. (2.1) to (2.3) employs a pseudospectral method combined with hybrid time marching techniques. The governing equations on the discrete level are obtained by assuming that the field of interest (velocity or buoyancy) can be expanded in terms of orthogonal basis functions. Because we deal exclusively with homogeneous flows, it is enough to consider only basis functions that are trigonometric polynomials, i.e., we restrict ourselves to Fourier series representations. For instance, the velocity field is expressed as

$$u_i(\mathbf{x}, t) = \sum_{\boldsymbol{\kappa}} \hat{u}_i(\boldsymbol{\kappa}, t) e^{I \boldsymbol{\kappa} \cdot \mathbf{x}}, \tag{2.4}$$

in which the compact notation for the summation term represents a triple summation, i.e., it takes place over every wavenumber direction, and the caret $\hat{(\cdot)}$ denotes the Fourier coefficients. The wavenumbers $\boldsymbol{\kappa}$ are related to the domain size through

$$\kappa_i = (2\pi / L_i) m, \tag{2.5}$$

where m is an integer ranging from $-N_i/2$ to $N_i/2 - 1$, with N_i the number of degrees of freedom in each direction, and the nodes of the corresponding physical grid are

$$x_{i,j} = (j - 1)\Delta x_i \tag{2.6}$$

where $\Delta x_i = L_i / N_i$ is the grid spacing and $j \in \mathbb{N} : 1 \leq j \leq N_i$.

The solver is built around the basic idea of converting the partial differential equations (Eqs. (2.1) to (2.3)) to a set of dynamical equations for the Fourier coefficients that can be further advanced in time. In the sequence (Sections 2.1.1 and 2.1.2), we cover the discretization procedure and present the resulting equations in the wavenumber domain. In Section 2.1.3, we discuss time integration.

2.1.1. Equations in the Wavenumber Domain

The procedure to find approximate solutions for partial differential equations with the aid of appropriate orthogonal basis functions can be summarized as follows. First, one needs to replace every field in the original partial differential equation by its expansion, i.e., make use of Eq. (2.4) and the corresponding expansion for the buoyancy field in Eqs. (2.1) to (2.3). Second, one defines a residual (error) function, which, upon multiplication with trial functions, is forced through integration to return null. Then, with the aid of the orthogonality relation between the basis and the trial function, one obtains a dynamical system, whose unknowns are the coefficients of the expansion, and that can be later advanced in time by a suitable time integration scheme. Although at first glance the process seems tedious, it is instead relatively simple. In Appendix C, we illustrate the procedure by applying the aforementioned steps to the Burgers' equation.

Here, we present the equations in the wavenumber domain, which follow from the sequence of steps mentioned above, and constitutes the foundations of the numerical method. We do this in parts. First, we treat Eq. (2.2) due to its slightly more complex form, and second, we show the resulting equation for Eq. (2.3). For Eq. (2.1), it is enough to note that in the wavenumber domain this equation requires that Fourier coefficients are orthogonal to the wavenumber vector, i.e., $\boldsymbol{\kappa} \cdot \hat{\mathbf{u}}(\boldsymbol{\kappa}) = 0$.

Conservation of Linear Momentum

Following the instructions described in Appendix C, it is readily shown that Eq. (2.2) yields

$$\frac{\partial \hat{u}_i}{\partial t} + \hat{c}_i + 2\epsilon_{ijk}\Omega_j \hat{u}_k = -I\kappa_i \hat{q} - \nu \left\|\boldsymbol{\kappa}\right\|^2 \hat{u}_i + bn_i, \tag{2.7}$$

where the convective terms have been grouped as $\hat{c}_i = I\kappa_j \mathcal{F}\{u_i u_j\}$, with $\mathcal{F}\{\cdot\}$ denoting the Fourier coefficients of the terms within the brackets. An advantage of this method with respect to approaches that deal with the equations of motion in physical space is that it does not need require to solve for the pressure field, as, for example, typically required by the fractional-step method in finite-difference or finite-volume methods (Ferziger & Perić, 2002). In our case, the pressure field can be computed with the aid of the incompressibility condition, and its solution can be back propagated to eliminate the pressure from the set of equations. By enforcing $\kappa_i \hat{u}_i = 0$ upon Eq. (2.7), we obtain

$$\hat{q} = \frac{I\kappa_m \hat{c}_m}{\left\|\boldsymbol{\kappa}\right\|^2} + 2I\frac{\kappa_m}{\left\|\boldsymbol{\kappa}\right\|^2}\epsilon_{mjk}\Omega_j \hat{u}_k - \frac{I\kappa_m bn_m}{\left\|\boldsymbol{\kappa}\right\|^2}, \tag{2.8}$$

which contains on its right-hand-side the divergence of the convective terms, along with contributions due to the Coriolis and to the buoyancy force. We can further simplify Eq. (2.8) by grouping the contributions due to the convective and the buoyancy terms into $\hat{h}_m = \hat{c}_m - bn_m$, such that

$$\hat{q} = \frac{I\kappa_m \hat{h}_m}{\left\|\boldsymbol{\kappa}\right\|^2} + 2I\frac{\kappa_m}{\left\|\boldsymbol{\kappa}\right\|^2}\epsilon_{mjk}\Omega_j \hat{u}_k. \tag{2.9}$$

Now, back substitution of Eq. (2.9) into Eq. (2.7) leads to

$$\frac{\partial \hat{u}_i}{\partial t} + \nu \left\|\boldsymbol{\kappa}\right\|^2 \hat{u}_i + \left[2\epsilon_{ijk}\Omega_j \hat{u}_k - 2\frac{\kappa_i \kappa_m}{\left\|\boldsymbol{\kappa}\right\|^2}\epsilon_{mjk}\Omega_j \hat{u}_k\right] = -\left(\delta_{im} - \frac{\kappa_i \kappa_m}{\left\|\boldsymbol{\kappa}\right\|^2}\right)\hat{h}_m. \quad (2.10)$$

We see that, as a result of the elimination of the pressure field, the influence of the Coriolis force (terms within the square brackets in the left-hand-side) is twofold. By invoking the incompressibility condition (see Appendix E), these two terms can be concatenated and Eq. (2.7) can be finally written as

$$\frac{\partial \hat{u}_i}{\partial t} + \nu \left\|\boldsymbol{\kappa}\right\|^2 \hat{u}_i + \frac{2\Omega_p \kappa_p}{\left\|\boldsymbol{\kappa}\right\|^2}\epsilon_{iql}\kappa_q \hat{u}_l = -\left(\delta_{im} - \frac{\kappa_i \kappa_m}{\left\|\boldsymbol{\kappa}\right\|^2}\right)\hat{h}_m. \quad (2.11)$$

Alternatively, Eq. (2.11) can be written in a more compact notation, viz.,

$$\frac{\partial \hat{\mathbf{u}}}{\partial t} + \mathcal{D}\hat{\mathbf{u}} + \mathcal{R}\hat{\mathbf{u}} = -\mathcal{P}\hat{\mathbf{h}}, \quad (2.12)$$

from which we will benefit in Section 2.1.3 when we deal with time marching schemes. In Eq. (2.12), the second-order tensors $\mathcal{D}$ and $\mathcal{R}$ are

$$\mathcal{D} = \begin{pmatrix} \nu\left\|\boldsymbol{\kappa}\right\|^2 & 0 & 0 \\ 0 & \nu\left\|\boldsymbol{\kappa}\right\|^2 & 0 \\ 0 & 0 & \nu\left\|\boldsymbol{\kappa}\right\|^2 \end{pmatrix} \quad \text{and} \quad \mathcal{R} = \frac{2\Omega_p \kappa_p}{\left\|\boldsymbol{\kappa}\right\|^2}\begin{pmatrix} 0 & -\kappa_3 & \kappa_2 \\ \kappa_3 & 0 & -\kappa_1 \\ -\kappa_2 & \kappa_1 & 0 \end{pmatrix},$$

and

$$\mathcal{P}_{im} = \left(\delta_{im} - \frac{\kappa_i \kappa_m}{\left\|\boldsymbol{\kappa}\right\|^2}\right) \quad (2.13)$$

is the projection tensor.

Conservation of Energy

Writing the conservation of energy in the wavenumber domain is essentially simpler, since Eq. (2.3) is neither influenced by the pressure field nor by the Coriolis force. Following the same logical steps (cf. Appendix C), it can be shown that Eq. (2.3) becomes

$$\frac{\partial \hat{b}}{\partial t} + I\kappa_j \mathcal{F}\left\{b u_j\right\} = -B_f^2(\hat{u}_i n_i) - \alpha\left\|\boldsymbol{\kappa}\right\|^2 \hat{b}, \quad (2.14)$$

or in compact notation

$$\frac{\partial \hat{b}}{\partial t} + \gamma\,\hat{b} = \hat{c}_{buo} \quad (2.15)$$

where $\gamma = \alpha\left\|\boldsymbol{\kappa}\right\|^2$ and $\hat{c}_{buo} = -B_f^2(\hat{u}_i n_i) - I\kappa_j \mathcal{F}\left\{b u_j\right\}$.

2.1.2. The Pseudospectral Approach

If it were not for one difficulty, it would be straightforward to advance Eqs. (2.12) and (2.15) in time. This difficulty arises from the nonlinear terms that appear on the right-hand-side of both Eqs. (2.12) and (2.15) and require information about all other wavenumbers. More precisely, we refer here to the terms

$$\mathcal{F}\{u_i u_j\} \quad \text{and} \quad \mathcal{F}\{b u_j\}, \tag{2.16}$$

which compose $\hat{\mathbf{h}}$ and $\hat{c}_{buo}$. In the following, we elaborate on what makes it hard to compute these terms, and show how their computation is in practice handled. We confine our attention to the calculation of $\mathcal{F}\{u_i u_j\}$, since this is sufficient to understand the gist of the problem.

In theory, we could calculate $\mathcal{F}\{u_i u_j\}$ through a convolution sum. By definition, the Fourier transform of a product is given by

$$\mathcal{F}\{u_i u_j\} = \sum_{\boldsymbol{\kappa'}+\boldsymbol{\kappa''}=\boldsymbol{\kappa}} \hat{u}_i(\boldsymbol{\kappa'})\hat{u}_j(\boldsymbol{\kappa''}) \tag{2.17}$$

(Tolstov & Silverman, 1976). Nevertheless, the number of operations required to evaluate the summation in Eq. (2.17) scales with N_p^2, where N_p is the total number of degrees of freedom. In fluid mechanics, we usually encounter problems with large number of unknowns. For certain cases, the number of degrees of freedom is proportional to $Re^{9/4}$ (Landau & Lifshitz, 1959), meaning that a small increase in Re requires a steep rise in N_p to cope with the new spatial scales of motions. As a result, evaluating $\mathcal{F}\{u_i u_j\}$ through Eq. (2.17) turns out to be computationally expensive and often prohibitive.

An alternative to remedy this cost is to employ the pseudospectral method introduced originally by Orszag (1969). The central idea is to first build the nonlinear product in physical space, e.g., $s_{ij} = u_i u_j$, and then transform the result into the wavenumber domain, using Discrete Fourier Transforms (DFT) to obtain $\mathcal{F}\{s_{ij}\}$. This technique can drastically reduce the number of operations from N_p^2 to $N_p \log_2(N_p)$. But, it comes at a price. It introduces aliasing errors and the obtained result is not fully equivalent to Eq. (2.17). Mathematically speaking, the pseudospectral leads to

$$\mathcal{F}\{s_{ij}\} = \sum_{\boldsymbol{\kappa'}+\boldsymbol{\kappa''}=\boldsymbol{\kappa}} \hat{u}_i(\boldsymbol{\kappa'})\hat{u}_j(\boldsymbol{\kappa''}) + \underbrace{\sum_{\boldsymbol{\kappa'}+\boldsymbol{\kappa''}=\boldsymbol{\kappa}\pm\mathbf{N}} \hat{u}_i(\boldsymbol{\kappa'})\hat{u}_j(\boldsymbol{\kappa''})}_{\text{aliasing errors}}, \tag{2.18}$$

from which we see that the aliasing errors contaminate the Fourier coefficients associated with high wavenumbers.

Fortunately, there are several techniques for removing the aliasing errors, viz., de-aliasing techniques, which overall still yield a lower computational cost than computing the convolution sum (see e.g. Boyd (2001) and Canuto *et al.* (2006*a*,*b*) for an extensive discussion). A popular choice, due to the ease of implementation is the 3/2-rule, also known as the 2/3-rule. In this technique, the velocity field (or the

variable of interest) is first sampled in physical space on a uniform grid with $3N_i/2$ nodes per direction. Multiplication is then performed in the physical grid and the Fourier coefficients are obtained through an oversized DFT. Upon transformation to the wavenumber domain, the Fourier coefficients are pruned, i.e., the coefficients associated to the additional degrees of freedom are discarded. This approach shifts the aliasing errors to wavenumbers higher than those associated with $m = N_i/2$, and guarantees that the coefficients of interest are unaffected.

When a dealiasing technique is combined with the pseudospectral approach, the final set of equations are equivalent to those obtained with the Fourier-Galerkin method. There are, however, ongoing debates in the scientific community on whether dealiasing is required. Many authors consider it unnecessary as long as enough resolution is provided. For large N_p, both truncation and aliasing errors decays at the same rate, but for a fixed N_p, the pseudospectral error will be larger than the Fourier-Galerkin error (Canuto *et al.*, 2006*b*). This point will be further discussed in Section 2.1.5 where we compare results of aliased and dealiased computations for different formulations of the Navier-Stokes equations.

2.1.3. Time Integration

So far we have shown how to transform the original partial differential equations into dynamical equations for the Fourier coefficients. Here, we target an essential part of the code, namely the time integration schemes, necessary for obtaining the long-time behavior of the system of equations. To advance the equations in time, we use a hybrid approach, in which some of the terms are treated with the integrating factor technique (Morinishi *et al.*, 2001; Rogallo, 1977) and the remaining are treated with either a third or fourth-order low-storage Runge-Kutta scheme (Canuto *et al.*, 2006*a*,*b*).

Technically, time integration could be solely accomplished by employing an explicit scheme like the Runge-Kutta scheme. For that, we would need to rearrange the equations of motion, e.g., Eq. (2.12), such that it is written as

$$\frac{\partial \hat{\mathbf{u}}}{\partial t} = \mathbf{l}(\hat{\mathbf{u}}, t). \tag{2.19}$$

By comparing Eq. (2.12) with Eq. (2.19), we see that this simply requires $\mathbf{l}(\hat{\mathbf{u}}, t) = -\mathcal{D}\hat{\mathbf{u}} - \mathcal{R}\hat{\mathbf{u}} - \mathcal{P}\hat{\mathbf{h}}$. Although this approach suffices, it places severe constrains in the size of the marching step (Δt). In numerical time integration, the timestep size follows from a compromise between the maximum eigenvalue of the operator on the right-hand-side of Eq. (2.19) and the size of the stability region, which depends on the time integration scheme. In another words, to integrate the equations in a stable manner, the maximum eigenvalue scaled with the timestep size must lie within the stability limits of the time integration scheme.

The different terms that compose $\mathbf{l}(\hat{\mathbf{u}}, t)$ can stem from different physical processes, and impose limits on Δt in different ways. For example, it can be show from the structure of the operator $\mathcal{D}$ that the maximum eigenvalue imposed by the viscous terms lies always on the real axis and is proportional to $\nu\kappa_{max}^2$, where κ_{max} is the largest positive wavenumber. Similarly, it can also be shown that the maximum

eigenvalue of $\mathcal{R}$ varies with 2Ω, where Ω is the absolute angular velocity of the rotating frame, and lies on the imaginary axis. In the case of $\mathbf{l}(\mathbf{u},t) = -\mathcal{D}\hat{\mathbf{u}} - \mathcal{R}\hat{\mathbf{u}} - \mathcal{P}\hat{\mathbf{h}}$, the maximum eigenvalue would have a component on the real axis due to the viscous terms and a component on the imaginary axis defined by the rotation rate. This would imply that we would have to choose a timestep of the order of either $1/(\nu\kappa_{max}^2)$ or $1/(2\Omega)$, whichever is stricter. We can then imagine that, even in the case of small Re (large ν), for high rotation rates, the above constraint requires increasingly small Δt, which would render simulations of multiples of large-eddy turnover times unfeasible.

In passing, we should also mention that the convective terms $\hat{\mathbf{h}}$ impose constraints in the timestep size. Stability analysis of a simplified linear transport equation with constant velocity shows that the eigenvalues lie on the imaginary axis and their magnitude is proportional to the transport velocity. However, when rotation is considered, stability limits on the imaginary axis are more likely to stem from the effects of rotation.

Exact Time Integration

In non-rotating unstratified flows, a common approach is to combine the Runge-Kutta scheme with another method for the integration of the viscous terms, for example, with the Crank-Nicolson method. This is definitely one way to go, since methods like the Crank-Nicolson are implicit and unconditionally stable. In the wavenumber domain, implementation of the Crank-Nicholson method is straightforward and has no noticeable extra cost. because the viscous terms are linear and local. Yet, another approach turns out to be more attractive, namely the integrating factor technique, which was introduced by Rogallo (1977) to integrate the viscous terms. This technique provides exact integration and it is not limited by the timestep size. Further, it can also be used to integrate any other linear term, such as the Coriolis force (see e.g. Morinishi *et al.* (2001)).

In Appendix D, we include a surrogate problem to illustrate the innerworkings of the integrating factor technique. In its essence, it allows us to find transformations that can bring Eq. (2.12) into the following form,

$$\frac{\partial \hat{\mathbf{v}}}{\partial t} = \mathbf{l}_v(\hat{\mathbf{v}}, t) \tag{2.20}$$

where $\hat{\mathbf{v}}$ is a new variable, which contains the former velocity field $\hat{\mathbf{u}}$ and the effects due to viscosity and/or rotation. If we know how to compute exponentials of second-order tensors, it turns out that the required steps are relatively simple. For instance, in the absence of rotation and stratification, Eq. (2.12) is

$$\frac{\partial \hat{\mathbf{u}}}{\partial t} + \mathcal{D}\hat{\mathbf{u}} = -\mathcal{P}\hat{\mathbf{c}}, \tag{2.21}$$

and multiplying both sides by $\mathcal{M}_\nu = \exp[\mathcal{D}t]$, leads to

$$\frac{\partial(\mathcal{M}_\nu \hat{\mathbf{u}})}{\partial t} = -\mathcal{M}_\nu \mathcal{P}\hat{\mathbf{c}}, \tag{2.22}$$

from which we can define $\hat{\mathbf{v}} = \mathcal{M}_\nu \hat{\mathbf{u}}$ and $\mathbf{l}_v(\hat{\mathbf{v}}, t) = -\mathcal{M}_\nu \mathcal{P}\hat{\mathbf{c}}$ to obtain an expression in the fashion of Eq. (2.20). In this case, $\mathcal{M}_\nu$ is a diagonal tensor and defined by

$$\mathcal{M}_\nu = \exp[\mathcal{D}t] = \exp\left(\nu \left\|\boldsymbol{\kappa}\right\|^2 t\right)\mathcal{I}, \tag{2.23}$$

where $\mathcal{I}$ is the identity tensor. Note that because $\mathcal{D}$ is diagonal, calculating $\exp[\mathcal{D}t]$ is straightforward.

If we now consider the Coriolis force and include the term $\mathcal{R}\hat{\mathbf{u}}$ into Eq. (2.21), we can still apply the same procedure. But this time, we multiply Eq. (2.21) with both $\mathcal{M}_\nu$ and $\mathcal{M}_\Omega = \exp[\mathcal{R}t]$ such that we obtain

$$\frac{\partial(\mathcal{M}_\nu \mathcal{M}_\Omega \hat{\mathbf{u}})}{\partial t} = -(\mathcal{M}_\Omega \mathcal{M}_\nu)\mathcal{P}\hat{\mathbf{c}}. \tag{2.24}$$

Again, we can define $\hat{\mathbf{v}} = (\mathcal{M}_\nu \mathcal{M}_\Omega)\hat{\mathbf{u}}$ and $\mathbf{l}_v(\hat{\mathbf{v}}, t) = -(\mathcal{M}_\nu \mathcal{M}_\Omega)\mathcal{P}\hat{\mathbf{c}}$ to obtain an equation like Eq. (2.20).

Nevertheless, $\mathcal{R}$ is not diagonal and to compute $\mathcal{M}_\Omega = \exp[\mathcal{R}t]$ we need the eigendecomposition of $\mathcal{M}_\Omega$, i.e., we need to write $\mathcal{R} = \mathcal{Q}\mathcal{R}_\Lambda\mathcal{Q}^{-1}$, where $\mathcal{Q}$ is obtained from the eigenvectors of $\mathcal{R}$ and $\mathcal{R}_\Lambda$ is a diagonal tensor whose elements are the eigenvalues of $\mathcal{R}$ (see Appendix B.1 for the definitions). This way, $\mathcal{M}_\Omega = \exp[\mathcal{R}t] = \mathcal{Q}\exp[\mathcal{R}_\Lambda t]\mathcal{Q}^{-1}$, and Eq. (2.24) becomes

$$\frac{\partial}{\partial t}\left(\exp[(\mathcal{D}+\mathcal{R}_\Lambda)t]\mathcal{Q}^{-1}\hat{\mathbf{u}}\right) = -\left(\exp[(\mathcal{D}+\mathcal{R}_\Lambda)t]\mathcal{Q}^{-1}\right)\mathcal{P}\hat{\mathbf{c}}, \tag{2.25}$$

from which we can define

$$\hat{\mathbf{v}} = \left(\exp[(\mathcal{D}+\mathcal{R}_\Lambda)t]\mathcal{Q}^{-1}\right)\hat{\mathbf{u}} \tag{2.26}$$

and

$$\mathbf{l}_v(\hat{\mathbf{v}}, t) = -\left(\exp[(\mathcal{D}+\mathcal{R}_\Lambda)t]\mathcal{Q}^{-1}\right)\mathcal{P}\hat{\mathbf{c}}. \tag{2.27}$$

Including the effects of stratification only requires to replace $\hat{\mathbf{c}}$ by $\hat{\mathbf{h}}$ in Eq. (2.27).

The same procedure can also be applied to the conservation of energy. Equation (2.15) is essentially simpler as it does not contain any explicit influence of the Coriolis force, and the resulting equation is

$$\frac{\partial}{\partial t}\left(\exp[\gamma t]\hat{b}\right) = \exp[\gamma t]\,\hat{c}_{buo}. \tag{2.28}$$

2.1.4. Forcing Methods

It is often convenient to study homogeneous turbulent flows that are sustained in time. In contrast to studies that initialize the velocity field according to an initial energy spectrum (typically of the Batchelor of Saffman type), and let the flow field decay in time, forced simulation allow the gathering of flow statistics in time, without the need to repeat the numerical experiment to build ensemble averages. Current literature contains a multitude of ways to design a force term that, when added to the right-hand-side of the momentum equations, produces statistically steady-state solutions. In our tool, we choose to implement two different forcing schemes, namely

the schemes proposed by Eswaran & Pope (1988) and Alvelius (1999). Whereas the former allows for forcing schemes with a characteristic timescale, the latter is more versatile and allows for fine tuning of the energy input rate.

The rate at which energy is injected on the system depends on both force-velocity and force-force correlations. This can be illustrated by considering a one-dimensional dynamical system as shown in Alvelius (1999). Instead of the full Navier-Stokes equations, let the evolution equation be one-dimensional and given by

$$\frac{\partial u_1}{\partial t} = f_1(x_1, t) \tag{2.29}$$

where f_1 is a random external force that drives the system. Now, assume that we employ a time marching scheme to numerically solve Eq. (2.29), e.g., an explicit Euler scheme. The (in time) discretized equation is

$$u_1^{j+1} = u_1^j + \Delta t f_1^j, \tag{2.30}$$

where the superscript j denotes the time level. The local kinetic energy at any time level j is defined as $(u_1^j u_1^j)/2$, such that, in a discrete sense, the box-averaged kinetic energy K varies as

$$\frac{K^{j+1} - K^j}{\Delta t} = \langle u_1^j f_1^j \rangle_{\mathcal{L}} + \frac{1}{2} \langle f_1^j f_1^j \rangle_{\mathcal{L}} \Delta t, \tag{2.31}$$

in which $\langle \cdot \rangle_{\mathcal{L}}$ denotes box-averages. From this simple example, we observe that the rate at which energy is injected into the system depends on both spatial correlations: the force-velocity correlation, and the force-force correlation, the latter being also proportional to the timestep size.

In simulations it is desirable to known *a priori* the final energy input rate due to the force, since this allows for the design of the numerical experiments and for control of the physical parameters. In a steady-state, the box-averaged energy input rate $\langle \varepsilon_I \rangle_{\mathcal{L}}$ matches the viscous dissipation $\langle \varepsilon_\nu \rangle_{\mathcal{L}}$. Knowledge of $\langle \varepsilon_I \rangle_{\mathcal{L}}$ in beforehand allows for predictions of quantities such as the Kolmogorov microscale and the ultimate Re_λ of the simulation.

In the following, we detail how the methods introduced by Eswaran & Pope (1988) and Alvelius (1999) construct the external forcing $\mathbf{f}$. In both cases, the forcing is constructed in the wavenumber domain and applied to a narrow wavenumber-band. The characteristic forcing wavenumber is defined as κ_f, and the set of the forced wavenumbers is denoted as N_f.

Eswaran & Pope (1988)

The forcing scheme introduced in Eswaran & Pope (1988) is based on the Ornstein-Uhlenbeck process. In a discrete sense, the components of the forcing term are given as

$$\hat{f}_i(\boldsymbol{\kappa}, t + \Delta t) = \hat{f}_i(\boldsymbol{\kappa}, t) \left(1 - \frac{\Delta t}{T_L}\right) + \zeta_i \left(2\sigma^2 \frac{\Delta t}{T_L}\right)^{1/2} \tag{2.32}$$

where ζ_i is a complex random number drawn from a normal distribution with zero mean and unity variance, T_L is the characteristic timescale of the random process

and σ^2 is the variance. (Note that when Δt equals the characteristic timescale T_L, the force becomes white-noise and uncorrelated in time.) In practice, it is convenient to introduce another quantity, namely $\varepsilon^* = \sigma^2 T_L$, such that in the limit of $T_L \to 0$, the energy input rate remains finite (Eswaran & Pope, 1988). This force is typically a large-scale force, in the sense that it is applied to a narrow wavenumber range, such that the forced wavenumbers lie in the range $[0, \kappa_f]$, where κ_f is a characteristic forcing wavenumber. This forcing scheme has then 3 free parameters, i.e., κ_f, T_L and ε^*, which can be tuned to obtain a turbulent field with specific physical parameters.

A common difficulty encountered when using this scheme is that it is not straightforward to predict the final energy input rate and consequently the final energy dissipation rate. This problem can be circumvented, to some extent, through *ad-hoc* approximations. Using a model that takes as input a measure of the timescale of the resulting velocity field, Eswaran & Pope (1988) obtained an analytical expression to predict the final time and box-averaged energy input rate rate:

$$\langle \varepsilon_I \rangle_{\mathcal{L},t} \approx \frac{4\varepsilon^* N_F}{1 + T_L^* N_F^{1/3}/\beta}, \tag{2.33}$$

where $T_L* = T_L(\varepsilon^*)^{1/3}\kappa_0^{2/3}$ is the nondimensional forcing timescale, κ_0 the lowest resolved wavenumber in the simulation, and the adjusted constant β is taken as 0.8. With prior knowledge about the energy input rate, the viscous dissipation and consequently the resulting Re_λ can be estimated. However, when the aim is to design numerical experiments with large Re_λ, our experience has shown that Eq. (2.33) leads to unsatisfactory estimates; see also the study of Chouippe & Uhlmann (2015), who experienced the same problem.

Our approach to select the free parameters that yield a desired energy dissipation rate uses as basis Eq. (2.33) but combines it with an iterative procedure to seek for the best value of T_L^*/β. In short, through a series of smaller simulations (typically with the number of degrees of freedom being set to one eighth of the actual computation), a Newton-Raphson algorithm is employed to search for a value of ε^* that delivers a desired Re_λ.

As a final step, the force $\hat{\mathbf{f}}$ needs to be made divergence free by projection in the wavenumber direction, i.e.,

$$\hat{f}_i(\boldsymbol{\kappa}) \to \hat{f}_i - \kappa_i \left(\frac{\kappa_j \hat{f}_j}{\|\boldsymbol{\kappa}\|^2} \right). \tag{2.34}$$

The latter step is required for the external force to not directly interfere with the pressure field.

Alvelius (1999)

Alvelius (1999) proposes a forcing term that is constructed around a predefined Gaussian spectrum $F(\boldsymbol{\kappa})$, which is centered around a forcing wavenumber κ_f and has standard deviation c, i.e.,

$$F(\boldsymbol{\kappa}) = C_A \exp\left[-\left(\frac{\|\boldsymbol{\kappa}\| - \kappa_f}{c} \right)^2 \right]. \tag{2.35}$$

In the equation above, C_A is a free parameter which can be tuned to control the energy input rate. The Fourier coefficients of the external force $\mathbf{f}$ are

$$\hat{f}_i(\boldsymbol{\kappa}, t) = A_{ran} e_i^1(\boldsymbol{\kappa}) + B_{ran} e_i^2(\boldsymbol{\kappa}), \tag{2.36}$$

in which $\mathbf{e}^1$ and $\mathbf{e}^2$ are unit vectors and A_{ran} and B_{ran} are complex random numbers uniformly distributed. The unit vectors are orthogonal to the wavenumber such that, per definition, the force is divergence free i.e., $\boldsymbol{\kappa} \cdot \hat{\mathbf{f}} = 0$. For each wavenumber triad, $\mathbf{e}^1$ and $\mathbf{e}^2$ are defined as

$$e_1^1 = \frac{\kappa_2}{(\kappa_1^2 + \kappa_2^2)^{1/2}}, \quad e_2^1 = -\frac{\kappa_1}{(\kappa_1^2 + \kappa_2^2)^{1/2}}, \quad e_3^1 = 0 \tag{2.37}$$

$$e_1^2 = \frac{\kappa_1 \kappa_3}{\|\boldsymbol{\kappa}\| (\kappa_1^2 + \kappa_2^2)^{1/2}}, \quad e_2^2 = -\frac{\kappa_2 \kappa_3}{\|\boldsymbol{\kappa}\| (\kappa_1^2 + \kappa_2^2)^{1/2}}, \quad e_3^2 = -\frac{(\kappa_1^2 + \kappa_2^2)^{1/2}}{\|\boldsymbol{\kappa}\|}. \tag{2.38}$$

The complex random numbers A_{ran} and B_{ran} are defined as

$$A_{ran} = \left(\frac{F(\boldsymbol{\kappa})}{2\pi \|\boldsymbol{\kappa}\|^2} \right)^{1/2} \exp(I\theta_1) g_A(\phi) \tag{2.39}$$

$$B_{ran} = \left(\frac{F(\boldsymbol{\kappa})}{2\pi \|\boldsymbol{\kappa}\|^2} \right)^{1/2} \exp(I\theta_2) g_B(\phi) \tag{2.40}$$

where the real functions g_A and g_B satisfy the relation $g_A^2 + g_B^2 = 1$, and θ_1, θ_2 and ϕ are uniformly distributed real numbers drawn for each wavenumber at each timestep; the first two are taken from the interval $[0, 2\pi]$, while the latter is taken from $[0, \pi]$. Choosing $g_A = \sin(2\phi)$ and $g_B = \cos(2\phi)$ ensures that the energy input rate is the same in all three directions and results in isotropic flow fields. For generating anisotropic flow fields with an specific energy input rate ratio between the directions, other functions can be chosen (Alvelius, 1999).

Due to its robust design, this scheme allows one to place constraints in the choice of θ_1 and θ_2 such that the force-velocity correlation is always zero, and the energy input rate stems solely from the force-force correlation. Since the force-force correlation is known and it can be computed in beforehand, it allows one to have absolute control over the energy input rate. As shown in Alvelius (1999), this is achieved by choosing θ_1 such that it satisfies

$$\tan(\theta_1) = \frac{g_A(\phi)\Re\{\xi_1\} + g_B(\phi)(\sin(\psi)\Im\{\xi_2\} + \cos(\psi)\Re\{\xi_2\})}{-g_A(\phi)\Im\{\xi_1\} + g_b(\phi)(\sin(\psi)\Re\{\xi_2\} - \cos(\psi)\Im\{\xi_2\})}, \tag{2.41}$$

where ξ_1 and ξ_2 are the projections of the coefficients of the velocity field on the directions defined by $\mathbf{e}^1$ and $\mathbf{e}^2$, i.e., $\xi_1 = \hat{u}_i e_i^1$ and $\xi_2 = \hat{u}_i e_i^2$, and $\psi = \theta_2 - \theta_1$.

Finally, the free parameter C_A follows from the desired energy input rate $\langle \varepsilon_I \rangle_{\mathcal{L}}$:

$$C_A = \frac{\langle \varepsilon_I \rangle_{\mathcal{L}}}{\Delta t} \frac{1}{\int_{N_F} \exp\left(-\frac{(\|\boldsymbol{\kappa}\| - \kappa_f)^2}{c} \right) \mathrm{d}\kappa} \tag{2.42}$$

where integration is taken over every forced wavenumber. The energy input rate is, for every instant of time, constant.

2.1.5. A Note on Different Formulations

In the previous sections, we have used the Navier-Stokes equations in their conservative form for our discussion on how to numerically solve the equations of motion. Here, we comment on alternative ways to express the conservation of linear momentum, which may result in computationally faster algorithms.

Besides the divergence form, which has already appeared in Eq. (2.2), the incompressible Navier-Stokes can be restated in three additional forms, namely in the skew-symmetric, rotation and convective form. The mathematical expressions that represent each of these forms in an inertial frame of reference and in the absence of any external/body forces are:

$$\text{Skew-Symmetric:} \quad \frac{\partial \mathbf{u}}{\partial t} + \frac{1}{2}(\mathbf{u}\cdot\nabla\mathbf{u}) + \frac{1}{2}\nabla\cdot(\mathbf{u}\otimes\mathbf{u}) = -\nabla p + \nu\nabla^2\mathbf{u}, \tag{2.43}$$

$$\text{Rotation:} \quad \frac{\partial \mathbf{u}}{\partial t} + (\boldsymbol{\omega}\times\mathbf{u}) + \frac{1}{2}\nabla\left\|\mathbf{u}\right\|^2 = -\nabla p + \nu\nabla^2\mathbf{u} \tag{2.44}$$

$$\text{Convective:} \quad \frac{\partial \mathbf{u}}{\partial t} + \mathbf{u}\cdot\nabla\mathbf{u} = -\nabla p + \nu\nabla^2\mathbf{u}, \tag{2.45}$$

$$\text{Divergence:} \quad \frac{\partial \mathbf{u}}{\partial t} + \nabla\cdot(\mathbf{u}\otimes\mathbf{u}) = -\nabla p + \nu\nabla^2\mathbf{u}. \tag{2.46}$$

where, for completeness, we have repeated the divergence form. All these 4 formulations are analytically equivalent, since they can be derived from each other with the aid of vector identities and assuming a solenoidal velocity field.

Yet, equivalence at the continuous level does not necessarily imply equivalence at the discrete level. That is, the alternative formulations may yield unequal discretized equations. When designing numerical algorithms, it is desirable to construct a numerical approximation such that the discretized equation preserves the properties of the continuous equation. Violating essential features of the original equations can result in faulty computations, which range from simulations being unreliable and not producing the correct picture of the phenomena, to unpractical simulations due to numerical overflow.

If we inspect the equations above, we note that they differ in the structure of the nonlinear operator. The fact that the nonlinear term in the Navier-Stokes can be always recast in a conservative form (as in the divergence form), ensures that in the absence of viscosity, kinetic energy is globally conserved, i.e., the kinetic energy is an invariant of the Euler equations. Therefore, if we employ the sequence of steps required to bring the continuous equations into a discrete form (Section 2.1.1), we may expect dissimilar results regarding the conservation of kinetic energy.

Canuto *et al.* (2006*a*,*b*) present a detail discussion on this matter. The bottomline is that when the pseudospectral approach is employed for evaluation of the nonlinear terms, the only formulations that ensures conservation of the kinetic en-

ergy in the discrete sense is either the skew-symmetric or the rotation form. The convective and the divergence form results in an over-accumulation of energy and ultimately overflow. Nevertheless, when a dealiasing method is included, a Fourier Galerkin approximation is obtained. In this case, all 4 formulations lead to analog semi-discrete equations, i.e., discrete in space and continuous in time, whose inviscid form conserve kinetic energy, i.e., $\mathrm{d}K/\mathrm{d}t = 0$, where $K = \frac{1}{2}\langle \mathbf{u} \cdot \mathbf{u} \rangle_{\mathcal{L}}$.

It is also worthwhile noting that the time integration scheme plays a role. The fully discrete equations only satisfy the conservation law of the semi-discrete equations if the time discretization scheme is symmetric (e.g., Crank-Nicolson). For unsymmetric time discretization schemes, as in the case of the Runge-Kutta scheme, it can be shown that the overall conservation of kinetic energy is broken. However, there is only minor violation of the conservation laws and errors typically shrink with decreasing timestep size.

So, assuming that a dealiasing technique is always necessary, what makes us choose one formulation over the other? The answer lies in the number of operations required to evaluate the nonlinear term. The computation of the nonlinear terms demands specific numbers of forward and backward discrete Fourier transforms. The number of transforms per timestep is the largest for the skew-symmetric formulation (21), and lowest for the rotation form and the divergence form (9), whereas the convective form requires 15 transforms per timestep. Thus, the rotation form is the best choice, in the sense that it requires less Fourier transforms and can be used without dealiasing.

2.1.6. A Note on Computational Implementation and Performance

In the following, we highlight the main ingredients of our DNS solver, and give an overview of its computational performance.

The computational code was written in Fortran 90 and it has been designed to efficiently exploit massively parallel supercomputer hardware. To achieve that, we have joined different programming paradigms: message passing interface (`MPI`) for inter-node communication, `OpenMP` for intra-node parallelization and parallel I/O through the `HDF5` library. The user can choose to time march the incompressible Navier-Stokes equations using any of the 4 formulations presented in Section 2.1.5, which can be further combined with the 2/3-rule to obtain alias free solutions. The time-stepping scheme uses specific strategies for each of the terms in the governing equations, cf. Section 2.1.3. In most of the cases, the integrating factor is applied to the viscous terms and the Coriolis force, whereas the convective terms and the external/body forces are integrated with a low-storage Runge-Kutta scheme (3rd or 4th order). Occasionally, and for the reasons given in Section 2.1.3, the Crank-Nicolson scheme can be applied to the viscous terms and the Runge-Kutta scheme can be also used to integrate the Coriolis force.

The performance of the code depends strongly on the efficiency of the discrete Fourier transforms, since these account for roughly 80% of the total computational time. In distributed-memory systems, Fourier transforms require global transposition of the three-dimensional arrays (all-to-all communication), and this operation

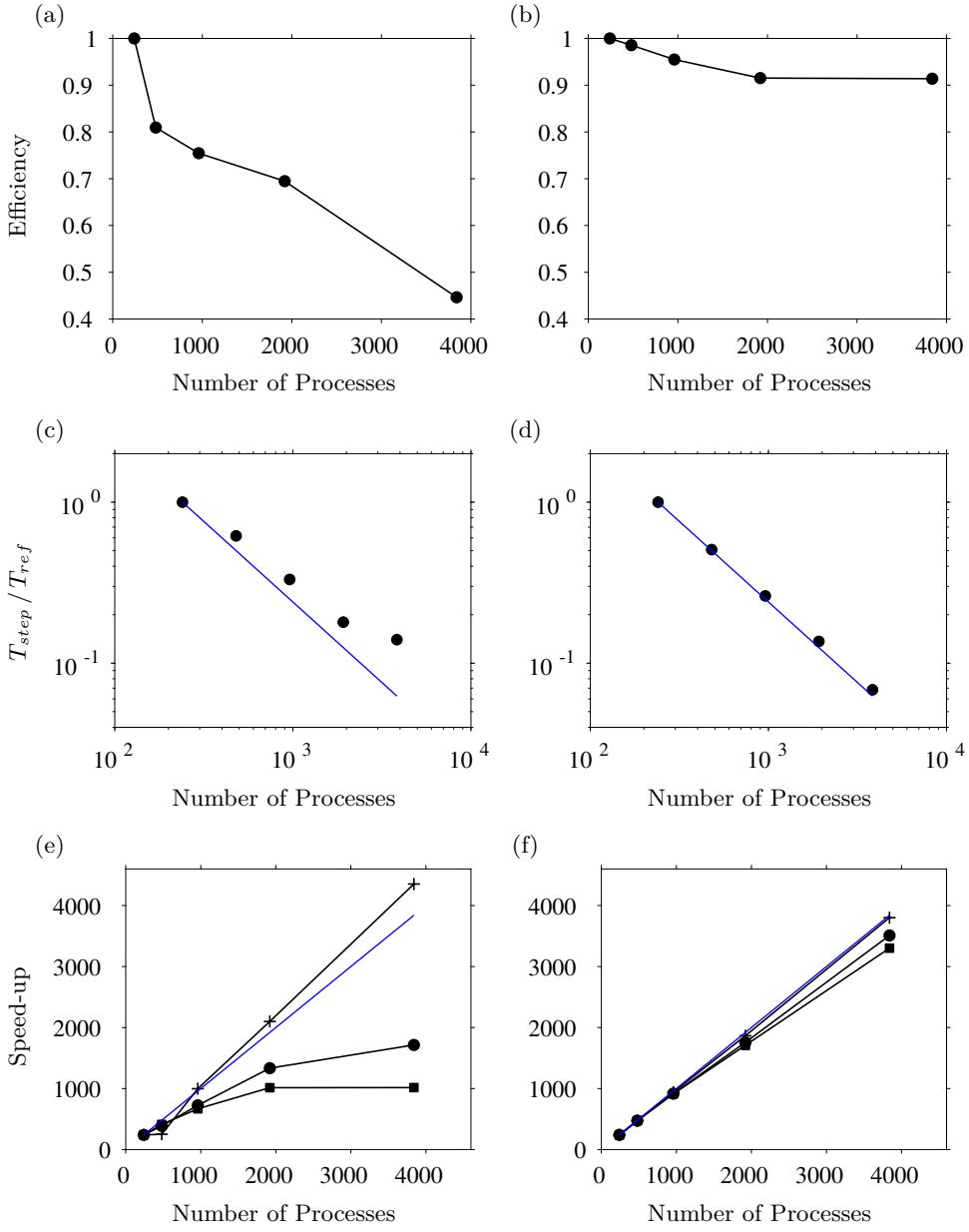

Figure 2.1: Performance of our numerical solver when applied to a problem size with $N^3 = 1024^3$ degrees of freedom (dealiased). The panels refer to two parallelization approaches: distributed with `MPI` (left) and hybrid with `MPI/OpenMP` (right). Panels (a) and (b) show the efficiency of the code, whereas (c) and (d) show the elapsed time per timestep normalized by the case with 240 processes. In (e) and (f), markers are used to represent the speed-up of the parts that constitute a single timestep: vectorized loops (—×—), discrete Fourier transforms (—■—) and the timestep itself (—●—). The thin blue line denotes the ideal behavior (—).

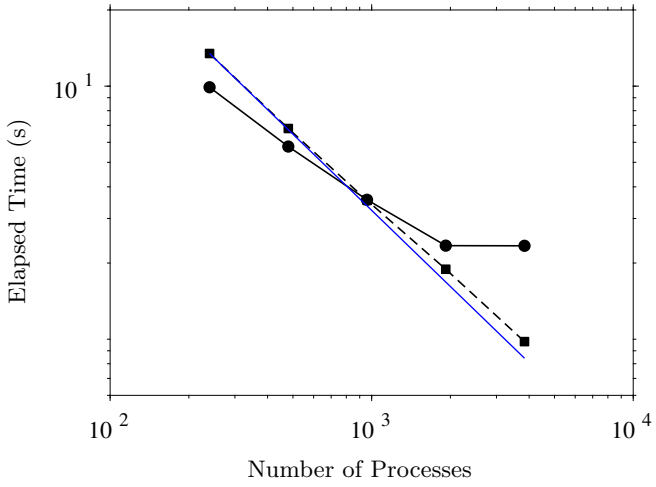

Figure 2.2: Wall-clock time required for the computation of discrete Fourier transforms per timestep for increasing number of processes. The problem size is fixed and has $N^3 = 1024^3$ degrees of freedom (dealiased) as in Fig. 2.1. Again, the markers denote two different parallelization approaches: fully distributed with `MPI` (—●—), and hybrid `MPI/OpenMP` (-■-). The thin blue line shows the ideal scaling (—).

hinges on network performance. Exclusively for this part of the code, we have opted to rely on `P3DFFT`, a well established `FFTW`-based library designed to handle three-dimensional Fourier transforms in parallel (Pekurovsky, 2012). During the development phase of the code, we have also investigated the performance of another library, namely `2DECOMP`. However, our tests have shown that `P3DFFT` outperforms `2DECOMP`, especially for large problem size and for large number of processes. In fact, Mohanan *et al.* (2019) has recently documented the performance of different libraries and confirmed the supremacy of `P3DFFT`, in agreement with our experience.

In terms of memory usage, the code is very efficient and memory requirements per core are extremely low. For each grid point, a computation with dealiasing requires approximately 630 bytes per grid point. For instance, for a problem with $N^3 = 1024^3$ (dealiased), therefore with corresponding physical domain compromising 1536^3 grid points, the required memory is not larger than 700 GB. This is significantly less than what is available in recent hardware, and only requires a couple of computing nodes, considering a typical memory size of 64 GB per node

To demonstrate the overall scalability and the speed-up of the code, we performed a scaling test on the Dutch National Supercomputer (Cartesius) with Haswell processors (Intel Xeon E5-2690V3). For the test, we fixed the problem size ($N^3 = 1024^3$, no dealiasing) and marched in time for a few timesteps with total number of processes ranging from 240 to 3840. This procedure was repeated for several realizations to obtain more reliable statistics, and it was conducted for 2 parallelization strategies: (i) purely based on `MPI`, and (ii) based on a hybrid approach which splits the number of processes among `MPI`-tasks and `OpenMP`-threads. For (ii), the number of

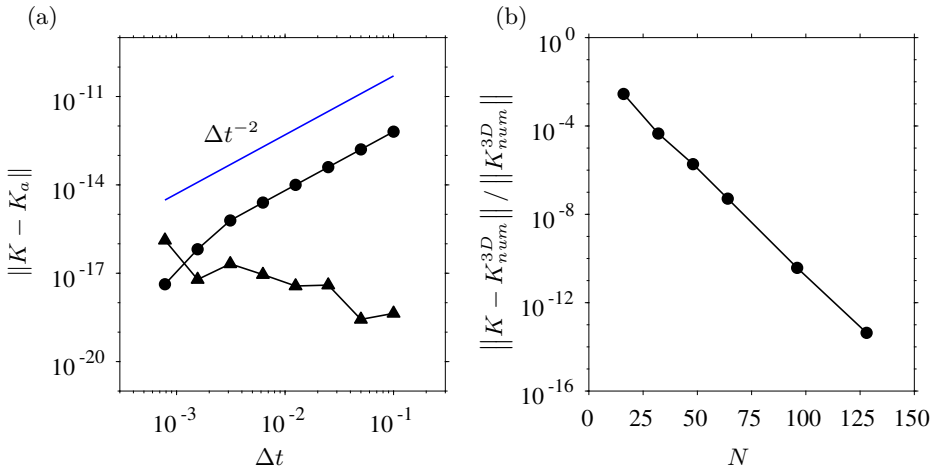

Figure 2.3: Validation of the temporal and the spatial discretization schemes. (a) Time convergence using as test case the TGV-2D. Solid line with markers indicate the numerical error due to different time integration schemes: Crank-Nicolson (●) and integrating factor (▲). A second-order power-law is added for reference (—). (b) Spectral convergence obtained for increasing number of degrees of freedom N^3 when simulating the TGV-3D.

`MPI`-tasks was taken as the number of sockets per node, in this case two.

Remarkably, when the hybrid approach is used, the code scales well up to 3840 cores, leading to a quasi-ideal performance in terms of speed-up and efficiency (Fig. 2.1). Conversely, the pure `MPI`-based approach shows an efficiency lower than 50 percent for more than 3000 processes, and the speed-up is consequently poorer. We attribute this gain in performance to the fact that all-to-all communications are cheaper in the hybrid approach, since several processes share the same memory space. Consequently, the Fourier transforms require less intra-node communication, and are less impacted by the maximum network throughput. This can actually be seen in Fig. 2.2, where we show the wall-clock time per timestep elapsed in Fourier transforms for both cases. A comparison reveals that the scaling with the hybrid approach is nearly ideal, whereas the performance of the `MPI`-based approach flats when the number of processes is increased. It is however worthwhile noting that for small number of processes, in this cases slightly smaller than 1000, the `MPI`-based approach can lead to faster execution times, in spite of the poorer scalability.

2.2. Verification and Validation

In this section, we present a set of test cases that were used to verify the correctness of our implementation. Each of them was designed to test a different part of the code. In the following, we show examples that range from simple and manufactured problems to fully developed homogeneous turbulence.

2.2.1. Taylor-Green Vortex

Perhaps the most used mean to validate and verify numerical solvers in fluid mechanics is to consider the time evolution of a Taylor-Green vortex flow. Taylor-Green vortices are velocity fields that satisfy the Navier-Stokes equations, and they can be defined in both two (TGV-2D) or three dimensions (TGV-3D). We define the TGV-2D and the TGV-3D velocity fields as

$$\text{TGV-2D:} \begin{cases} u_1 = A\cos(x_1)\sin(x_2) \\ u_2 = -A\sin(x_1)\cos(x_2) \\ u_3 = 0 \end{cases} \tag{2.47}$$

$$\text{TGV-3D:} \begin{cases} u_1 = 0 \\ u_2 = -\cos(x_1)\sin(x_2)\cos(x_3) \\ u_3 = \cos(x_1)\cos(x_2)\sin(x_3) \end{cases} \tag{2.48}$$

with $A = 1/4$ the amplitude of the velocity field. The velocity fields are built from harmonic functions, which share special symmetries and periodicity, and the streamlines form an array of counter rotating vortices. Note that other definitions may appear in the literature, but they only differ by a prefactor.

When either the TGV-2D or the TGV-3D is given as initial condition to the Navier-Stokes equations, we observe different dynamics. For the TGV-2D, due to its definition, the convective terms are null and the vortices simply decay in time. For this specific case, analytical solutions for the flow field exist, and one can show that the box-averaged kinetic evolves as

$$K_a^{2D}(t) = \frac{A^2}{4}\, e^{-4\nu t}. \tag{2.49}$$

In three dimensions, the time evolution of the TGV-3D is marked by a strong coupling between the velocity components. This interaction yields, at least initially, to an energy exchange among the different velocity components, similarly to what is observed in a real turbulent flows (energy cascade). Nevertheless, after the initial phase, which is characterized by a surge in the energy dissipation rate, the TGV-3D also decays in time due to viscous effects. For the verification and validation of the pseudospectral method and the temporal integration schemes, we performed simulations of both TGV-2D and TGV-3D in a triple periodic domain $\mathcal{L} = [0, 2\pi]^3$ and at $Re = u_{tgv}\ell_{tgv}/\nu = 100$. The terms u_{tgv} and ℓ_{tgv} denote the characteristic velocity and lengthscale, respectively, and were both set to unity.

Exclusively for verifying the time integration schemes, we performed a set of simulations of the TGV-2D with different temporal resolutions Δt. The total simulation time was $t_{obs} = 10(\ell_{tgv}/u_{tgv})$. The correctness of the method was measured by comparing the box-averaged kinetic energy at the final simulation time against its true value, i.e., $K_a^{2D}(t = t_{obs})$. Figure 2.3a shows the convergence rate of the temporal integration. We observe that the Crank-Nicolson integrating scheme leads to the expected error decay rate of the order of $\mathcal{O}(\Delta t^{-2})$, whereas the error due to the integrating factor technique is, irrespective of the timestep size, $\mathcal{O}(10^{-15})$, i.e.,

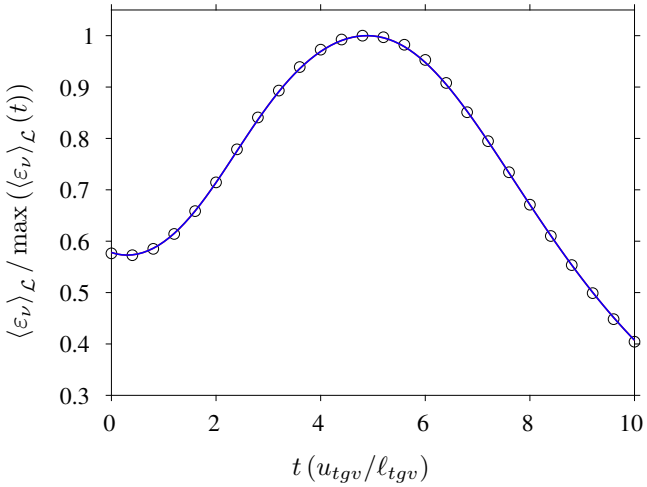

Figure 2.4: Time evolution of the box-averaged energy dissipation rate normalized by its maximum value for the TGV-3D at $Re = 100$. The simulation was performed with 128^3 (dealiased) and fixed timestep size $\Delta t = 0.01$. The different line colors represent runs with different three time marching techniques: integrating factor technique (—) and Crank-Nicolson (—). The markers (o) represent the data from Hickel *et al.* (2006).

machine precision. Both results are in solid agreement with theoretical predictions, thus verifying our time marching strategies.

For assessing spatial convergence, a separate set of runs with the TGV-3D was performed. This time, we fixed Δt and varied the spatial resolution. Unfortunately, we did not have analytical solutions nor access to any database with the same quality as the ones produced by our tool. Hence, we first generated reference data by using $N^3 = 256^3$ degrees of freedom and the skew-symmetric formulation, which is more than sufficient to resolve all scales of motion found in the TGV-3D at $Re = 100$. Figure 2.3b shows the relative error between the box-averaged kinetic energy of each of the runs and the reference box-averaged kinetic energy from our over-resolved simulation, i.e., K^{3D}_{num}. We observe that the error decay rate is proportional to $1/N$ (spectral convergence), showing that it decays faster than any finite power-law. Again, this is in solid agreement with the theory.

As a final test, we set $N^3 = 128^3$ and computed the TGV-3D with both time integrating schemes. The time evolution of the energy dissipation rate compared against the data found in Hickel *et al.* (2006) is shown in Fig. 2.4, from which we find a perfect agreement with the reference data. Altogether, this set of tests give us confidence regarding the numerical implementation.

2.2.2. Integrating Factor: Coriolis

Now, we verify the integrating factor technique for integration of the Coriolis force. For this test, we create a toy-problem for which an analytical solution can be eas-

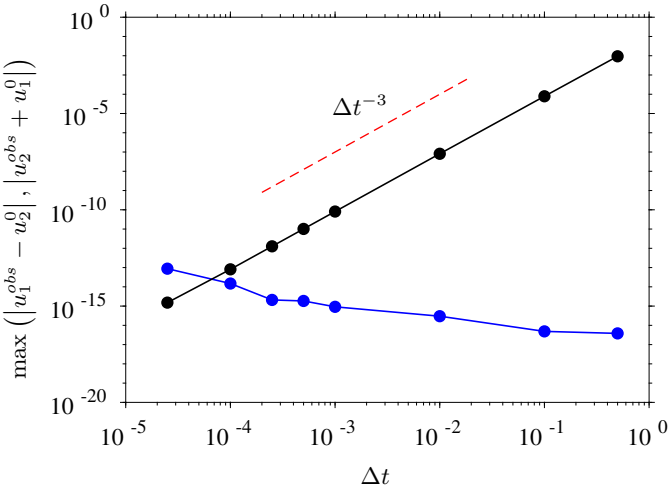

Figure 2.5: Numerical error in the solution of Eq. (2.50) for different timesteps sizes and two time integration techniques: third-order Runge-Kutta scheme (—●—) and exact integration (—●—). The dashed red line denotes a cubic power law (—).

ily obtained. Instead of solving the full Navier-Stokes equations, we consider the following system of equations:

$$\frac{\mathrm{d}\mathbf{u}}{\mathrm{d}t} = 2\boldsymbol{\Omega} \times \mathbf{u}, \tag{2.50}$$

with $\boldsymbol{\Omega} = \Omega\,\tilde{\mathbf{e}}_3$, where $\tilde{\mathbf{e}}_3$ is the unit vector along the third Cartesian direction.

It is readily shown that this problem has two eigenvalues, namely $\lambda = \pm 2I\Omega$, which are associated to the eigenvectors $(I/\sqrt{2}, 1/\sqrt{2})$ and $(-I/\sqrt{2}, 1/\sqrt{2})$, respectively. Therefore Eq. (2.50) can be diagonalized, and the solution is of the type

$$u_1^\lambda = C_1 \exp\left(-I\beta t\right) \tag{2.51}$$

$$u_2^\lambda = C_2 \exp\left(I\beta t\right), \tag{2.52}$$

where the superscript "λ" denotes the variables on the basis spanned by the eigenvectors, $\beta = 2\Omega$ and C_1 and C_2 are two integration constants which can be determined for a given initial condition. For an arbitrary initial condition, say $\mathbf{u}(t=0) = (u_1^0, u_2^0)$ the final solution in Cartesian coordinates is given by

$$u_1 = u_1^0 \cos(\beta t) + u_2^0 \sin(\beta t) \tag{2.53}$$

$$u_2 = -u_1^0 \sin(\beta t) + u_2^0 \cos(\beta t). \tag{2.54}$$

Note that Eqs. (2.53) and (2.54) are simply the equations for clockwise rotation of the vector $\mathbf{u}(t=0) = (u_1^0, u_2^0)$. At any instant of time, the velocity can be then obtained by a linear transformation of the initial velocity field.

As initial condition, we impose the two-dimensional Taylor-Green vortex, cf. Eq. (2.47). Further, we set $\Omega = \pi/2$ and march Eq. (2.50) in time until $t_{obs} = 1/2$ by using two integration schemes — the third-order Runge-Kutta and the exact integrating factor. The numerical error stems solely from time integration and we define it as the difference between the final state of the velocity field (u_1^{obs}, u_2^{obs}) and the expected solution $(u_2^0, -u_1^0)$, which is essentially the initial field rotated clockwise by $\pi/2$, cf. Eqs. (2.53) and (2.54). Figure 2.5 shows the numerical error for different timestep sizes and for both methods. As we can see, the results agree perfectly, i.e., the Runge-Kutta displays an error decay rate varying with $(\Delta t)^3$ and the exact integrating factor is machine accurate. In the latter case, the fact that the error increases for decreasing timestep size is attributed to round-off errors, which naturally accumulate; the smaller Δt, the larger are the number of steps required to reach the final simulation time.

2.2.3. Decaying Homogeneous Isotropic Turbulence

Let us now consider decaying fully developed homogeneous turbulence. For this test case, we use as reference the results from Comte-Bellot & Corrsin (1971), who reported experiments of grid turbulence. In that experiment, turbulence was generated by the contact of an incoming flow and a grid, and measurements were taken downstream of the grid, where the flow was assumed nearly isotropic. The data provided by these authors is a hallmark in the study of homogeneous isotropic turbulence, and here we attempt to reproduce the same experimental conditions numerically.

In the experiment, the flow field was first sustained for a certain time before let decay. Later, while decaying, data is probed at 3 consecutive instants of time, referred to as stages 42, 98 and 171. The first of these corresponds to the instant at which the flow is left to decay. For comparison with the available data, we generate a random velocity field and rescale every velocity component to match the initial spectrum at stage 42. Then, we give this velocity field as initial condition and evolve the equations of motion in time without external force and, obviously, in the absence of rotation and stratification.

During the first instants of time, the Fourier coefficients of the velocity field are rescaled such that the energy spectrum remains constant and the influence associated with the random initialization is diminished. After a certain time is reached, the rescaling is switched off and the flow decays. The simulations are repeated with all 4 formulations of the Navier-Stokes equations, to observe the influence on the results.

Figure 2.6a compares the energy spectrum at all 3 stages with $N^3 = 384^3$ (dealiasing) and using the rotation formulation. Overall, we observe a good agreement between our simulations and the reference data. In fact, when dealiasing is used, the good agreement is independent of the chosen formulation; see Fig. 2.6b, which shows that all different formulations lead to the same result at stage 98. Conversely, in the presence of aliasing errors, the rotation and the skew-symmetric form lead to disparate behavior, especially in the high wavenumber range of the energy spectrum. Figure 2.6c compares aliased calculations with two the skew-symmetric

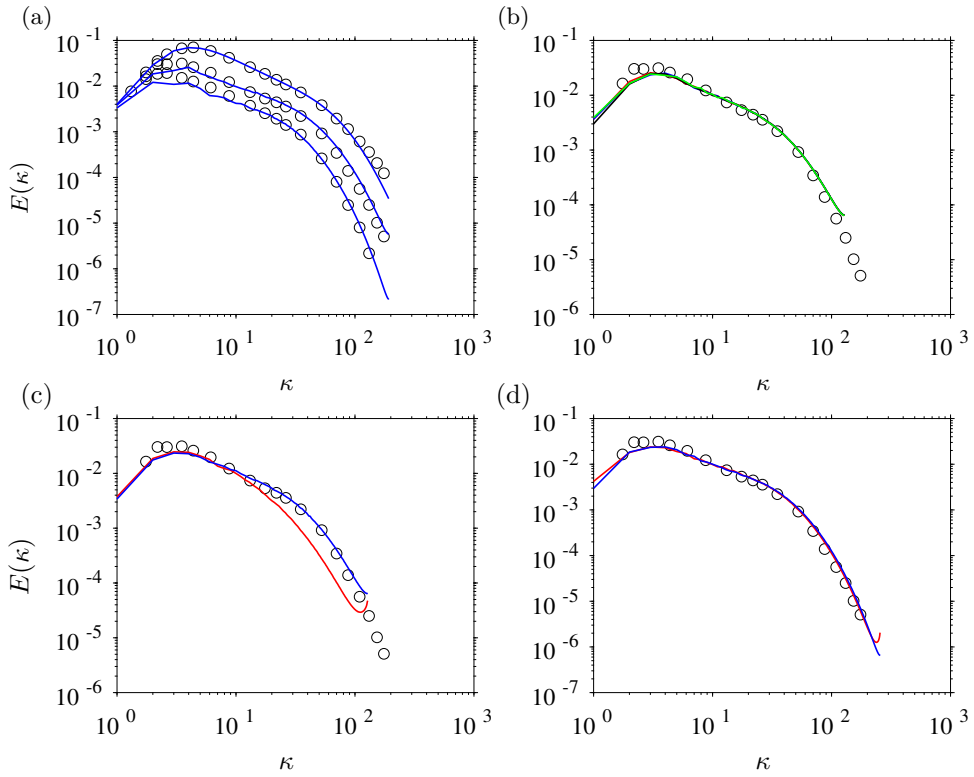

Figure 2.6: Validation of homogeneous isotropic turbulence against the experiments of CBC for stages 48, 98 and 171, together with the influence of the aliasing error on the numerical solution. (o) corresponds to the reference data from CBC. (a): (—) energy spectra at the three different stages computed with the rotation formulation and 384^3 DoF (dealiased). (b): energy spectra for stage 98 computed using 256^3 DoF (dealiased) with the four alternative formulations of the NSE, i.e., convective (—), divergence (—), rotation (—) and skew-symmetric (—). (c) energy spectra at stage 98 computed using 256^3 DoF (aliased) using the rotation form (—) and skew-symmetric (—). (d) energy spectra at stage 98 computed using 512^3 DoF (aliased) using the rotation form (—) and skew-symmetric (—).

and the rotation form and $N^3 = 256^3$. We see that the reference data is better reproduced by the skew-symmetric formulation. With the rotation formulation, aliasing errors are larger and causes significant discrepancies. If the resolution is however increased to $N^3 = 512$, while still aliased, both formulations are able to reproduce results accurately (cf. Fig. 2.6d). In the latter case, $N^3 = 512^3$ is more than sufficient, implying that truncation and aliasing errors are probably very small in both cases.

These tests were performed in the initial development phase of the code, and all simulations used the Crank-Nicolson method for integrating the viscous terms and the 3rd order Runge-Kutta for integrating the convective terms.

2.2.4. Forced Homogeneous Isotropic Turbulence

In contrast to the previous section, we now consider cases for which the system is initially at rest, and homogeneous isotropic turbulence is generated by injecting energy into the system with the aid of an external force. In other words, here we test the implementation of the forcing schemes of Eswaran & Pope (1988) (henceforth EP) and Alvelius (1999) (henceforth AL).

The tests with the forcing of EP were aimed at reproducing the results of Jiménez *et al.* (1993), for which reference data of homogeneous isotropic turbulence at different Re_λ is available[1]. Our numerical experiments focused on two different Reynolds numbers, namely $Re_\lambda \approx 60$ and $Re_\lambda \approx 140$, and compared the probability density functions (pdfs) of the longitudinal and the transversal velocity gradients as well as the energy spectra. In all cases, the numerical resolution is chosen such that $\kappa_{max}\eta \approx 1.5$, where η is the Kolmogorov lengthscale.

Through a proper choice of the free parameters, the simulation was setup such that the desired final Re_λ were obtained. After an initial transient that lasted about 6 large-eddy turnover times, the velocity field reached a statistically steady-state. Figures 2.7 and 2.8 show the results for $Re_\lambda \approx 60$ and $Re_\lambda \approx 140$. The present results are in excellent agreement with the reference data although the reference data was computed using a different forcing scheme (negative viscosity). Further and in agreement with theory, two behaviors for the probability density functions are also salient: the skewed behavior in the pdf of $\partial u/\partial x$, and the fact that both pdfs become wider for increasing Re_λ.

The test for the forcing scheme of AL was instead aimed at showing that a constant power input is achieved throughout the entire simulation time. For this purpose, we considered a simple case with relatively low Re_λ. To excite a fluid initially at rest, we imposed a force in the wavenumber range $[0, 4\kappa_0]$ with $\kappa_f/\kappa_0 = 2$. After the usual transient, a statistically steady-state was reached with $Re_\lambda \approx 68$.

Figure 2.9 shows the temporal evolution of the individual terms in the turbulence kinetic equation:

$$\frac{\mathrm{d}K}{\mathrm{d}t} = -\langle \varepsilon_\nu \rangle_{\mathcal{L}} + \langle \varepsilon_I \rangle_{\mathcal{L}} \,. \tag{2.55}$$

In a steady-state, i.e., $\mathrm{d}K/\mathrm{d}t = 0$, the box-averaged power input $\langle \varepsilon_I \rangle_{\mathcal{L}}$ must bal-

[1] Processed data for the basic flow statistics is available at http://torroja.dmt.upm.es/turbdata/agard/

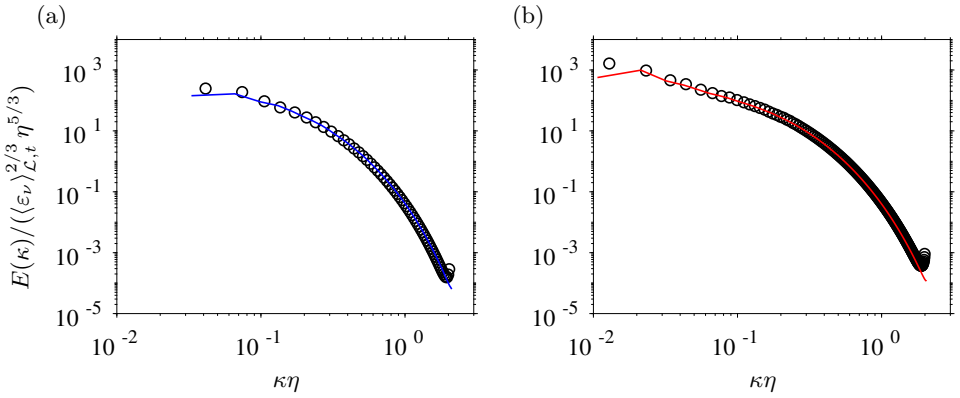

Figure 2.7: Spherically averaged energy spectrum for the validation runs with (a) $Re_\lambda \approx 60$ (—) and with (b) $Re_\lambda \approx 140$ (—). The symbols represent the reference data from Jiménez *et al.* (1993) at approximately the same Re_λ (o).

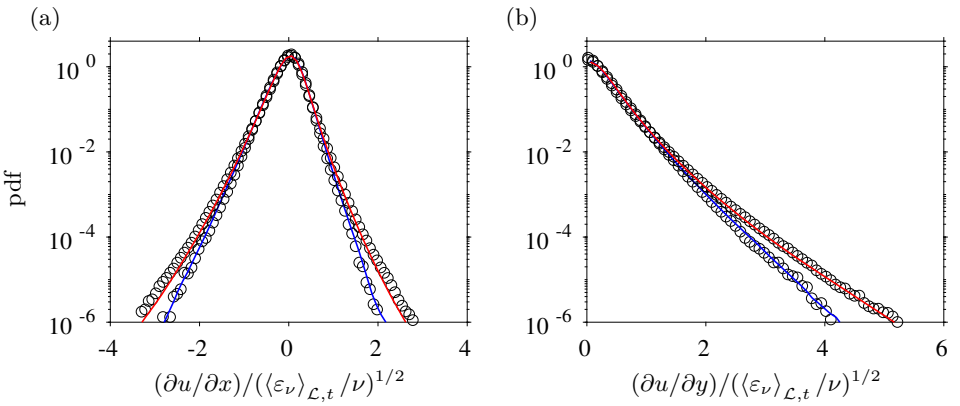

Figure 2.8: Probability density function of the transversal and longitudinal (a) velocity derivatives (b). The solid line denotes results obtained with our numerical tool for $Re_\lambda \approx 60$ (—) and $Re_\lambda \approx 140$ (—). The symbols denote the data from Jiménez *et al.* (1993) (o) at approximately the same Re_λ.

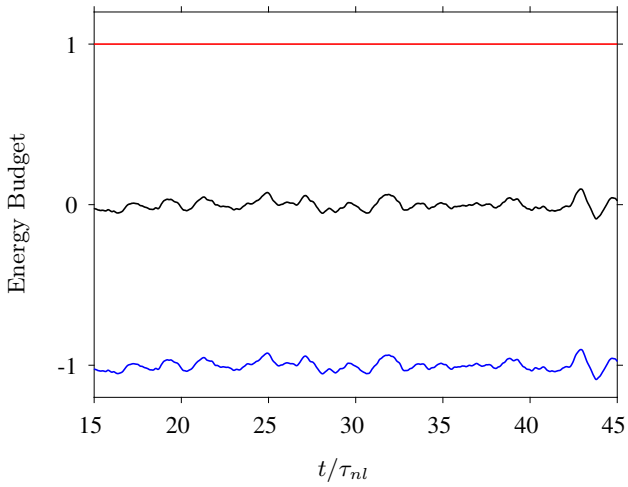

Figure 2.9: Turbulence kinetic energy budget showing the constant energy input rate when the forcing scheme of Alvelius (1999) is used. Solid lines denote the individual contributions due to: $\langle \varepsilon_I \rangle_{\mathcal{L}}$ (—), $-\langle \varepsilon_\nu \rangle_{\mathcal{L}}$ (—) and $\mathrm{d}\langle K \rangle_{\mathcal{L}}/\mathrm{d}t$ (—).

ance the box-averaged viscous dissipation $\langle \varepsilon_\nu \rangle_{\mathcal{L}}$. These features are salient in Fig. 2.9, and the departure from null for the time derivative of $\langle K \rangle_{\mathcal{L}}$ is approximately $0.001\ \langle \varepsilon_\nu \rangle_{\mathcal{L},t}$.

Although omitted, we have also compared the results with the forcing scheme of Alvelius (1999) with equivalent runs and the forcing scheme of Eswaran & Pope (1988). The results are of the same quality as the ones presented in Figs. 2.7 and 2.8.

2.2.5. Vortex Blob in a Rotating Flow

Last, we consider a canonical example that illustrates one of the most basic features of rotating flows, i.e., the elongation of the flow structures along the axis of rotation. This example considers the time evolution of a compact eddy and it is taken from Yoshimatsu *et al.* (2011). The equation of motion is the inviscid linearized Navier-Stokes equations in a rotating frame of reference, i.e.,

$$\frac{\partial \mathbf{u}}{\partial t} + 2(\boldsymbol{\Omega} \times \mathbf{u}) = -\nabla q, \tag{2.56}$$

in which $\boldsymbol{\Omega} = \Omega\, \tilde{\mathbf{e}}_3$, where $\tilde{\mathbf{e}}_3$ is the unit vector along the third Cartesian direction. The numerical domain is defined as $\mathcal{L} = [0, 2\pi] \times [0, 2\pi] \times [0, 2\pi]$, and the initial velocity field is

$$\mathbf{u}(\mathbf{x}, 0) = \left\{ B \exp\left[-((x_1 - \pi)^2 + (x_2 - \pi)^2 + (x_3 - \pi)^2)/\delta^2 \right] \right\} \tilde{\mathbf{e}}_3 \times \mathbf{r}, \tag{2.57}$$

with $\mathbf{r} = x_i \tilde{\mathbf{e}}_i$ the position vector, $B = 5$ and $\delta = 0.2$. The velocity field consists of an array of periodic vortex blobs which has maximum strength at the center of

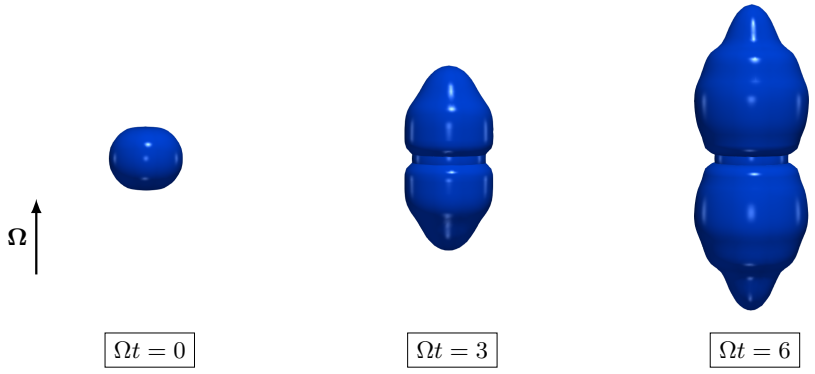

Figure 2.10: Time evolution of a vortex blob in a rotating environment reproducing the results from (Yoshimatsu *et al.*, 2011). The surface represents iso-contours of the enstrophy $\mathcal{E} = (\omega_i \omega_i)^{1/2}$ for the mean value plus 3 standard deviations.

the computational domain, and which is exponentially damped towards the domain boundaries.

For the numerical test, we integrated Eq. (2.56) in time using the integrating factor approach as described in Section 2.1.3 and compared the results with the data from Yoshimatsu *et al.* (2011). Note that as explained in Section 2.1.1, the pressure q can be eliminated from the set of equations. In Fig. 2.10, we show the iso-surfaces of the enstrophy $\mathcal{E} = \omega^2$ for three instants of time which correspond to the onset of the simulation and two subsequent time instants. As time evolves, the initial compact vortex blob stretches along the axis of rotation and attains a columnar shape. This behavior is essentially the same as described in Yoshimatsu *et al.* (2011), and both results agree visually very well. Nevertheless, a more strict way to validate our numerical results is to quantify the elongation of the flow structures and compare numerical values.

As been discussed in detail by those authors, the integral lengthscale based on the enstrophy is a good candidate for measuring the spatial dimension of the flow structures in this case. The integral lengthscale of enstrophy along a specific direction is defined in terms of the two-point correlation as

$$\ell_\beta(\mathcal{E}) = \frac{1}{\langle \mathcal{E}' \mathcal{E}' \rangle_{\mathcal{L}}} \int_0^\infty \langle \mathcal{E}'(\mathbf{x}, t) \mathcal{E}'(\mathbf{x} + r\tilde{\mathbf{e}}_\beta, t) \rangle_{\mathcal{L}} \, \mathrm{d}r, \tag{2.58}$$

where the prime denotes the fluctuations with respect to box averages, i.e., $\mathcal{E}' = \mathcal{E} - \langle \mathcal{E} \rangle_{\mathcal{L}}$, and $\beta \in \{1, 2, 3\}$ is any of the Cartesian directions. As seen from Fig. 2.11, our numerical results for the temporal evolution of $\ell_\beta(\mathcal{E})$ for $\beta = 2$ and $\beta = 3$ is in solid agreement with the data from Yoshimatsu *et al.* (2011).

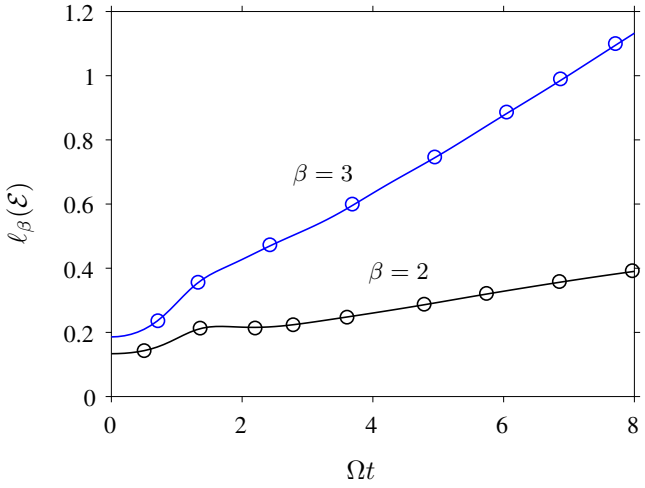

Figure 2.11: Time evolution of the enstrophy based integral lengthscales. The black and blue markers are the reference data from Yoshimatsu *et al.* (2011) (o ; o), whereas the blue and black solid lines (— ; —) represent the results obtained with our numerical tool.

3

Suppressing the Inverse Energy Cascade

Pestana, T. & Hickel, S. 2019 Regime transition in the energy cascade of rotating turbulence. *Physical Review E* **99** (5), 053103

3.1. Background

The energy cascade is the fundamental mechanism in turbulent flows that describes the energy exchange between the various scales of motion (Frisch, 1995). A forward cascade from large to small scales is commonly observed in three-dimensional (3D) flows, whereas an inverse energy cascade from small towards large scales is the hallmark of two-dimensional (2D) flows (Alexakis & Biferale, 2018; Boffetta & Ecke, 2012). Predicting the energy cascade direction, therefore, requires anticipating if, for a given set of control parameters, the resulting flow field resembles best 3D or 2D flow dynamics. In lack of analytical predictions, a typical approach consists of carefully designing numerical experiments, where the system's parameters are individually varied to produce a phase transition diagram. Throughout this study we consider a large number of forced direct numerical simulations (DNS) and analyze the influence of geometric confinement and system rotation on the cascade direction in homogeneous rotating turbulence.

Inertial waves, i.e. plane wave solutions to the linearized Navier-Stokes equations, can modulate the energy transfer in rotating turbulence (Godeferd & Moisy, 2015; Greenspan, 1968). By considering high rotation rates and exploiting the fact that rotating turbulence is a multi-timescale problem, Waleffe (1993) suggested that the nonlinear dynamics are modified by wave interactions. Resonant wave interactions can explain the favored energy transfer towards horizontal modes, whereas non-resonant wave interactions are considered to damp and inhibit the triadic interactions typical of homogeneous turbulence (Cambon *et al.*, 1997; Smith & Waleffe, 1999). This mechanism also persists at lower rotation rates due to homochirical interactions that transfer energy into the plane orthogonal to the rotation axis (Buzzicotti *et al.*, 2018). As a consequence, when rotating homogeneous flows are forced at wavenumber κ_f, the injected energy can cascade both to larger ($\kappa < \kappa_f$) and smaller scales ($\kappa > \kappa_f$); this is hereafter referred to as split energy cascade. These findings help to explain the preferential upscale of energy typically found in numerical and experimental investigations of rotating turbulent flows (Delache *et al.*, 2014; Mininni *et al.*, 2009, 2012; Moisy *et al.*, 2011; Smith & Waleffe, 1999; Yeung & Zhou, 1998). Nevertheless, we must bear in mind that a large network of triadic interactions as in the Navier-Stokes equations can evolve differently than a set of isolated triads, as previously pointed out in Refs. (Linkmann & Dallas, 2017; Moffatt, 2014).

Among different theories that elucidate the phenomenon of rotating turbulence, the work of Galtier (2003) is regarded as an important contribution. Based on wave turbulence theory, which deals with systems where interactions are governed by waves, he derived scaling laws for the energy spectrum. These laws were also shown to follow from phenomenological arguments for the spectral transfer time — a typical energy transfer timescale. For infinitely large domains, as required by wave turbulence theory (Nazarenko, 2011), the weak inertial-wave theory of Galtier (2003) predicts that energy cascades forward and to small scales. However, a passage from a split to a forward energy cascade system by approaching the large-box limit has not yet been confirmed by DNS.

In the absence of rotation, however, the geometrical dimensions of the system itself influences the energy cascade direction. Using a two-dimensional two-component

(2D2C) horizontal force, Smith *et al.* (1996) and Celani *et al.* (2010) found that the ratio L_3/ℓ_f, where L_3 is the vertical domain extension and ℓ_f is the forcing lengthscale, is a governing control parameter. They showed that large L_3/ℓ_f results in a forward energy cascade, whereas inverse energy transfer was triggered and split the energy cascade for $L_3/\ell_f \leq 1/2$. More recently, numerical simulations by Benavides & Alexakis (2017) explored transitions in a thin layer of fluid subjected to free-slip boundary conditions. Transition from a forward to a split energy cascade was shown to be critical and depend on the ratio of forcing lengthscale to wall separation.

Regime transitions in rotating homogeneous turbulence are therefore affected by geometrical dimensions and rotation rate. Deusebio *et al.* (2014) studied hyperviscous fluids in rotating small aspect ratio domains subjected to 2D2C forcing and found that large rotation rates as well as small L_3/ℓ_f suppress enstrophy production and induce an inverse energy cascade. Their data proves, at least for weak rotation rates, that transition from a split to a forward cascade is possible by controlling either rotation rate or domain size. For strong rotation, however, almost the entire injected energy cascaded inversely. Although transition was not observed, they hypothesized that it could still take place for sufficiently large L_3/ℓ_f. This conjecture, however, remains to be verified by either forcing smaller flow scales or by increasing the domain size (Seshasayanan & Alexakis, 2018).

The present work sheds light on the question whether a transition from a split to a forward cascade system always exists in forced homogeneous rotating turbulence. We conduct a systematic parametric study that covers several rotation rates and an unprecedented range of geometric confinements by considering strongly elongated domains and large forcing wavenumbers κ_f. This new database is complementary to previous studies, which focused on the confinement induced transition in smaller and shallower domains. Through large-scale forcing, we construct isotropic flow fields that are posteriorly subjected to rotation. Differently from previous studies, we employ a three-dimensional three-component (3D3C) forcing scheme that by design provides a constant energy input independent of the velocity field. We believe this results in a neater and more general framework where anisotropy originates solely from rotation.

3.2. Description of the Simulations

We solve the incompressible Navier-Stokes equations in a frame rotating at rate $\boldsymbol{\Omega}$:

$$\nabla \cdot \mathbf{u} = 0, \tag{3.1}$$

$$\frac{\partial \mathbf{u}}{\partial t} + (2\,\boldsymbol{\Omega} + \boldsymbol{\omega}) \times \mathbf{u} = -\nabla q + \nu \nabla^2 \mathbf{u} + \mathbf{f}. \tag{3.2}$$

Here, $\mathbf{u}$, $\boldsymbol{\omega}$ and $\mathbf{f}$ are velocity, vorticity and an external force, respectively. The reduced pressure into which the centrifugal force is incorporated is given by q, and ν denotes the kinematic viscosity. Equations (3.1) and (3.2) are discretized in space by a dealiased Fourier pseudo-spectral method (2/3-rule) in a triply-periodic domain of size $2\pi\mathcal{L}_1 \times 2\pi\mathcal{L}_2 \times 2\pi\mathcal{L}_3$ (Orszag, 1969; Pekurovsky, 2012). The rotation axis is assumed aligned with the vertical direction, i.e. $\boldsymbol{\Omega} = \Omega\,\hat{\mathbf{e}}_3$, and we restrict ourselves

Table 3.1: List of the performed Direct Numerical Simulations at $Re_\varepsilon \approx 55$ ($Re_\lambda \approx 68$) for different $\kappa_f \mathcal{L}_\parallel$, $\kappa_f \mathcal{L}_\perp$ and Ro_ε.

Case	$\kappa_f \mathcal{L}_\perp$	$\kappa_f \mathcal{L}_\parallel$	A_r	N_p
`kf02-a01` [a]	2	2	1	192^3
`kf04-a01` [a]	4	4	1	384^3
`kf04-a02` [b]	4	8	2	$384^2 \times 768$
`kf04-a04` [b]	4	16	4	$384^2 \times 1536$
`kf04-a08` [b]	4	32	8	$384^2 \times 3072$
`kf04-a16` [b]	4	64	16	$384^2 \times 6144$
`kf04-a32` [b]	4	128	32	$384^2 \times 12288$
`kf08-a01` [a]	8	8	1	768^3
`kf08-a02` [b]	8	16	2	$768^2 \times 1536$
`kf08-a04` [b]	8	32	4	$768^2 \times 3072$
`kf08-a08` [c]	8	64	8	$768^2 \times 6144$
`kf08-a16` [b]	8	128	16	$768^2 \times 12288$
`kf16-a01` [a]	16	16	1	1536^3
`kf16-a02` [b]	16	32	2	$1536^2 \times 3072$
`kf16-a04` [b]	16	64	4	$1536^2 \times 6144$
`kf32-a01` [b]	32	32	1	3072^3

[a] $Ro_\varepsilon \approx 0.31,\ 0.06$
[b] $Ro_\varepsilon \approx 0.06$
[c] $Ro_\varepsilon \approx 1.25,\ 0.63,\ 0.31,\ 0.27,\ 0.24,\ 0.22,\ 0.19,\ 0.16,\ 0.14,\ 0.11,\ 0.09,\ 0.08,\ 0.06$

to cases where the domain size in the direction perpendicular to the axis of rotation are equal: $\mathcal{L}_1 = \mathcal{L}_2 = \mathcal{L}_\perp = 1$. Accordingly, $\mathcal{L}_\parallel$ replaces $\mathcal{L}_3$ to denote the domain size in the direction parallel to the rotation axis, and can be arbitrarily chosen. We use Rogallo's integrating factor technique for exact time integration of the viscous and Coriolis terms and a third-order Runge-Kutta scheme for the nonlinear terms (Morinishi *et al.*, 2001; Rogallo, 1977).

The external force $\mathbf{f}$ injects energy to the system at rate ε_I, see Alvelius (1999). The force's spectrum $F(\kappa)$, from which $\mathbf{f}$ in Eq. (3.2) is assembled, is Gaussian distributed, centered around a wavenumber κ_f and has standard deviation $c = 0.5$: $F(\kappa) = A \exp(-(\kappa - \kappa_f)^2/c)$.

For given κ_f and c, the prefactor A is uniquely determined from the desired energy input rate ε_I. In the absence of rotation, we obtain isotropic velocity fields and a balance between energy input rate and viscous dissipation, i.e. $\varepsilon_I = \varepsilon_\nu$. This forcing scheme ensures through projection that the force and velocity field are uncorrelated at every instant of time (Alvelius, 1999). As a consequence, ε_I is solely determined by the force-force correlation and is independent of the velocity field. Thus, we can define a priori true control parameters from which the governing non-dimensional numbers are derived.

The domain size, $\mathcal{L}_\parallel$ and $\mathcal{L}_\perp$, the forcing wavenumber κ_f, the viscosity ν, the rotation rate Ω and the energy input rate ε_I can all be freely chosen. Regarding ε_I,

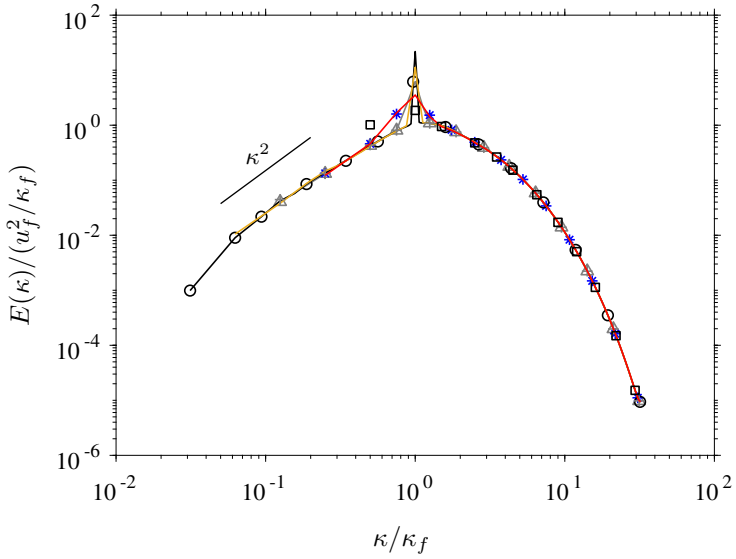

Figure 3.1: Three-dimensional spherically averaged energy spectrum of the initial condition: `kf02-a01` (□), `kf04-a01` (—), `kf08-a01` (+), `kf16-a01` (—), `kf32-a01` (-⊖-), `kf04-a32` (∗), `kf08-a16` (△)

it could be additionally decomposed in three contributions stemming from the power injected in each direction. However, because the forcing is isotropic, it is sufficient to consider the total power input ε_I only. These six parameters $\{\kappa_f, \nu, \varepsilon_I, \Omega, \mathcal{L}_\perp, \mathcal{L}_\parallel\}$ form the set of true control parameters and are the basis for the non-dimensional similarity numbers. The characteristic length, velocity and time-scale follow naturally as $\ell_f = \kappa_f^{-1}$, $u_f = \varepsilon_I^{1/3}\ \kappa_f^{-1/3}$, and $\tau_f = \kappa_f^{-2/3}\ \varepsilon_I^{-1/3}$, respectively. In addition, a timescale based on the rotation rate is taken as $\tau_\Omega = 1/(2\Omega)$.

The Reynolds and Rossby numbers are now unambiguously defined as

$$Re_\varepsilon = \frac{\varepsilon_I^{1/3}\ \kappa_f^{-4/3}}{\nu} \quad \text{and} \quad Ro_\varepsilon = \frac{\kappa_f^{2/3}\varepsilon_I^{1/3}}{2\Omega}. \tag{3.3}$$

From the problem's geometry and the forcing wavenumber, we define two other non-dimensional numbers, i.e. $\kappa_f\mathcal{L}_\perp$ and $\kappa_f\mathcal{L}_\parallel$. Hence, we obtain a set of four independent governing non-dimensional numbers that fully describes our numerical experiments: Re_ε, Ro_ε, $\kappa_f\mathcal{L}_\perp$ and $\kappa_f\mathcal{L}_\parallel$. As the final goal is to investigate dimensional and rotational effects on forced homogeneous rotating turbulence, we fix Re_ε and allow Ro_ε, $\kappa_f\mathcal{L}_\parallel$ and $\kappa_f\mathcal{L}_\perp$ to vary. We remark that this set is not unique and other non-dimensional groups exist. For instance, Re_ε and Ro_λ could be combined to form the micro-scale Rossby number $Ro_\lambda = Re_\varepsilon^{1/2}Ro_\lambda$ (ratio of rotation and Kolmogorov timescale (Cambon *et al.*, 1997)) or $\kappa_f\mathcal{L}_\parallel$ and $\kappa_f\mathcal{L}_\perp$ could be related to obtain the domain's aspect ratio $A_r = \mathcal{L}_\parallel/\mathcal{L}_\perp$.

Initial conditions were generated by performing DNS of non-rotating forced isotropic turbulence. We started from a zero-velocity field and marched in time until a fully developed steady-state was achieved. After the initial transient statistics, were sampled over at least $24\,\tau_f$, corresponding to approximately ten large-eddy turnover times. Following this procedure, a reference isotropic solution was computed for every entry in Table 4.2.

The initially imposed $Re_\varepsilon \approx 55$ ultimately led to homogeneous non-rotating turbulent fields with a characteristic Taylor micro-scale Reynolds number $Re_\lambda \approx 68$. The spatial resolution in terms of the Kolmogorov lengthscale η was kept constant throughout this study, i.e. $\kappa_{max}\eta \approx 1.5$, where κ_{max} is the largest represented wavenumber. For the case with largest $\kappa_f\mathcal{L}_\parallel$, the integral lengthscale in the direction of rotation is about 600 times smaller than the respective domain size.

Figure 3.1 compares the 3D spherically averaged energy spectrum $E(\kappa)$ for cases with aspect ratio $A_r = 1$, which contain "`a01`" in its name description, and two additional simulations with $A_r = 16$ and $A_r = 32$ (cases `kf04-a32` and `kf08-a16` in Table 4.2). This data proves the equivalence between initial conditions for DNS forced at different wavenumbers and those computed with distinct $\kappa_f\mathcal{L}_\parallel$ and $\kappa_f\mathcal{L}_\perp$. We find that the energy spectra perfectly coincide and that $E(\kappa)$ scales best with κ^2 at wavenumbers $\kappa < \kappa_f$, in agreement with Dallas *et al.* (2015). The obtained isotropic velocity fields were used as initial condition for the simulations with different rotation rates. The statistical variability of the results for small domains was reduced by ensemble averaging. For the smallest domain `kf02-a01` we ensemble averaged 10 independent realizations and cases `kf04` with $A_r > 1$ are averages of 3 realizations. For all other cases, the data represents a single numerical experiment.

3.3. Results

First we assess the effects of geometrical dimension and rotation on the time evolution of box-averaged kinetic energy K and viscous dissipation ε_ν. The non-dimensional geometric parameters $\kappa_f\mathcal{L}_\perp$ and $\kappa_f\mathcal{L}_\parallel$ are varied for two fixed rotation rates: weak ($Ro_\varepsilon = 0.31$; Fig. 3.2) and strong ($Ro_\varepsilon = 0.06$; Fig. 3.3). Additionally, for a fixed and large domain, $\kappa_f\mathcal{L}_\perp = 8$ and $\kappa_f\mathcal{L}_\parallel = 64$ (case `kf08-a08`; Fig. 3.4), we investigate the Rossby number range $0.06 < Ro_\varepsilon < 1.25$. For more details about the simulation parameters, please refer to Table 4.2.

All cases undergo a transient of roughly $10\,\tau_f$ from the onset of rotation (Figs. 3.2 to 3.4), and converge towards a unique solution for sufficiently large $\kappa_f\mathcal{L}_\parallel$. We find that the results are independent of the transversal domain size for $\kappa_f\mathcal{L}_\perp \geq 4$; see Fig. 3.3, where the lines for different $\kappa_f\mathcal{L}_\perp$ and identical $\kappa_f\mathcal{L}_\parallel$ coincide. Departing from an isotropic state, where the energy cascade is strictly forward ($\varepsilon_\nu/\varepsilon_I = 1$), ε_ν decreases monotonically until it is lowest at approximately $3\,\tau_f$ (Figs. 3.2b, 3.3b and 3.4b). For fixed Ro_ε, Figs. 3.2b and 3.3b show that both $\kappa_f\mathcal{L}_\perp$ and $\kappa_f\mathcal{L}_\parallel$ have no influence on the minimum of ε_ν. On the other hand, Fig. 3.4b suggests a direct proportionality between the minimum value of ε_ν and Ro_ε.

After $t \approx 3\,\tau_f$, ε_ν increases towards ε_I. Nevertheless, the strong and weak rotation cases lead to a different final state for ε_ν. While increasing $\kappa_f\mathcal{L}_\parallel$ restores $\varepsilon_\nu = \varepsilon_I$ for the weak rotating case (Fig. 3.2b), the imbalance $\varepsilon_\nu < \varepsilon_I$, although lower

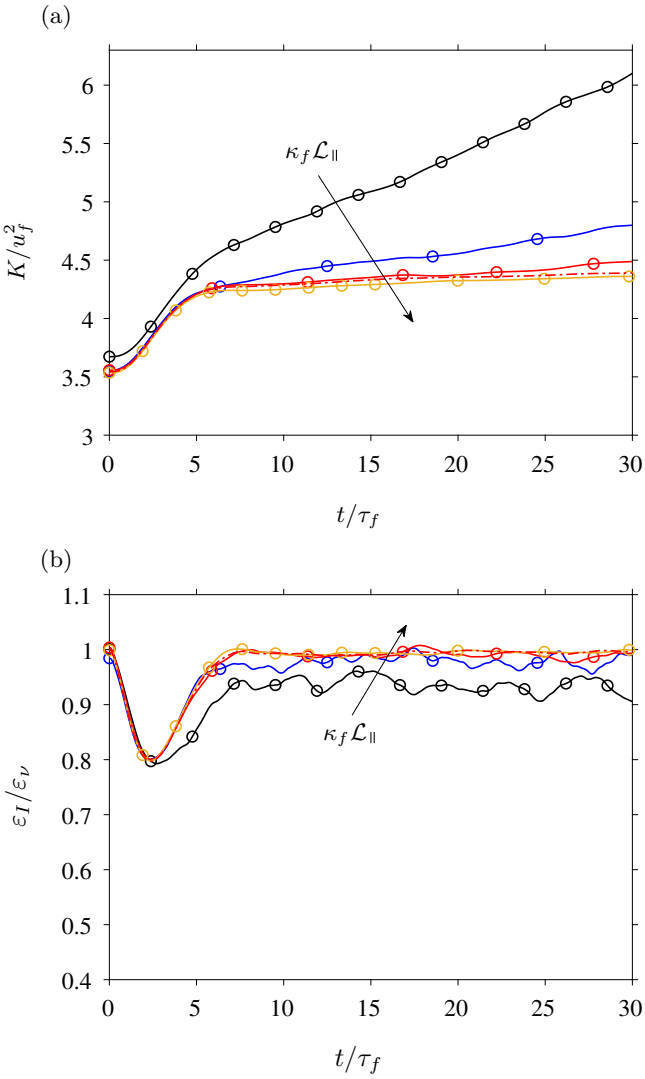

Figure 3.2: Time evolution of box-averaged kinetic energy (a) and energy dissipation rate (b) for $Ro_\varepsilon \approx 0.31$ (weak rotation). Lines corresponding to same $\kappa_f\mathcal{L}_\perp$ are grouped by color: $\kappa_f\mathcal{L}_\perp = 2$ (■), $\kappa_f\mathcal{L}_\perp = 4$ (■), $\kappa_f\mathcal{L}_\perp = 8$ (■), $\kappa_f\mathcal{L}_\perp = 16$ (■). Lines corresponding to the same A_r are grouped by line types: $A_r = 1$ (—o—), $A_r = 8$ (- - -), cf. Table 4.2.

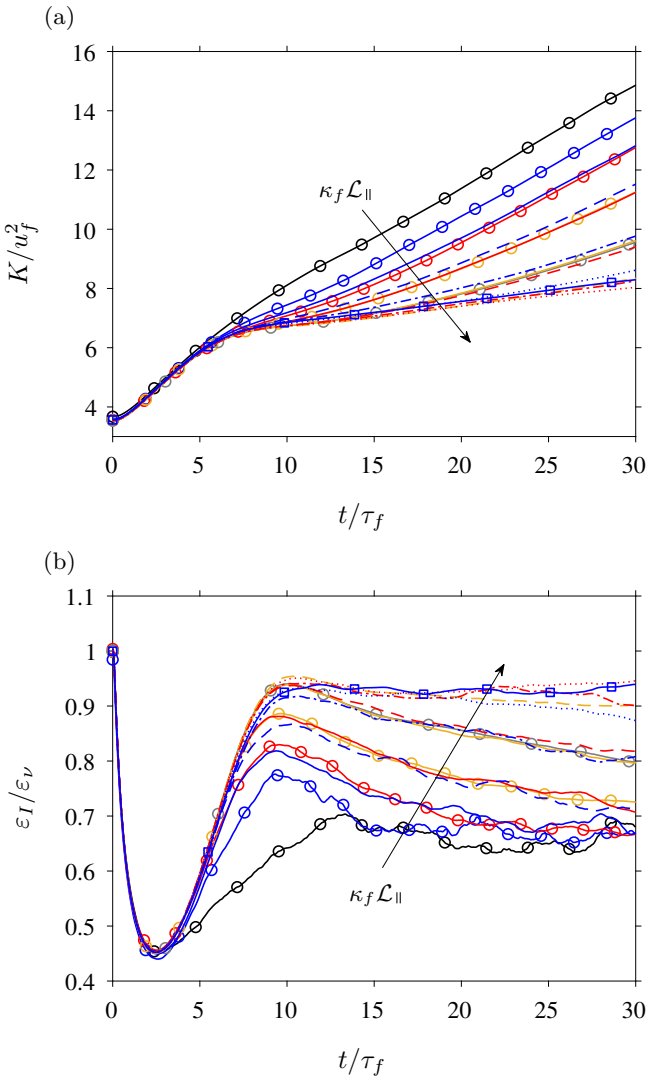

Figure 3.3: Time evolution of box-averaged kinetic energy (a) and energy dissipation rate (b) for $Ro_\varepsilon \approx 0.06$ (strong rotation). Lines corresponding to same $\kappa_f\mathcal{L}_\perp$ are grouped by color: $\kappa_f\mathcal{L}_\perp = 2$ (■), $\kappa_f\mathcal{L}_\perp = 4$ (■), $\kappa_f\mathcal{L}_\perp = 8$ (■), $\kappa_f\mathcal{L}_\perp = 16$ (■), $\kappa_f\mathcal{L}_\perp = 32$ (■). Lines corresponding to the same A_r are grouped by line types: $A_r = 1$ (—o—), $A_r = 2$ (—), $A_r = 4$ (- - -), $A_r = 8$ (– – –), $A_r = 16$ (·····), $A_r = 32$ (—□—), cf. Table 4.2.

than $0.075\,\varepsilon_I$ for $\kappa_f\mathcal{L}_\parallel = 128$, persists up to the final time for the strong rotating case (Fig. 3.3b). Similarly to Fig. 3.2b, increasing Ro_ε reestablishes a forward energy cascade for a fixed domain size (Fig. 3.4b). After the initial transient ($t > 10\,\tau_f$), ε_ν follows mostly a slow linear decay (Fig. 3.3b) or remains nearly constant (Figs. 3.2b and 3.4b). Consequently, K, which evolves in time as $\mathrm{d}K/\mathrm{d}t = \varepsilon_I - \varepsilon_\nu$, grows quasi-linearly (Figs. 3.2a, 3.3a and 3.4a). Based on this idea we define the inverse energy flux $\varepsilon_{inv} = \varepsilon_I - \varepsilon_\nu$ from the imbalance between energy injection rate and viscous dissipation. To estimate ε_{inv}, which is equal to the local slope of $K(t)$, a linear least-square fit is applied to $15\,\tau_f < t < 30\,\tau_f$ in the time evolution of K (Figs. 3.2a, 3.3a and 3.4a). The r.m.s. residual between the actual and fitted data indicates that the linear regression model is appropriate. For the worst case, `kf04-a08`, the r.m.s. residual is 0.65% of the mean value. Assuming that the linear law is exact and the noise is essentially Gaussian, one obtains 0.0004 for the standard error of the slope coefficient. Results for the inverse energy flux are thus shown in Figs. 3.5 and 3.6 in form of a phase transition diagram.

From Fig. 3.5a, we see that the inverse energy flux ε_{inv} decreases monotonically with $\kappa_f\mathcal{L}_\parallel$ for both $Ro_\varepsilon \approx 0.31$ and $Ro_\varepsilon \approx 0.06$. Moreover, results for the strong rotating case suggest that increasing $\kappa_f\mathcal{L}_\perp$ while retaining $\kappa_f\mathcal{L}_\parallel$ leads to negligible differences in ε_{inv} — see the overlapping circles with different colors for $Ro_\varepsilon \approx 0.06$. Transition from a split to a forward cascade system occurs gradually. For $Ro_\varepsilon \approx 0.31$ and $\kappa_f\mathcal{L}_\parallel = 64$ less than $0.004\,\varepsilon_I$ is transferred in the inverse direction, whereas for $Ro_\varepsilon \approx 0.06$ a split cascade is still present at $\kappa_f\mathcal{L}_\parallel = 128$. For a fixed domain size with $\kappa_f\mathcal{L}_\perp = 8$ and $\kappa_f\mathcal{L}_\parallel = 64$ (case `kf08-a08`; Fig. 3.5b), ε_{inv} is continuously suppressed for increasing Ro_ε and transition to a forward cascade system occurs in the vicinity of $Ro_\varepsilon = 1$.

A question that follows from these results is for which combination of governing non-dimensional parameters regime transition occurs. From literature, a possible criteria is $Ro_\varepsilon\kappa_f\mathcal{L}_\parallel = C$, where C is a constant (Alexakis & Biferale, 2018; Seshasayanan & Alexakis, 2018). To test this hypothesis, Fig. 3.6 presents the data from Fig. 3.5, but juxtaposed in a single diagram and scaled accordingly with $Ro_\varepsilon\kappa_f\mathcal{L}_\parallel$. The curves for different Ro_ε do not line up; hence, this criteria disagrees with our data. A discussion on a possible reason is given in the next section.

Now we turn our attention to the influence of $\kappa_f\mathcal{L}_\parallel$ and $\kappa_f\mathcal{L}_\perp$ on the spectral energy flux and energy spectra. Hereafter we present results for the strong rotating case with $Ro_\varepsilon \approx 0.06$ only, as differences are more pronounced than in the weak rotating case. Although we show instantaneous data at $t = 30\,\tau_f$, the trend described in what follows also holds for other instants of time. Conservation of energy requires the portion of the injected energy that is not dissipated to be accumulated. By analyzing the spectral energy flux $\Pi(\kappa)$, we find that the net energy transfer $T(\kappa) = -\mathrm{d}\Pi/\mathrm{d}\kappa$ is positive for $\kappa < \kappa_f$. In other words, wavenumbers in this range gain energy and we observe an upscale energy transfer. Evidence is presented in Fig. 3.7, which also highlights how sensitive $\Pi(\kappa)$ is with respect to changes in $\kappa_f\mathcal{L}_\parallel$ and $\kappa_f\mathcal{L}_\perp$. In this regard, Fig. 3.7a, where $\kappa_f\mathcal{L}_\parallel$ is constant and $\kappa_f\mathcal{L}_\perp = \{8, 16, 32\}$, shows that the shape of $\Pi(\kappa)$ remains unaltered for different $\kappa_f\mathcal{L}_\perp$. On the other hand, varying $\kappa_f\mathcal{L}_\parallel$ from 16 to 64 while $\kappa_f\mathcal{L}_\perp$ is constant, reduces the magni-

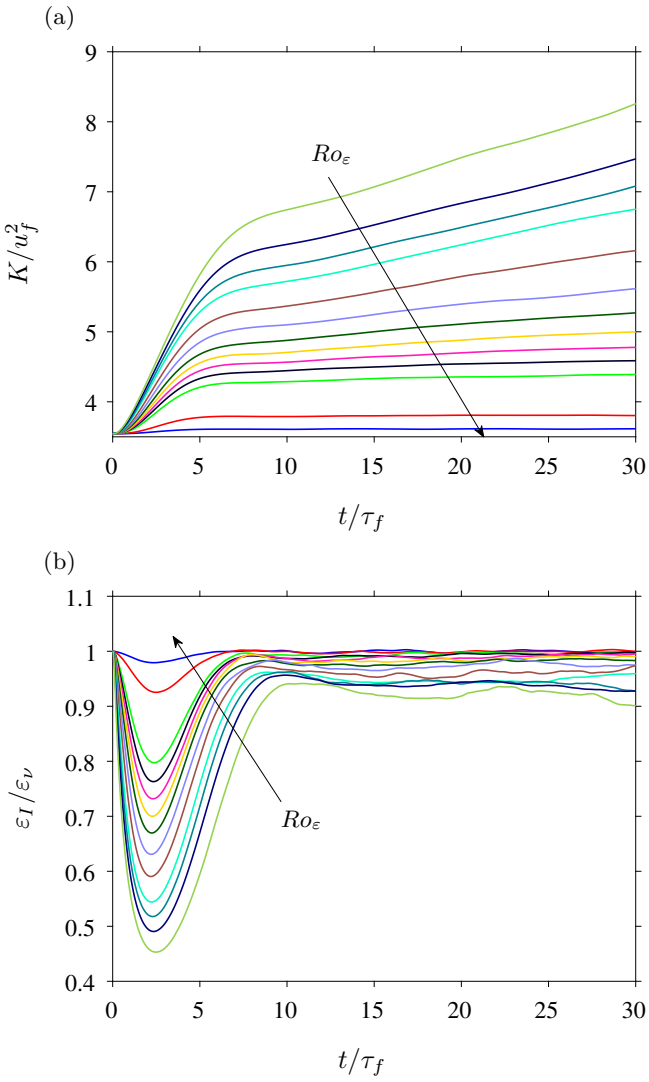

Figure 3.4: Time evolution of box-averaged kinetic energy (a) and energy dissipation rate (b) for $\kappa_f \mathcal{L}_\perp = 8$ and $\kappa_f \mathcal{L}_\parallel = 64$. Different line colors correspond to the range $0.06 < Ro_\varepsilon < 1.25$, see Table 4.2.

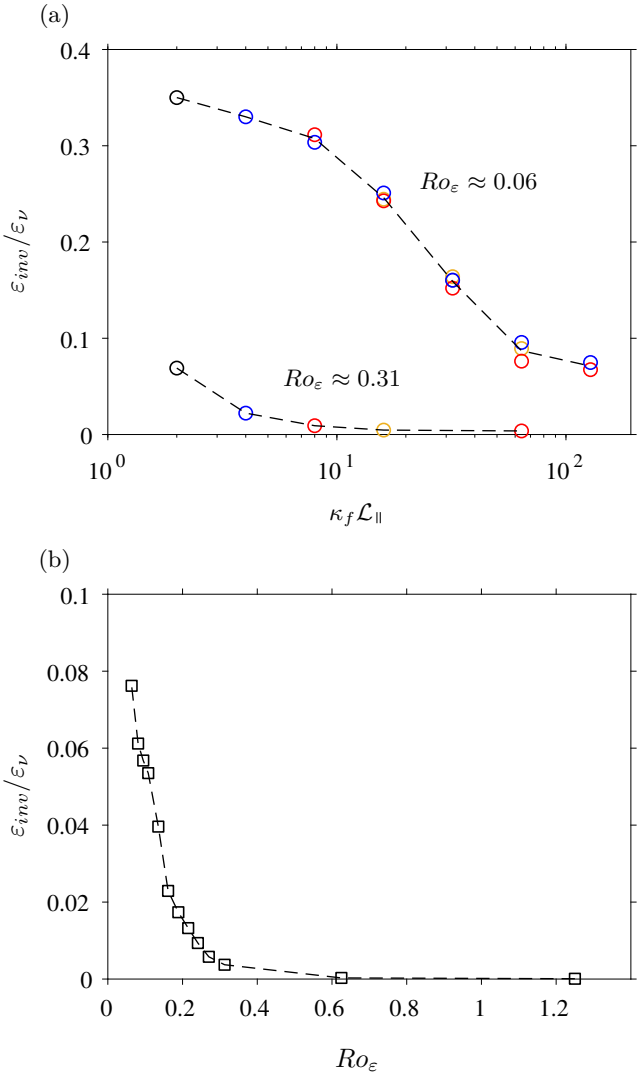

Figure 3.5: Phase transition diagram for weak and strong rotation and varying geometrical dimensions (a) and for constant geometrical dimension and varying Ro_ε (b). Color scheme of (a) is the same as in Fig. 3.3. In (a), the data point for $\kappa_f \mathcal{L}_\perp = \kappa_f \mathcal{L}_\parallel = 32$ (case `kf32-a01`) is almost identical to case `kf04-a08` ($\kappa_f \mathcal{L}_\perp = 4$; $\kappa_f \mathcal{L}_\parallel = 32$), and is therefore not visible.

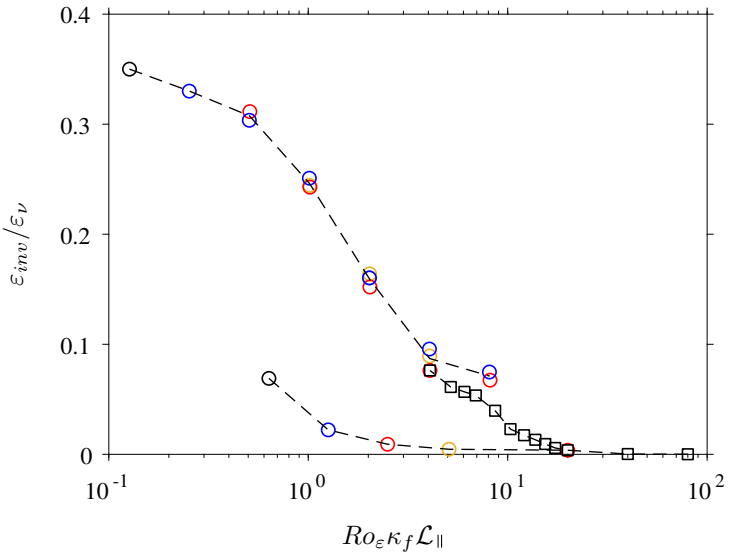

Figure 3.6: Phase transition diagram in terms of combined control parameter $Ro_\varepsilon \kappa_f \mathcal{L}_\parallel$ for all data points of Fig. 3.5. Colored circles represent data from Fig. 3.5a, and squares data from Fig. 3.5b.

tude of the inverse energy flux and the range of wavenumbers for which an upscale energy transfer takes place, see Fig. 3.7b. Therein, greater values of $\kappa_f \mathcal{L}_\parallel$ are also associated with an enhanced spectral energy flux for $\kappa > \kappa_f$. This is a consequence of the fixed energy input rate ε_I, which causes the step in $\Pi(\kappa)$ at $\kappa = \kappa_f$ to be the same for all cases.

The three-dimensional energy spectra $E(\kappa)$ for the same cases are shown in Fig. 3.8. Additionally, the energy spectrum of case `kf32-a01` with $\kappa_f \mathcal{L}_\parallel = \kappa_f \mathcal{L}_\perp = 32$ from Fig. 3.1 at the onset of rotation is included as reference. Figure 3.8a reinforces that $\kappa_f \mathcal{L}_\parallel$ dictates the degree of energy accumulation, as the curves for different $\kappa_f \mathcal{L}_\perp$ and constant $\kappa_f \mathcal{L}_\parallel$ overlap. In agreement with results in Fig. 3.7 for $\Pi(\kappa)$, we observe significantly higher levels of energy for $\kappa < \kappa_f$ with respect to the isotropic reference spectrum. These are reduced for increasing $\kappa_f \mathcal{L}_\parallel$, see Fig. 3.8b.

As for the distribution of energy in terms of $\kappa_\parallel$ and $\kappa_\perp$, Fig. 3.9 presents the two-dimensional energy spectrum $E(\kappa_\perp, \kappa_\parallel)$. Results are shown exclusively for case `kf32-a01` with $\kappa_f \mathcal{L}_\perp = \kappa_f \mathcal{L}_\parallel = 32$, as it contains most large scale resolution. The energy spectrum is non-dimensionalized with $2\pi\kappa_\perp$, in such a way that contour levels of isotropic spectra appear as circles centered at the origin. In agreement with previous works, Fig. 3.9 confirms that the kinetic energy has the tendency to accumulate at lower $\kappa_\parallel/\kappa_f$. Hence, $E(\kappa_\perp, \kappa_\parallel)$ is anisotropic and contour levels display an elliptical shape with major axis aligned with the $\kappa_\perp$-direction. This is observed even for high wavenumbers and suggests that all scales of motion are influenced by rotation; indeed, for this case, $\kappa_\Omega \eta = 1.1$, where $\kappa_\Omega = (\Omega^3/\varepsilon_I)^{1/2}$ is the Zeman wavenumber (Delache *et al.*, 2014). At the same time, the energy input

remains isotropic. See the inset for the imprint of the isotropic forcing scheme, which delineates the bright area located at $\kappa_\parallel^2 + \kappa_\perp^2 = \kappa_f^2$. In addition, we see higher energy levels in the vicinity of $\kappa_\parallel/\kappa_f = 0$.

An anisotropic distribution of energy is predicted by the weak inertial-wave theory, which suggests that the energy spectrum has the form $E(\kappa_\perp, \kappa_\parallel) \sim \kappa_\perp^{-5/2}\kappa_\parallel^{-1/2}$ (Galtier, 2003). To test if our data presents any sign of this scaling law, we show in Fig. 3.10 instantaneous one-dimensional energy spectra along the perpendicular and parallel directions, i.e. $E_\perp(\kappa_\perp)$ and $E_\parallel(\kappa_\parallel)$ for $t = 0, 10, 20$ and $30\,\tau_f$. Figure 3.10a shows that energy levels increase progressively for $\kappa_\perp < \kappa_f$, whereas for $\kappa_\perp > \kappa_f$, the distribution of energy is nearly unaltered. Also for $\kappa_\perp > \kappa_f$, we observe that a narrow wavenumber range develops from the initial state and approaches best a $\kappa_\perp^{-5/2}$ scaling law. Regarding $E_\parallel(\kappa_\parallel)$, Fig. 3.10b, the energy content for $\kappa_\parallel > \kappa_f$ is significantly lower than at the onset of rotation. This corroborates the idea that rotation lessen the flow field dependency on the direction parallel to the rotation axis. As time evolves, the range $\kappa_\parallel < \kappa_f$ resembles best a $\kappa_\parallel^{-1/2}$ scaling law for all time instants. We emphasize that this result is essentially different from predictions of the weak inertial-wave theory, as the latter estimates $E(\kappa_\parallel) \sim \kappa_\parallel^{-1/2}$ for $\kappa_\parallel$ larger than the forcing wavenumber.

3.4. Discussion

We attribute the fact that ε_{inv} does not become exactly zero for $Ro_\varepsilon \approx 0.31$ to two effects. First, the simulations considered in this study are limited to $Re_\lambda \approx 68$. A higher Reynolds number could contribute to a stronger forward cascade, possibly reducing ε_{inv} to zero. Second, although effects of the geometric non-dimensional parameter $\kappa_f\mathcal{L}_\perp$ are minor, the results hint that larger values of $\kappa_f\mathcal{L}_\perp$ could also contribute to a reduction of ε_{inv}. In this manner, an indefinite increase of $\kappa_f\mathcal{L}_\perp$ could potentially change the phase diagram in the vicinity of $\varepsilon_{inv}/\varepsilon_I = 0$, and could cause regime transition to be sharp rather than smooth. The recent study of Benavides & Alexakis (2017) has shown that a continuous increase of horizontal domain dimensions shifts the transition behavior for thin layer turbulence from smooth to critical. We hope that further studies will help to fill the parameter space for higher Reynolds numbers and even longer domain sizes.

For $Ro_\varepsilon \approx 0.06$, we agree with Deusebio *et al.* (2014) and believe that a continuous increase of $\kappa_f\mathcal{L}_\parallel$ would result in transition to a forward energy cascade. Nevertheless, results for the weak case suggest a slow-paced transition and significantly larger values for $\kappa_f\mathcal{L}_\parallel$ might be required. Interestingly, the transition of ε_{inv} in terms of $\kappa_f\mathcal{L}_\parallel$ resembles a logistic function, similar to what has been found for regime transitions in thin layer turbulence (Benavides & Alexakis, 2017).

In search of a criteria for transition between a forward and a split cascade system, we made an attempt to express $\varepsilon_{inv}/\varepsilon_I$ for all parameter points as a function of $Ro_\varepsilon\kappa_f\mathcal{L}_\parallel$. As the different curves do not overlap, we believe that a criteria for transition should stem from a more general match of timescales. A criteria such as $Ro_\varepsilon\kappa_f\mathcal{L}_\parallel = C$, can be obtained by requiring the slowest inertial wave frequency $1/\tau_w = 2\Omega/\kappa_f\mathcal{L}_\parallel$ and the eddy turnover frequency $u_f\kappa_f$ at the forcing scale to be

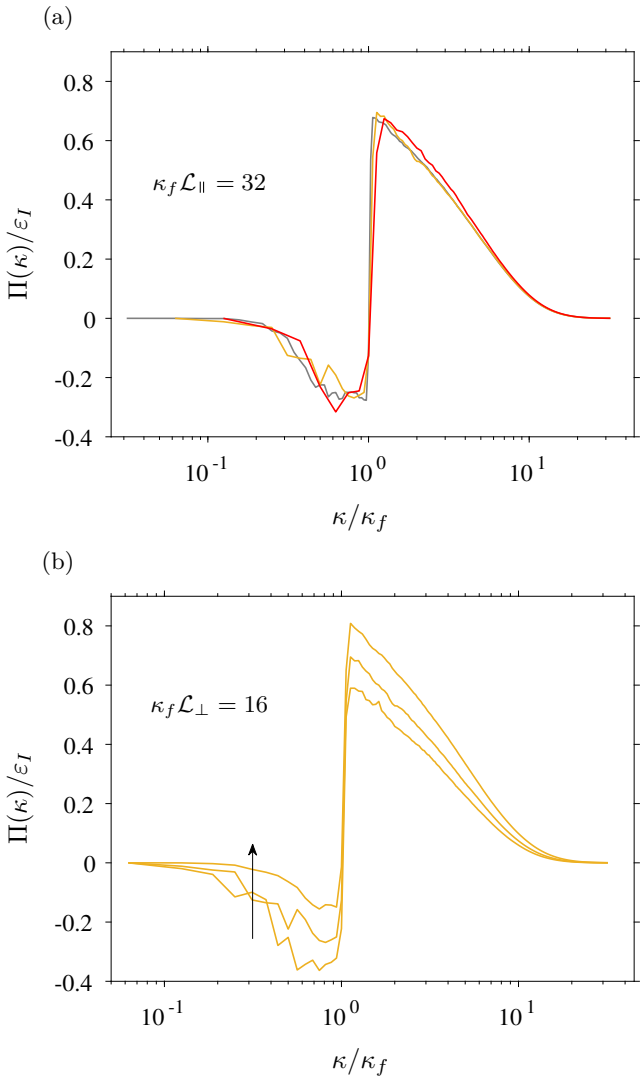

Figure 3.7: Spectral energy flux for $Ro_\varepsilon \approx 0.06$ and cases with $\kappa_f \mathcal{L}_\parallel = 32$ (a) and $\kappa_f \mathcal{L}_\perp = 16$ (b). In (a), $\kappa_f \mathcal{L}_\perp = 8$ (—), $\kappa_f \mathcal{L}_\perp = 16$ (—) and $\kappa_f \mathcal{L}_\perp = 32$ (—). In (b), $\kappa_f \mathcal{L}_\parallel = 16, 32$ and 64 (—). Arrow denotes the direction of increase.

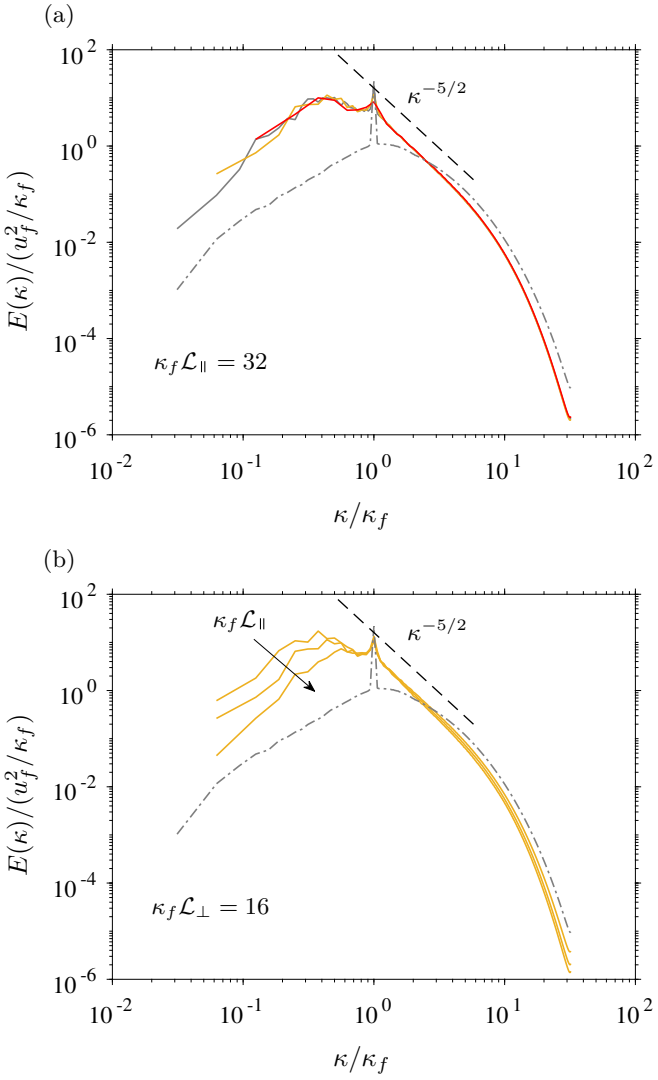

Figure 3.8: Three-dimensional spherically averaged energy spectrum for $\kappa_f\mathcal{L}_\parallel = 32$ (a) and $\kappa_f\mathcal{L}_\perp = 16$ (b) with $Ro_\varepsilon \approx 0.06$. Line styles are the same as in Fig. 3.7, apart from the reference energy spectrum of Fig. 3.1 with $\kappa_f\mathcal{L}_\perp = \kappa_f\mathcal{L}_\parallel = 32$ (– – –).

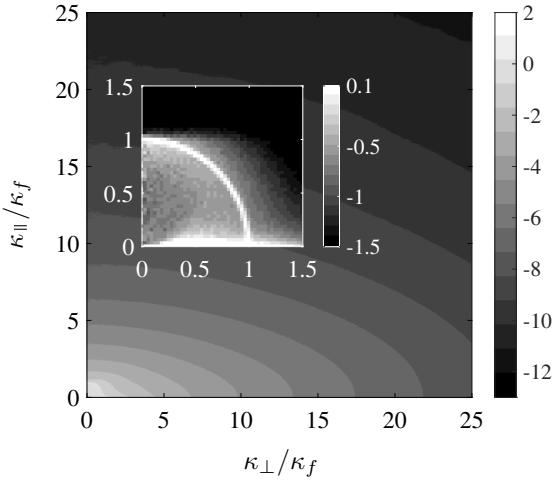

Figure 3.9: Two-dimensional energy spectrum $E(\kappa_\perp, \kappa_\parallel)$ for $Ro_\varepsilon \approx 0.06$ with $\kappa_f \mathcal{L}_\perp = \kappa_f \mathcal{L}_\parallel = 32$ (case `kf32-a01`) at $t = 30\,\tau_f$. Data is normalized by $(2\pi\kappa_\perp)\, u_f^2/\kappa_f^3$ and plotted in $\log_{10}$. The inset highlights the region around the forcing wavenumber: $\kappa_\perp/\kappa_f < 1.5$ and $\kappa_\parallel/\kappa_f < 1.5$.

of same order (Alexakis & Biferale, 2018; Seshasayanan & Alexakis, 2018). Alternatively, we can frame the problem within the idea that rotation alters the spectral transfer time τ_s at which energy is transferred to smaller scales. Thus, it follows that $\varepsilon_\nu \sim u_\ell^2/\tau_s$, with u_ℓ a velocity scale characteristic of eddies of size ℓ, and $\tau_s \sim \tau_{nl}^2/\tau_3$ (Galtier, 2003; Kraichnan, 1965; Zhou, 1995). Here, $\tau_{nl} \sim \ell/u_\ell$ is the nonlinear timescale and τ_3 is the relaxation time of triple velocity correlations. The relaxation time in isotropic turbulence simplifies to τ_{nl} to recover the dissipation law, i.e. $\varepsilon_\nu \sim u_\ell^3/\ell$.

Now the condition $Ro_\varepsilon \kappa_f \mathcal{L}_\parallel = C$ can be obtained by requiring $\varepsilon_\nu = \varepsilon_I$, and assuming $u \sim u_f$, $\tau_{nl} \sim \tau_f$ and $\tau_3 \sim \tau_w$. So, $Ro_\varepsilon \kappa_f \mathcal{L}_\parallel = C$ is equivalent to state that in the presence of rotation the nonlinear timescale remains of the order of τ_f, and that the relaxation timescale τ_3 is given by the inverse of the slowest inertial wave frequency, i.e $\tau_3 \sim \tau_w$. A generalization of the previous reasoning would be to consider a τ_{nl} obtained from a measured velocity quantity, like the r.m.s velocity, and the lengthscale ℓ possibly as $\ell_\perp$, as the triadic interactions are expected to be depleted in the direction parallel to the rotation axis (Nazarenko & Schekochihin, 2011). The relaxation time τ_3 could be sought as a function of both τ_f and τ_Ω. In this manner, more general criteria like $Ro_\varepsilon^a (\kappa_f \mathcal{L}_\parallel)^b = C$ arise, where a and b are yet undetermined exponents.

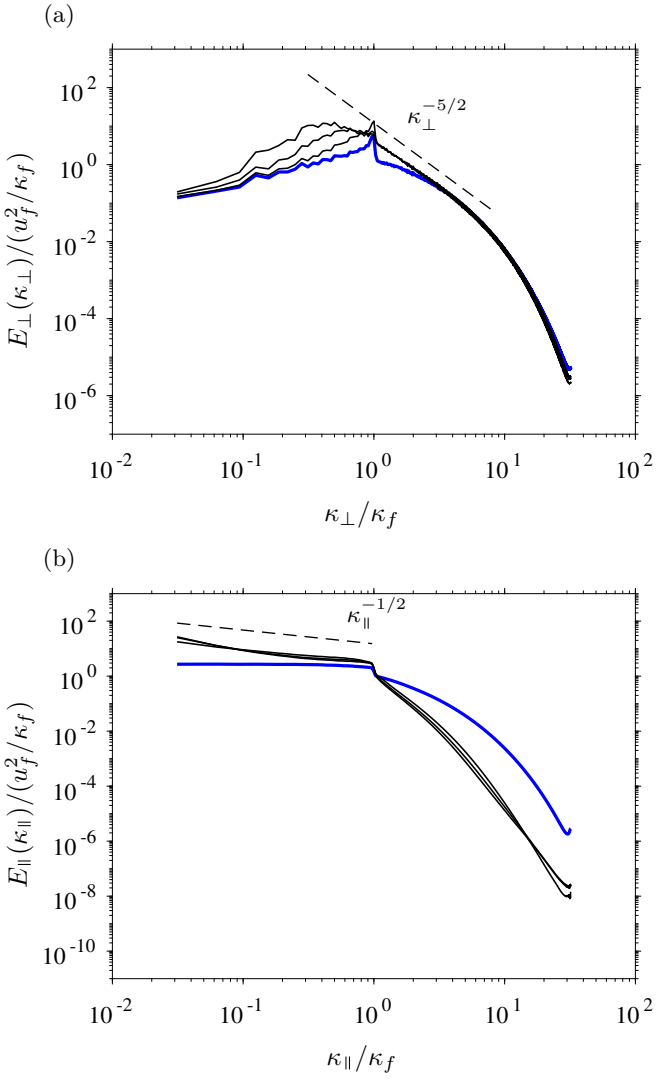

Figure 3.10: One-dimensional energy spectra for $Ro_\varepsilon \approx 0.06$ and $\kappa_f\mathcal{L}_\perp = \kappa_f\mathcal{L}_\parallel = 32$ (case `kf32-a01`) along directions $\kappa_\perp$ (a) and $\kappa_\parallel$ (b). Lines represent the time evolution of the energy spectrum: $t = 0$ (—), and $t = 10, 20$ and $30\,\tau_f$ (—). A reference line for the scaling laws that best agrees with the presented data is also shown (- - -).

4

Scaling Laws for the Energy Dissipation Rate

Pestana, T. & Hickel, S. 2020 Rossby Number Effects on Columnar Eddy Formation and the Energy Dissipation Law in Homogeneous Rotating Turbulence. *Journal of Fluid Mechanics* **885**, A7

4.1. Background

Many geophysical and man-made fluid flows are affected by the interaction between system rotation and turbulence (Boffetta & Ecke, 2012; Greenspan, 1968). An idealized approach to study rotating turbulence consists in observing the evolution of an initial homogeneous isotropic flow in a non-inertial rotating frame of reference. This way, early experimental studies already revealed the main features of homogeneous rotating turbulence (e.g., Jacquin *et al.* (1990)), although a few of them did not meet the condition for homogeneity (e.g., Hopfinger *et al.* (1982); Ibbetson & Tritton (1975)). When the Rossby number (Ro) was sufficiently small, i.e., the ratio of the rotational time scale and the turbulent time scale, it was observed that the energy dissipation rate ε_ν is reduced with respect to the reference non-rotating isotropic case. Further, the typical cloud of isotropic eddies found in isotropic flows was strained, and grew in size to towards an array of flow structures aligned with the axis of rotation (columnar eddies). These two features are the traits of rotating turbulence and have been observed and analyzed in a number of recent experimental and numerical investigations, see, e.g., van Bokhoven *et al.* (2009); Delache *et al.* (2014); Mininni *et al.* (2009, 2012); Moisy *et al.* (2011); Staplehurst *et al.* (2008), or Godeferd & Moisy (2015) for a review. Yet, it remains poorly understood how they are quantitatively related.

For homogeneous isotropic turbulence, it is well accepted that the energy dissipation rate scales as $\varepsilon_\nu \sim u_0^3/l_0$, where u_0 and l_0 are an integral velocity scale and an integral length scale, respectively (Batchelor, 1953). This relation can be interpreted on the basis of phenomenological arguments as follows. Let us first assume that ε_ν depends on an energy content, say u_0^2, and on a time scale τ_s characteristic of the downscale energy transfer: the spectral transfer time. In homogeneous isotropic turbulence, the only time scale available to be taken as τ_s is the time scale characteristic of the non-linear triadic interactions, τ_{nl}. If we further assume that $\tau_{nl} \sim l_0/u_0$, where l_0 is the typical size of the energy containing eddies, the dissipation law for homogeneous isotropic turbulence can be recovered. But for systems in which other time scales are also relevant, as is the case of magnetohydrodynamics (MHD) or rotating turbulence, τ_s might be different from τ_{nl}. Within the context of MHD, Kraichnan (1965) considered that τ_s is in fact composed of two time scales of opposing effects; the non-linear time scale τ_{nl}, which can also be considered as the measure of how fast triple velocity correlations are built-up, and the decorrelation time scale τ_3, which indicates how fast these correlations decay in time. Exploiting these ideas, he suggested that the energy flux (energy dissipation rate) was directly proportional to τ_3 and inversely proportional to τ_{nl}.

Following this line of thought, one alternative to relate the energy dissipation rate to the formation of columnar eddies in rotating turbulence is to find approximations for τ_{nl} and τ_3 that involve integral length scales and the rotation rate. However, this is not straightforward. First, owing to the fact that the distribution of energy is not isotropic, two distinct integral length scales in homogeneous rotating turbulence exist, i.e., $\ell_{0\perp}$ and $\ell_{0\parallel}$, which can be defined along the directions normal and parallel to the axis of rotation, respectively. Which one then is relevant to form τ_{nl}? Second, how does τ_3 depend on the time scale imposed by the background rotation, i.e., $\tau_\Omega =$

$1/(2\Omega)$? In literature, a few dissipation laws for homogeneous rotating turbulence have emerged from attempts to estimate the energy flux (Baqui & Davidson, 2015; Galtier, 2003; Nazarenko & Schekochihin, 2011; Zhou, 1995). Despite the efforts to account for the effects of rotation, results available in current literature regarding whether these laws generally hold or if they specifically apply to a Rossby number range are inconclusive or even inconsistent.

Another problem, which is rather more technical, is the fact that the elongated columnar flow structures restrict the maximum observation time in Direct Numerical Simulations (DNS) of rotating turbulence. Because simulations of homogeneous flows often consider periodic boundary conditions, a too small domain size with respect to the characteristic size of the living eddies can modulate the dynamics of the large scales and constrain their size. An obvious solution to circumvent this problem and avoid numerical artifacts is either to consider larger domains or to generate flow fields in which the characteristic eddy size is smaller than the domain size. For example, in the DNS by Baqui & Davidson (2015) the initial characteristic eddy size was 50 times smaller than the domain size. However, when $Ro \ll 1$ this may be still insufficient and limit the simulation to a few eddy-turnover times.

In view of these shortcomings, this study addresses the two following questions:

(i) What is the influence of the Rossby number in the growth rate of the columnar eddies, in the absence of confinement effects?

(ii) Can we approximate the energy dissipation rate in homogeneous rotating turbulence in a fashion similar to homogeneous isotropic turbulence, i.e., in terms of a velocity scale, an integral length scale and the rotation rate?

For this purpose, we consider the evolution of an initial homogeneous isotropic flow field in a rotating frame of reference. We conduct a systematic study that consists of 21 different rotation rates, thus covering a wide range of Rossby numbers. Our DNS are carried out in an elongated computational domain that is about 340 times larger than the initial characteristic size of the flow structures, provides enough room for the columnar eddies to grow freely. All simulations are performed with a stochastic large-scale forcing that injects energy at a constant rate. The forcing scheme is three-dimensional, isotropic, and at all times uncorrelated with the velocity field. To the best of our knowledge, the present database is unprecedented.

This work is organized as follows. In Section 4.2, the governing equations and the numerical method is detailed together with a description of the simulations and their physical parameters. The influence of the Rossby number in the growth rate of the columnar eddies is investigated in Section 4.3, and approximations for the energy dissipation rate are finally offered in Section 4.4.

4.2. Numerical Set-up

4.2.1. Governing Equations and Numerical Method

We consider an incompressible fluid in a triply periodic rectangular cuboid of size $2\pi\mathcal{L}_1 \times 2\pi\mathcal{L}_2 \times 2\pi\mathcal{L}_3$ that rotates around $\mathbf{\Omega}$. Fluid motion is assumed governed by

$\kappa_f\mathcal{L}_\perp$	$\kappa_f\mathcal{L}_\parallel$	$(2\pi\mathcal{L}_\perp)/\ell_\perp^{\mathrm{iso}}$	$(2\pi\mathcal{L}_\parallel)/\ell_\parallel^{\mathrm{iso}}$	τ_f/T_e	Re_ε	Re_λ	N_p
8	64	39.9	342.5	2.36	55.05	68	$768^2 \times 6144$

Table 4.1: Numerical and physical parameters of the initial homogeneous isotropic turbulent flow field used for the runs with rotation.

the incompressible Navier-Stokes equations:

$$\nabla \cdot \mathbf{u} = 0, \tag{4.1}$$

$$\frac{\partial \mathbf{u}}{\partial t} + (2\,\boldsymbol{\Omega} + \boldsymbol{\omega}) \times \mathbf{u} = -\nabla q + \nu \nabla^2 \mathbf{u} + \mathbf{f}. \tag{4.2}$$

Here, $\mathbf{u}$, $\boldsymbol{\omega}$ and $\mathbf{f}$ are the velocity, the vorticity and an external force, respectively. Time is denoted by t, the reduced pressure, into which the centrifugal force is incorporated, is given by q, and ν denotes the kinematic viscosity of the fluid. The rotation vector $\boldsymbol{\Omega}$ is chosen to be aligned with the 3-direction, i.e, $\boldsymbol{\Omega} = (0, 0, \Omega)$, where Ω is the rotation rate. The horizontal dimensions of the rectangular cuboid (normal to the axis of rotation) are equal, $\mathcal{L}_\perp = \mathcal{L}_1 = \mathcal{L}_2 = 1$, whereas the vertical extension (parallel to the axis of rotation) is by a factor of 8 larger than the horizontal dimensions, i.e. $\mathcal{L}_\parallel = \mathcal{L}_3 = 8$.

The numerical method is essentially the same as in Pestana & Hickel (2019*b*). Equations (4.1) and (4.2) are solved by a de-aliased Fourier pseudo-spectral method (2/3-rule), where the spatial gradients are computed with the aid of fast Fourier transforms (Pekurovsky, 2012), and the time-stepper employs exact integration of the viscous and Coriolis forces (Morinishi *et al.*, 2001; Rogallo, 1977) together with a third-order low-storage Runge-Kutta scheme for the non-linear terms. The number of degrees of freedom is $N_p = 768^2 \times 6144$, which has been increased accordingly to the extended domain size to resolve all scales of motion. The smallest and largest resolved wavenumber per direction is $\kappa_{min,i} = 1/\mathcal{L}_i$ and $\kappa_{max,i} = N_{p,i}/(3\mathcal{L}_i)$, respectively, where the index $i = \{1, 2, 3\}$ denotes the different directions.

In all simulations considered in this study, energy is injected through the external force $\mathbf{f}$ on right-hand-side of Eq. (4.2). The forcing scheme is designed as proposed in Alvelius (1999); the force spectrum $F(\kappa)$ is Gaussian with standard deviation $c = 0.5$ and is centered around the forcing wavenumber κ_f:

$$F(\kappa) = A \exp(-(\kappa - \kappa_f)^2/c). \tag{4.3}$$

In Eq. (4.3), the prefactor A, which controls the amplitude of $F(\kappa)$ can be determined *a priori* to the simulation and allow us to fix the power input ε_I. This is only possible because this forcing scheme ensures that the force-velocity correlation is at all time instants zero. As a consequence, the injected power is an exclusive product of the force-force correlation, which is directly related to $F(\kappa)$. For more details about the forcing scheme and its design, please refer to (Alvelius, 1999).

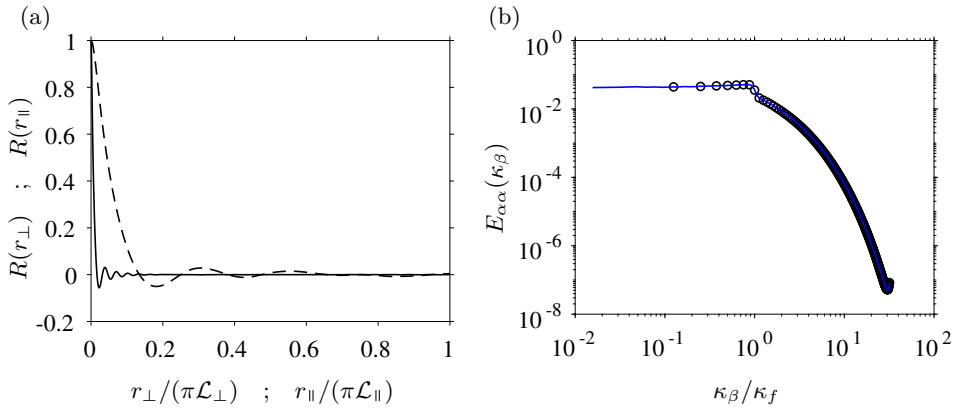

Figure 4.1: Two-point velocity correlations showing the ratio domain size to characteristic size of the flow structures in the different directions, and one-dimensional energy spectra showing that the initial conditions are indeed isotropic. (a) Normal $R(r_\perp)$ (- - -) and parallel $R(r_\parallel)$ (—) velocity two-point correlations. (b) Perpendicular and parallel one-dimensional energy spectra: $\alpha = 1$; $\beta = 3$; $E_{11}(\kappa_3)$ (—) and $\alpha = 3$; $\beta = 1$; $E_{33}(\kappa_1)$ (o)

4.2.2. Description of the Simulations and Physical Parameters

To describe the considered physical problem, we are free to choose 6 control parameters. These form the set $\{\kappa_f, \varepsilon_I, \nu, \mathcal{L}_\parallel, \mathcal{L}_\perp, \Omega\}$, which involves two physical units. Thus, a total of 4 non-dimensional numbers is sufficient to describe the numerical experiment. The governing non-dimensional numbers can be built by combination of the free control parameters. For instance, using κ_f and ε_I and assuming that the constant of proportionality is 1, we can construct the velocity scale $u_f = \varepsilon_I^{1/3}\kappa_f^{-1/3}$ and the time scale $\tau_f = \kappa_f^{-2/3}\varepsilon_I^{-1/3}$. Additionally, a characteristic length scale can be taken as $\ell_f = 1/\kappa_f$. Hence, the Reynolds and the Rossby number are defined as

$$Re_\varepsilon = \frac{\varepsilon_I^{1/3}\kappa_f^{-4/3}}{\nu} \quad \text{and} \quad Ro_\varepsilon = \frac{\kappa_f^{2/3}\varepsilon_I^{1/3}}{2\Omega}. \tag{4.4}$$

The two other governing non-dimensional numbers are formed by combining the forcing wavenumber with the geometric dimensions of the domain to yield $\kappa_f\mathcal{L}_\perp$ and $\kappa_f\mathcal{L}_\parallel$. The 4 non-dimensional numbers, $\{Re_\varepsilon, Ro_\varepsilon, \kappa_f\mathcal{L}_\parallel, \kappa_f\mathcal{L}_\perp\}$, whose definitions have been borrowed from Seshasayanan & Alexakis (2018), form the parameter space henceforth used to characterize the simulations performed in this study. Note, however, that this set of non-dimensional parameters is not unique. For instance, one may combine Re_ε and Ro_ε to form the micro-scale Rossby number $Ro_\lambda = Re_\varepsilon^{1/2}Ro_\varepsilon$, which represents the ratio of rotation and Kolmogorov time scales, or express the geometric dimensions in terms of the domain aspect ratio $A_r = \mathcal{L}_\parallel/\mathcal{L}_\perp$.

Another important parameter is the Zeman wavenumber $\kappa_\Omega = (\Omega^3/\varepsilon_I)^{1/2}$, which indicates the wavenumber range for which rotational effects are relevant (Delache *et al.*, 2014; Zeman, 1994). The Zeman wavenumber is also automatically set by

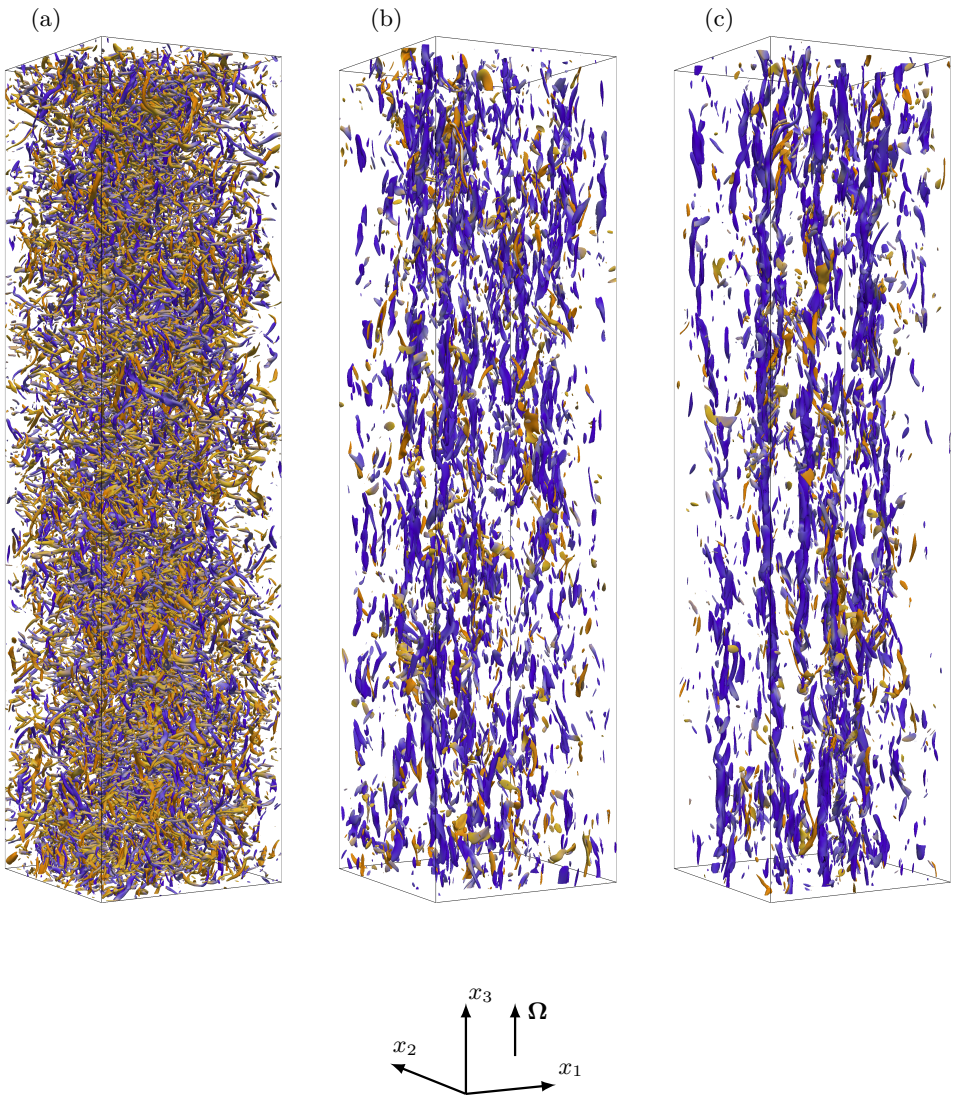

Figure 4.2: Flow field visualization of a sub-set of the computational domain (1/16 of the entire computational domain), showing half of the horizontal domain extension and 1/4 of the vertical domain size: $[0, \pi] \times [0, \pi] \times [0, 4\pi]$. Iso-contours of the Q-criterion (Hunt *et al.*, 1988) colored by the normalized projection of the vorticity vector along the axis of rotation, i.e., $\boldsymbol{\omega} \cdot \mathbf{e}_{\parallel} / \|\boldsymbol{\omega}\|$. Blue colors indicates structures that rotate in the same sense as $\mathbf{\Omega}$ (counter-clockwise), whereas orange colors indicate the opposite sense of rotation (clockwise). (a) Isotropic initial condition; (b) and (c) correspond to the run with $Ro_{\varepsilon} = 0.06$ at later time instants after the onset of rotation, i.e., $t = 10.5\,\tau_f$ and $t = 20\,\tau_f$, respectively.

	Run	Colormap	Ro_ε	Ro_λ	$\kappa_\Omega\eta$	κ_Ω/κ_f
R1	run01		1.54	11.42	0.009	0.19
	run02		1.25	9.28	0.013	0.25
	run03		1.00	7.42	0.017	0.35
	run04		0.87	6.45	0.022	0.44
	run05		0.77	5.71	0.026	0.52
	run06		0.69	5.12	0.031	0.62
	run07		0.63	4.64	0.035	0.72
	run08		0.56	4.12	0.042	0.85
	run09		0.47	3.45	0.055	1.11
	run10		0.39	2.91	0.071	1.44
R2	run11		0.31	2.32	0.100	2.02
	run12		0.27	2.01	0.124	2.52
	run13		0.24	1.79	0.148	2.99
	run14		0.22	1.60	0.175	3.55
	run15		0.19	1.40	0.213	4.31
	run16		0.16	1.20	0.270	5.46
	run17		0.14	1.00	0.352	7.12
	run18		0.11	0.80	0.492	9.95
	run19		0.09	0.70	0.599	12.12
	run20		0.08	0.60	0.759	15.34
	run21		0.06	0.47	1.088	21.99

Table 4.2: Numerical and physical parameters for the DNS of homogeneous rotation turbulence at distinct rates of rotation. The runs that exhibit similar dynamics are collected together in groups, namely R1 and R2.

fixing the aforementioned parameters as $Ro_\varepsilon = (\kappa_f/\kappa_\Omega)^{2/3}/2$.

A posteriori, we can compute the usual physical parameters that describe the flow field. The box-averaged kinetic energy K is given by $\langle u_i u_i \rangle_{\mathcal{L}}/2$, where the operator $\langle \cdot \rangle_{\mathcal{L}}$ denotes volume averages, and the viscous dissipation rate is $\varepsilon_\nu = 2\nu \langle S_{ij} S_{ij} \rangle_{\mathcal{L}}$, where $S_{ij} = (\partial u_{i,j} + \partial u_{j,i})/2$ is the strain-rate tensor. From K, we define the r.m.s. velocity $u' = \sqrt{2K/3}$, which is used to define the large-eddy turnover time $T_e = u'^2/\varepsilon_I$. The Taylor micro-scale is defined as in Pope (2000), i.e, $\lambda = (15\nu u'^2/\varepsilon_\nu)^{1/2}$. The Taylor micro-scale Reynolds number is computed as $Re_\lambda = u'\lambda/\nu$, and the Kolmogorov length scale is $\eta = (\nu^3/\varepsilon_I)^{1/4}$.

Last, we define the integral length scales along the directions normal and parallel to the axis of rotation. These are constructed from the two-point velocity correlation:

$$R(\mathbf{r}) = \frac{\langle u_i(\mathbf{x}) u_i(\mathbf{x}+\mathbf{r}) \rangle_{\mathcal{L}}}{\langle u_i(\mathbf{x}) u_i(\mathbf{x}) \rangle_{\mathcal{L}}}, \tag{4.5}$$

where $\mathbf{r} = r_i \hat{\mathbf{e}}_i$ is an arbitrary position vector. We integrate Eq. (4.5) with $\mathbf{r} = r\hat{\mathbf{e}}_r$, as in spherical coordinates, or with $\mathbf{r} = r_\perp \hat{\mathbf{e}}_\perp$ and $\mathbf{r} = r_\parallel \hat{\mathbf{e}}_\parallel$, as in cylindrical

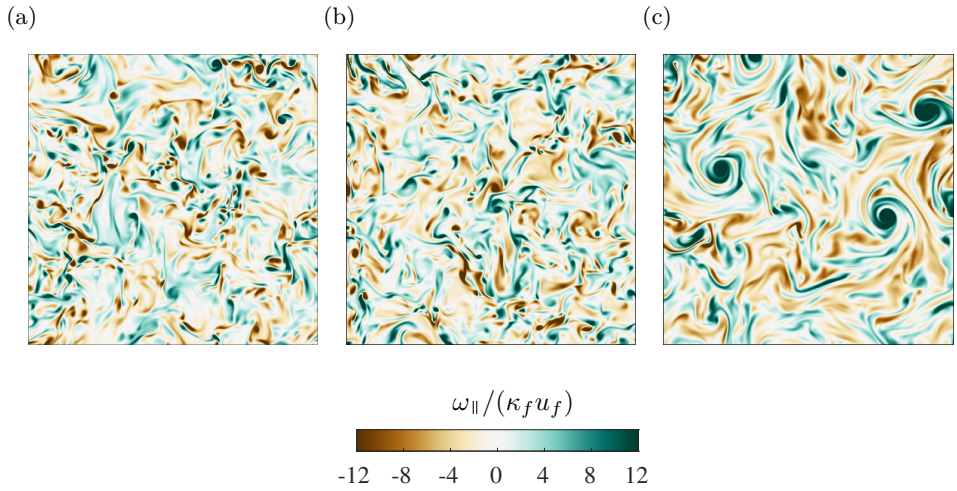

Figure 4.3: Instantaneous contours on a x_1x_2-plane of the vorticity projected along the axis of rotation. (a) isotropic case; (b) $Ro_\varepsilon = 0.22$; (c) $Ro_\varepsilon = 0.06$. All panels correspond to the final simulation time $t \approx 30\,\tau_f$.

coordinates, to obtain the integral length scales along the respective directions:

$$\ell = \int_0^{\pi\mathcal{L}_{min}} R(r)\,\mathrm{d}r, \quad \ell_\perp = \int_0^{\pi\mathcal{L}_\perp} R(r_\perp)\,\mathrm{d}r_\perp, \quad \text{and} \quad \ell_\parallel = \int_0^{\pi\mathcal{L}_\parallel} R(r_\parallel)\,\mathrm{d}r_\parallel. \tag{4.6}$$

In Eq. (4.6), $\mathcal{L}_{min}$ is taken as $\min(\mathcal{L}_\parallel, \mathcal{L}_\perp)$ in the limit of the integral that defines ℓ. To represent quantities from the initial and isotropic flow field we use the superscript "iso", like in $\ell^{\,\mathrm{iso}}$.

Initial Conditions

The initial conditions for the simulations with rotation are produced by injecting energy at constant rate ε_I to a fluid that is initially at rest. The energy, which is injected at wavenumber $\kappa_f = 8$, is progressively distributed over a wider range of wavenumbers by action of the triple velocity correlations. When the energy cascade is built up, the box-averaged kinetic energy K stops growing and a steady-state is reached. The numerical resolution guarantees that at all times $\kappa_{max}\eta \geq 1.5$, which is sufficient to resolve all scales of motion. The initial transient lasts for $20\,\tau_f$ or, equivalently, $8.45\,T_e$, and afterwards, statistics are collected for another $54\,\tau_f$ ($22.84\,T_e$). For the fully-developed field, we find that $Re_\lambda \approx 68$, and that the relation $\ell^{\,\mathrm{iso}} = \ell_\parallel^{\,\mathrm{iso}} = \ell_\perp^{\,\mathrm{iso}}$ holds up to 2 decimal places. The latter suggests that the flow field is in fact isotropic.

Other statistics of the steady-state match closely with typical values found in DNS of homogeneous isotropic turbulence. For instance, the skewness and flatness of the longitudinal velocity derivative $\partial u_1/\partial x_1$ are -0.51 and 4.8, respectively, in agreement with Tang *et al.* (2018) and Van Atta & Antonia (1980). The energy

dissipation rate ε_ν at the steady-state is well approximated by $\varepsilon_\nu = C_\varepsilon^{\text{iso}}(u'^{\text{iso}})^3/\ell^{\text{iso}}$, where $C_\varepsilon^{\text{iso}} \approx 0.35$ is the constant of proportionality. Note, however, that the value of this constant depends on how the two-point correlation in Eq. (4.5) is normalized. If we normalize it with $2u'$, like in Kaneda *et al.* (2003), instead of $2K$, like in Eq. (4.5), a factor of 3/2 must be accounted for to yield $C_\varepsilon^{\text{iso}} \approx 0.5$ in agreement with the literature; see Ishihara *et al.* (2009) for a compilation of other numerical results.

In this study, the goal is not to achieve the highest possible Reynolds number for a given numerical resolution. Instead, we focus on maximizing the time for which large scale eddies with typical size ℓ^{iso} can evolve unbounded, while still resolving all scales of motion. Therefore, apart from forcing at scales smaller than usual, we consider an elongated domain with $A_r = 8$. As a result, the isotropic fields to which background rotation can be imposed to are in the vertical direction about 340 times larger than ℓ^{iso} and, in the normal direction, $2\pi\mathcal{L}_\perp/\ell^{\text{iso}} \approx 40$. In Fig. 4.1, we show evidence of these aspects. Figure 4.1a confirms through the two-point velocity correlation along the normal and the parallel directions that the ratio of domain size to flow structures is indeed significantly larger in the vertical direction. The area below the curves equals $2\pi\mathcal{L}_\perp/\ell_\perp^{\text{iso}}$ and $2\pi\mathcal{L}_\parallel/\ell_\parallel^{\text{iso}}$, respectively. Alongside, Fig. 4.1b verifies that the velocity fields are isotropic, as the curves for the one-dimensional energy spectra along the normal and perpendicular directions overlap.

These features are also clearly visible in the flow field visualization; see Fig. 4.2, where we show a sub-set of the computational domain with the flow structures visualized by the Q-Criterion of Hunt *et al.* (1988) and colored by the normalized projection of the vorticity vector on the axis of rotation, i.e., $\boldsymbol{\omega}\cdot\mathbf{e}_\parallel/\|\boldsymbol{\omega}\|$. Reinforcing the aforementioned results, we observe two main points in the isotropic field that is used as initial condition for the runs with rotation (Fig. 4.2a). First, the flow structures do not display any preferential sense of rotation, which is confirmed by the uniform distribution of the colors. Second, they are also isotropically arranged and therefore not aligned along any preferential direction. For a summary of the numerical and physical parameters of the initial conditions, please refer to Table 4.1.

Runs in a Rotating Frame of Reference

The runs with rotation are constructed by imposing 21 different background rotation rates to the isotropic flow field shown in Fig. 4.2a; see Table 4.2 for the relevant numerical and physical parameters. The result is a set of simulations that covers a broad range of the Ro_ε parameter space, i.e., $0.06 < Ro_\varepsilon < 1.54$. The Zeman wavenumber in terms of the Kolmogorov length scale, $\kappa_\Omega\eta$, for instance, varies from 0.1 for $Ro_\varepsilon = 1.54$ (weakest rotation case) to 1.1 for $Ro_\varepsilon = 0.06$ (strongest rotation case). As the numerical resolution provides $\kappa_{max}\eta = 1.5$ for the fully developed isotropic reference initial field, for $Ro_\varepsilon = 0.06$, almost all scales of motion are influenced by the system's rotation.

With increasing the rotation rate, the flow field gradually departs from the initial isotropic state in agreement with previous experimental and numerical studies (Bartello *et al.*, 1994; van Bokhoven *et al.*, 2009). This is observed from visualizing 4 movies (movie 1: $Ro_\varepsilon = 0.63$; movie 2: $Ro_\varepsilon = 0.22$; movie 3: $Ro_\varepsilon = 0.09$; movie 4:

$Ro_\varepsilon = 0.06$), which show the evolution of the flow field in a sub-set of the computational domain; see our data repository Pestana & Hickel (2019*a*) for the animations, and also 2 movies of the contours of the vorticity vector along the axis of rotation ($\omega_\parallel$), on a normal (movie 5) and a parallel plane (movie 6). Altogether, the visualizations indicate that rotation destroys the small structures and modulates the flow field such that columns elongated in the direction of rotation emerge. These typical features of rotating turbulence are better appreciated in movies 3 and 4, where the pairing and stretching of co-rotating eddies are more salient.

To give an impression of the flow field, we include two snapshots in Figs. 4.2b and 4.2c for the run with $Ro_\varepsilon = 0.06$ (strongest rotation) at times subsequent to the onset of rotation ($t = 10.5\,\tau_f$ and $t = 20\,\tau_f$) and visualizations of $\omega_\parallel$ for different Ro_ε in Figs. 4.3 and 4.4.

4.3. The Growth Rate of Columnar Eddies

Now, we present results and discuss the influence of different rotation rates on the growth of the columnar eddies. For the quantitative analysis, we use integral length scales, which on one hand can be used to quantify the typical eddy size that contributes the most to the total kinetic energy, and on the other hand also serves as an indicator of anisotropy. Due to the background rotation, the dynamics of the flow in the parallel and transversal direction are essentially different, which is reflected in the temporal evolution of $\ell_\parallel$ and $\ell_\perp$ (Bardina *et al.*, 1985). As it will be seen, the appearance of the columnar eddies in Figs. 4.2b and 4.2c is strongly reflected in the growth of the integral length scale along the axis of rotation.

We obtain the time evolution of $\ell_\parallel$ and $\ell_\perp$ by evaluating Eq. (4.6) on a series of instantaneous velocity fields throughout the simulation time, see Fig. 4.5. We choose to split the actual data in two diagrams, which are displayed side-by-side. The left panels correspond to cases for which $Ro_\varepsilon \geq 0.39$ (group R1 in Table 4.2) and the right panels to $Ro_\varepsilon \leq 0.31$ (group R2 in Table 4.2).

For $Ro_\varepsilon \geq 0.39$ (left panels; group R1), $\ell_\parallel$ and $\ell_\perp$ remain approximately unchanged in time and at values similar to the ones at $t = 0$, which corresponds to the initial isotropic field. Specifically for $Ro_\varepsilon = 0.39$, the run with highest rotation rate in this group, the departure from isotropy is marginal and $\ell_\parallel/\ell_\perp \approx 1.5$ at the final simulation time. Differently, for $Ro_\varepsilon \leq 0.31$ (right panels; group R2), the disparity between $\ell_\parallel$ and $\ell_\perp$ is clear. We observe that $\ell_\parallel$ grows substantially in time, whereas variations in $\ell_\perp$ are small when compared to the latter. For instance, for $Ro_\varepsilon = 0.06$, the final value of $\ell_\parallel$ is 26.8 times greater that its initial value, whereas $\ell_\perp$ only increases by a factor of 1.21. Additionally, we observe an intriguing behavior in $\ell_\perp$. It initially grows in time until a maximum is reached; thereupon, it decreases towards a minimum, before growing again. On the other hand, $\ell_\parallel$ increases monotonically and approximately linearly for $t > 10\,\tau_f$.

The growth of $\ell_\parallel$ in Fig. 4.5d is in agreement with the formation of columnar eddies observed in Fig. 4.2c. In order to identify the dependency between the growth rate of $\ell_\parallel$ and Ro_ε, we have fit the data for $\ell_\parallel$ in the interval $10\,\tau_f < t < 30\,\tau_f$ with a straight line. The linear fit approximates fairly well the time evolution of $\ell_\parallel$ and the maximum residuum is found for $Ro_\varepsilon = 0.11$, where the discrepancy is around 4.7% of

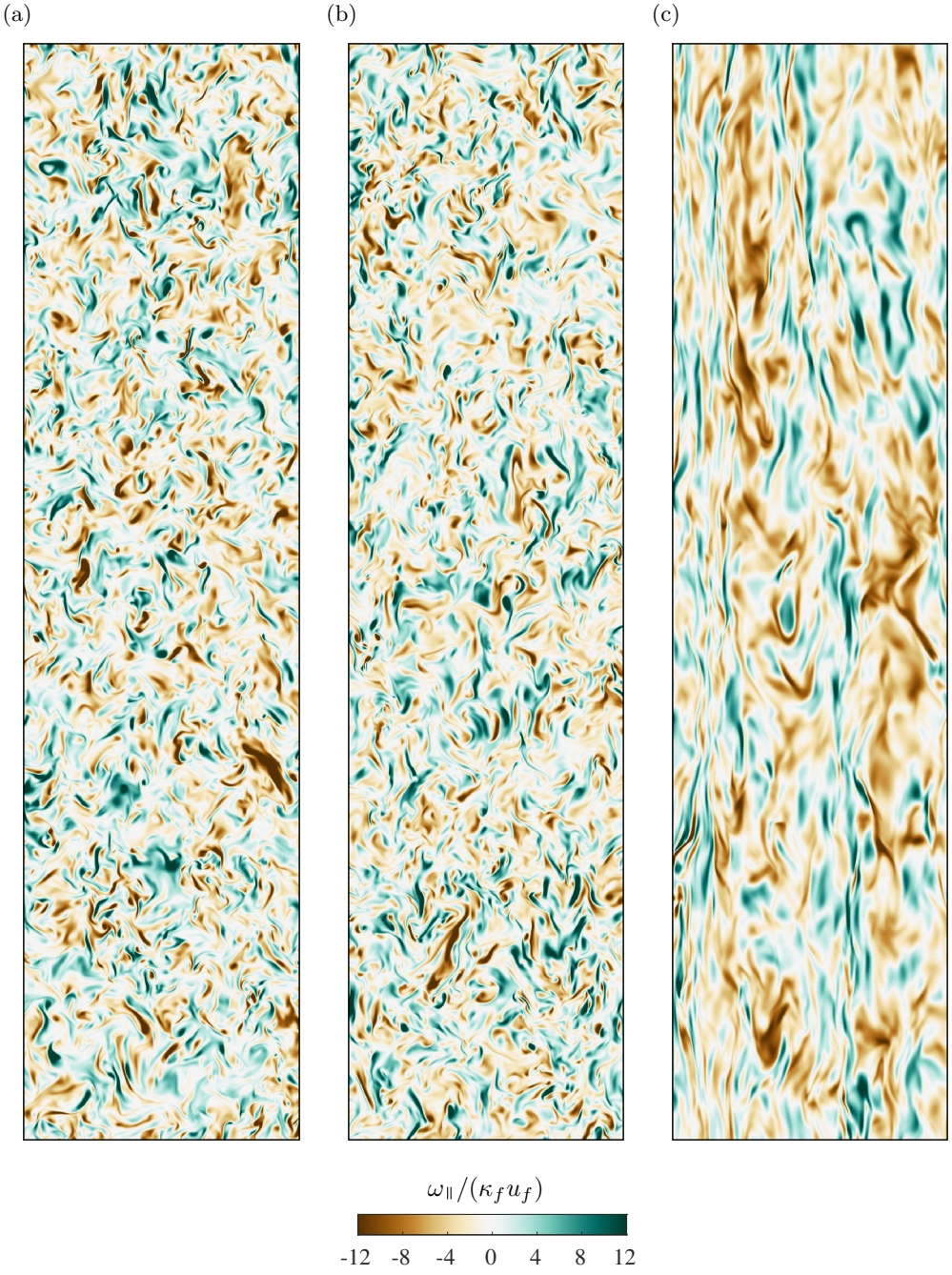

Figure 4.4: Instantaneous contours of the vorticity projected on the axis of rotation on a x_2x_3-plane. (a) isotropic case; (b) $Ro_\varepsilon = 0.22$; (c) $Ro_\varepsilon = 0.06$. All panels correspond to the final simulation time $t \approx 30\,\tau_f$.

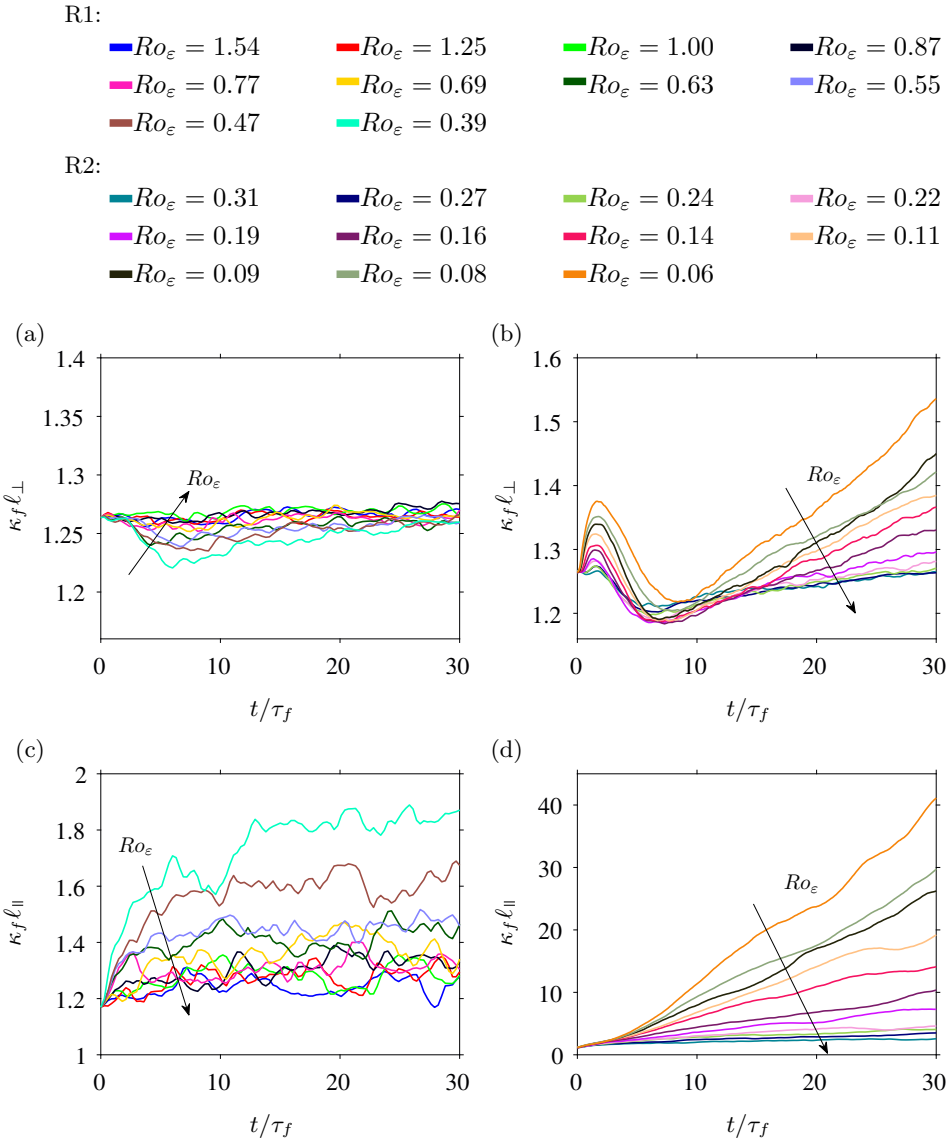

Figure 4.5: Time evolution of the parallel and transversal integral length scales $\ell_\parallel$ and $\ell_\perp$, for group R1 (left panels; $1.54 \geq Ro_\varepsilon \geq 0.39$) and group R2 (right panels; $0.31 \geq Ro_\varepsilon \geq 0.06$).

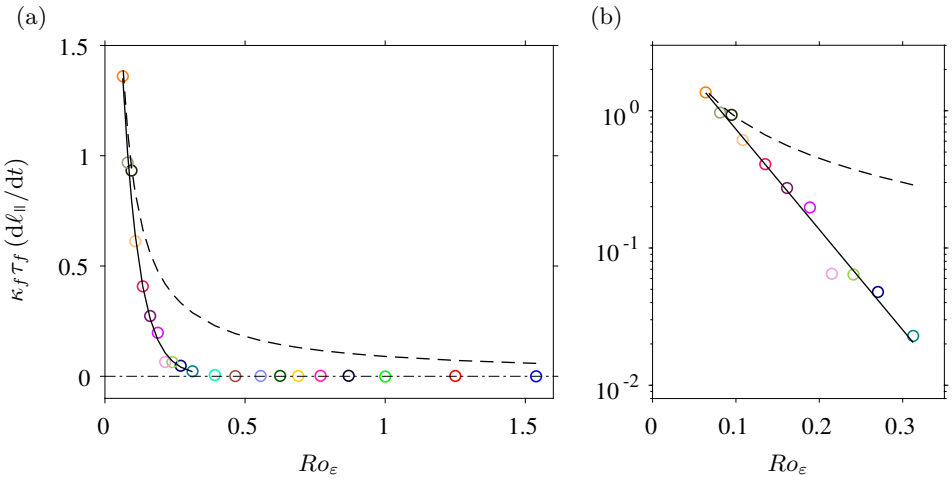

Figure 4.6: Non-dimensional growth rate $\gamma = \kappa_f \tau_f (\mathrm{d}\ell_\parallel/\mathrm{d}t)$ as a function of Ro_ε. Least-square fit (—) for the range $0.06 \leq Ro_\varepsilon \leq 0.31$, which yields the power-law $\gamma = a \exp(b\, Ro_\varepsilon)$ with $a = 3.90$ and $b = -16.72$. The thin dashed line (- - -) represents a law of the type $\gamma \sim Ro_\varepsilon^{-1}$, where the constant of proportionality was arbitrarily chosen to fit the leftmost data point. The dot dashed line (- · -) represents a zero growth-rate.

the mean value of $\ell_\parallel$. The slope of the linear fit non-dimensionalized with the forcing parameters, i.e., $\gamma = \kappa_f \tau_f (\mathrm{d}\ell_\parallel/\mathrm{d}t)$, is shown in Fig. 4.6 as a function of Ro_ε. For $Ro_\varepsilon \geq 0.39$, the effects of rotation are irrelevant and γ is approximately zero within statistical error, suggesting that the integral length scales remain approximately at their initial value. More precisely, the linear regression leads to both positive and negative values of γ in this range. Nevertheless, the values are all very small and at most of the order of $\mathcal{O}(10^{-3})$. On the other hand, the range $0.06 \leq Ro_\varepsilon \leq 0.31$ is marked by a significant rise in γ, and, specifically for this range, a least-square fit yields the power law $\gamma = a \exp(b\, Ro_\varepsilon)$ with $a = 3.90$ and $b = -16.72$ (Fig. 4.6b).

A linear growth rate for $\ell_\parallel$ is in agreement with experimental observations (Jacquin *et al.* (1990); Staplehurst *et al.* (2008)), numerical simulations (Bartello *et al.* (1994); Yoshimatsu *et al.* (2011)) and closure theories such as the EDQNM2 of Cambon & Jacquin (1989). Nevertheless, the growth rate obtained here is essentially different than what has been found in previous studies, which have mostly focused on decaying homogeneous isotropic turbulence. For example, the laboratory experiments of Staplehurst *et al.* (2008) and the DNS of Yoshimatsu *et al.* (2011) found a growth rate proportional to $1/\tau_\Omega = 2\Omega$, which would result in $\gamma \sim Ro_\varepsilon^{-1}$. As we see from Fig. 4.6, our results do not agree with such a scaling, which suggests a faster increase in γ for decreasing Ro_ε. Nevertheless it is important to remark that previous work have analyzed the first initial time instants upon the onset of rotation, while our results include an extended observation time and it is therefore a prediction of the growth rate of columnar eddies at later time instants. For example, the numerical results by Yoshimatsu *et al.* (2011) consider a total simulation time of $10\,\tau_\Omega$ for their strongest rotation case ($Ro_\lambda = 0.90$), whereas our results for a

similar parameter point (`run18`; $Ro_\lambda = 0.80$) contains approximately $270\,\tau_\Omega$. Last, let us remark that the transition Rossby number found here (based on the disparity between $\ell_\parallel$ and $\ell_\perp$) is in close agreement with previous observations: for instance, Moisy *et al.* (2011) report that anisotropy develops in decaying rotating turbulence at a macro and a micro Rossby number of 0.4 and 1.8, respectively. In comparison, results in Fig. 4.6 suggest a transition within the range $0.31 < Ro_\varepsilon < 0.39$, which corresponds to $2.32 < Ro_\lambda < 2.91$.

Note that to prevent the results from being affected by numerical artifacts, we stopped the simulations when $\ell_\parallel$ was about 8 time smaller than $2\pi\mathcal{L}_\parallel$. This constraint limited our runs to a duration of $30\,\tau_f$ ($12.7\,T_e$), and was due to the simulation with $Ro_\varepsilon = 0.06$. Obviously, for the remaining cases, $2\pi\mathcal{L}_\parallel/\ell_\parallel > 8$ at $t = 30\,\tau_f$. The decision of when to interrupt the runs were rather arbitrary, but a value of 8 for the ratio $2\pi\mathcal{L}_\parallel/\ell_\parallel$ is common in DNS of homogeneous isotropic turbulence (Cardesa *et al.*, 2017).

4.4. Scaling Laws for the Energy Dissipation Rate

The analysis for the integral length scales in the previous section has identified two regimes in our dataset. Whereas the group of runs R1 display a dynamics similar to homogeneous isotropic turbulence with no characteristic growth of $\ell_\parallel$, runs in the group R2 are characterized by strong anisotropy and $\gamma > 0$. In this section, we present results for the evolution of the energy dissipation rate, and seek for similarity relations that can collapse the data in the different regimes.

After the onset of rotation, both K and ε_ν evolve in time according to the conservation of energy, i.e., $\mathrm{d}K/\mathrm{d}t = -\varepsilon_\nu + \varepsilon_I$. While K grows rapidly (Fig. 4.7a), the viscous dissipation ε_ν first decreases monotonically until a minimum Fig. 4.7b. The minimum value decreases with Ro_ε, and for the runs of group R2 it scales with $Ro_\varepsilon^{0.36}$ (not shown). After reaching its lowest value, ε_ν continues to grow towards the power input ε_I, although the inequality $\varepsilon_\nu < \varepsilon_I$ remains for some of the cases up to the final simulation time. Generally speaking, the mismatch between the energy dissipation rate and the energy input rate in Fig. 4.7b is stronger for small Ro_ε (group R2). For the runs in this group, we also observe that the parallel direction contributes significantly to ε_ν (Fig. 4.7c). By splitting the energy dissipation rate into its normal and parallel contributions such that $\varepsilon_\nu = 2\varepsilon_{\nu,\perp} + \varepsilon_{\nu,\parallel}$, where $\varepsilon_{\nu,\perp} = (\varepsilon_{\nu,11} + \varepsilon_{\nu,22})/2$ and $\varepsilon_{\nu,\parallel} = \varepsilon_{\nu,33}$, we find that for decreasing Ro_ε the contribution due to the parallel direction increases, whereas for large Ro_ε the energy dissipation rate is equally partitioned among both directions. For instance, for $Ro_\varepsilon = 1.54$ the ratio $\varepsilon_{\nu,\perp}/\varepsilon_{\nu,\parallel}$ is close to 1, while for $Ro_\varepsilon = 0.06$ almost half of the total dissipation stems from $\varepsilon_{\nu,\parallel}$. In Fig. 4.7c, we also note that $\varepsilon_{\nu,\perp}/\varepsilon_{\nu,\parallel}$ remains approximately unchanged in time for $t > 15\,\tau_f$. Averaging $\varepsilon_{\nu,\perp}/\varepsilon_{\nu,\parallel}$ (Fig. 4.7d) in the interval $15\,\tau_f < t < 30\,\tau_f$ shows that $\varepsilon_{\nu,\perp}/\varepsilon_{\nu,\parallel}$ scales with $Ro_\varepsilon^{0.37}$ for $0.31 < Ro_\varepsilon < 0.14$, while for smaller Ro_ε the ratio between normal and parallel dissipation rates seems to reach an asymptotic limit of 0.54 for $Ro_\varepsilon < 0.9$. The latter finding however needs to be confirmed by studies at even lower Ro_ε.

The imbalance $\varepsilon_\nu \neq \varepsilon_I$ is the footprint of an inverse energy cascade that is triggered by the Coriolis force, and that leads to the accumulation of energy at the

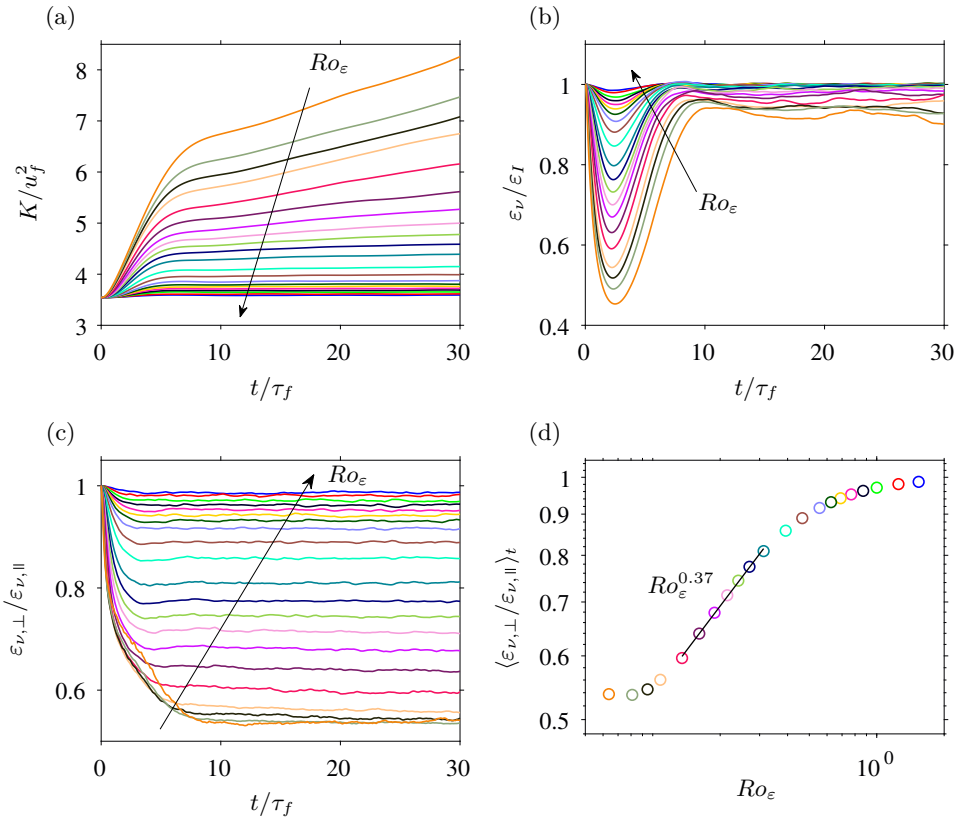

Figure 4.7: Time evolution of (a) box averaged kinetic energy K and (b) energy dissipation rate ε_ν. Panel (c) shows the ratio between the normal ($\varepsilon_{\nu,\perp}$) and parallel ($\varepsilon_{\nu,\parallel}$) energy dissipation rate, whereas panel (d) shows the data from (c) averaged in the interval $15\,\tau_f < t < 30\,\tau_f$ and in terms of Ro_ε.

large scales. This is expected to occur when Ro_ε is below a critical Rossby number that depends on the geometrical dimensions of the system (Deusebio *et al.*, 2014; Pestana & Hickel, 2019*b*; Smith *et al.*, 1996). In such cases, however, equilibrium ($\varepsilon_\nu = \varepsilon_I$) can still be restored after long integration times when the energy in the wavenumbers $\kappa < \kappa_f$ is sufficiently high to contribute to ε_ν (Seshasayanan & Alexakis, 2018; Valente & Dallas, 2017). For the runs considered in this study, the critical Ro_ε is approximately 1 as show in Pestana & Hickel (2019*b*).

From Fig. 4.7b, it is evident that a naive scaling in terms of the forcing parameters can not cause the different lines in Fig. 4.7b to collapse, as it would in homogeneous isotropic turbulence. In other words, an approximation of ε_ν in terms of u_f and κ_f is invalid because the evolution of ε_ν in Fig. 4.7b depends clearly on Ro_ε. In homogeneous isotropic turbulence, the estimation $\varepsilon_\nu \sim u_f^3 \kappa_f$ suffices since both u_f and $1/\kappa_f$ are proportional to a characteristic velocity and a characteristic length, and this expression is equivalent to $\varepsilon_\nu \sim (u'^{\,\mathrm{iso}})^3/\ell^{\,\mathrm{iso}}$. We must therefore

search for other ways to approximate ε_ν in rotating turbulence.

4.4.1. Spectral Transfer Time

To address this problem we followed the methodology introduced by Kraichnan (1965) within the context of MHD and bridged by Zhou (1995) to homogeneous rotating flows. The basic idea is that the rate at which energy is transferred to the smaller scales depends on an energy content and on a time scale, viz. the spectral transfer time. If we treat the characteristic scales as global quantities instead of wavenumber dependent, the dissipation law can be written in terms of the r.m.s. velocity and the spectral transfer time as

$$\varepsilon_\nu \sim \frac{u'^2}{\tau_s}. \tag{4.7}$$

The spectral transfer time, however, is composed of two additional time scales, namely the nonlinear time scale τ_{nl} and the relaxation time scale τ_3. Whereas τ_{nl} indicates how fast the triple velocity correlations are built up and favors the forward energy cascade, τ_3 serves as a relaxation time or a measure of how fast the triple velocity correlations are destroyed. The assumptions that the energy dissipation rate ε_ν is directly proportional to τ_3 and that the energy cascade is local lead to the so-called "golden rule" (Zhou, 1995):

$$\tau_s \sim \frac{\tau_{nl}^2}{\tau_3}. \tag{4.8}$$

In Eq. (4.8), τ_{nl} involves a velocity and a length scale and τ_3 can rest on any other time scales that are relevant for the problem. For instance, in forced homogeneous isotropic flows, $\tau_3 \sim \tau_f \sim \tau_{nl} \sim \ell^{\,\mathrm{iso}}/u'^{\,\mathrm{iso}}$, which implies $\tau_s \sim \ell^{\,\mathrm{iso}}/u'^{\,\mathrm{iso}}$ to recover the well known dissipation law $\varepsilon_\nu \sim (u'^{\,\mathrm{iso}})^3/\ell^{\,\mathrm{iso}}$, extensively verified by DNS and experiments. For more complex flows, which involve other time scales like rotating turbulence with the rotation time scale $\tau_\Omega = 1/(2\Omega)$, the relaxation time scale τ_3 can be assumed as function of the type $\tau_3 = \tau_3(\tau_f, \tau_\Omega)$ (Kraichnan, 1965; Matthaeus & Zhou, 1989; Zhou, 1995). Combining Eqs. (4.7) and (4.8) leads to

$$\varepsilon_\nu \sim u'^2 \left(\frac{\tau_3}{\tau_{nl}^2}\right), \tag{4.9}$$

and the problem of determining the dissipation law becomes the one of determining τ_{nl} and τ_3.

4.4.2. Evaluation of Current Available Dissipation Laws

In current literature, a few dissipation laws for homogeneous rotating turbulence have been proposed. For example, the approximations that follow from the theory of Galtier (2003); Nazarenko & Schekochihin (2011); Zhou (1995) and Baqui & Davidson (2015) are

$$\varepsilon_\nu \sim \frac{u'^4}{\Omega\ell^2}, \quad \varepsilon_\nu \sim \frac{u'^4\ell_\parallel}{\Omega\ell_\perp^3}, \quad \varepsilon_\nu \sim \frac{u'^3}{\ell_\perp}, \quad \text{and} \quad \varepsilon_\nu \sim \frac{u'^3}{\ell_\parallel}, \tag{4.10}$$

respectively. Although these authors do not explicitly present their theories within the framework of a spectral transfer time, we have taken the freedom to also summarize their theories within this context.

The law proposed by Zhou (1995), for instance, ignores anisotropy. It assumes that $\tau_{nl} \sim \ell/u'$ and that the relaxation time scale is proportional to the rotation time scale, i.e., $\tau_3 \sim \tau_\Omega$, to yield $\varepsilon_\nu \sim u'^4/(\Omega\ell^2)$. In contrast, dimensional analysis for the weak inertial-wave theory proposed by Galtier (2003), which takes into account scale anisotropy, results in $\varepsilon_\nu \sim u'^4\ell_\parallel/(\Omega\ell_\perp^3)$, where $\tau_{nl} \sim \ell_\perp/u'$ and $\tau_3 \sim \ell_\parallel/(\Omega\ell_\perp)$. When anisotropy is however disregarded, i.e., $\ell \sim \ell_\parallel \sim \ell_\perp$, the predictions by Galtier (2003) reduce to the relation proposed by Zhou (1995). The critical balance theory of Nazarenko & Schekochihin (2011) considers that $\tau_{nl} \sim \tau_3 \sim \ell_\perp/u'$ and the theory of Baqui & Davidson (2015) suggests that $\tau_{nl} \sim \tau_3 \sim \ell_\parallel/u'$.

When we apply the scaling laws in Eq. (4.10) to the data presented in Fig. 4.7b, we find a good match for the runs in group R1. In Figs. 4.8 and 4.9, we scale ε_ν with the different laws; Fig. 4.9 shows the inverse of what appears in Fig. 4.8. We present the results in this manner in order to provide a fair treatment and avoid misinterpretations from arbitrary choice of the axis limits, which can increase/decrease the spread between the lines.

By comparing Figs. 4.8a and 4.9a, we see that the approximation suggested by Zhou (1995) can not collapse the data. Whereas the data for the group R2 appears close to straight lines in Fig. 4.9a, Fig. 4.8a shows that they diverge and instead increase in time. For large Ro_ε, however, both figures show straight lines, suggesting a correction factor in terms of Ro_ε. For the weak inertial-wave theory, Fig. 4.8b shows that the curves of the 5 last runs in group R2 (lowest Ro_ε) seems to follow a similar trend. This behavior is however not observed in Fig. 4.9b, which shows that these lines actually increase in time with approximately the same slope. For the runs in group R1, Fig. 4.9b shows a reasonable collapse of the data, which is however opposed by Fig. 4.8b. The predictions by Nazarenko & Schekochihin (2011) in Figs. 4.8c and 4.9c show that for large Ro_ε, the curves are flat and tend closer to each other. This is expected as $\ell_\perp$ must tend to $\ell^{\,\mathrm{iso}}$ for large Ro_ε, and in this limit the dissipation law of homogeneous isotropic turbulence is recovered. For small Ro_ε, this scaling delivers approximately straight lines in both diagrams, which suggests that a correction in terms of Ro_ε might also be possible.

The best approximation, at least for part of the data-set (group R1), is obtained with the scaling law of Baqui & Davidson (2015). Figure 4.8d and Fig. 4.9d indicates that this scaling is suitable for the runs in group R1 (indicated with an arrow in the figure). For the other runs (group R2), Fig. 4.8d and Fig. 4.9d also provides unsatisfactory results. We are then motivated to look into a similarity law for this group of runs.

4.4.3. A Dissipation Scaling Law for Runs in Group R2

To find a dissipation law for runs in group R2 we base ourselves on Eq. (4.9). The first question we turn to is the one of finding an approximation for τ_{nl}. The nonlinear time scale involves an estimation of a velocity and a length scale, which we shall assume as u' and $\ell_\perp$, respectively. The reason behind this choice is as follows.

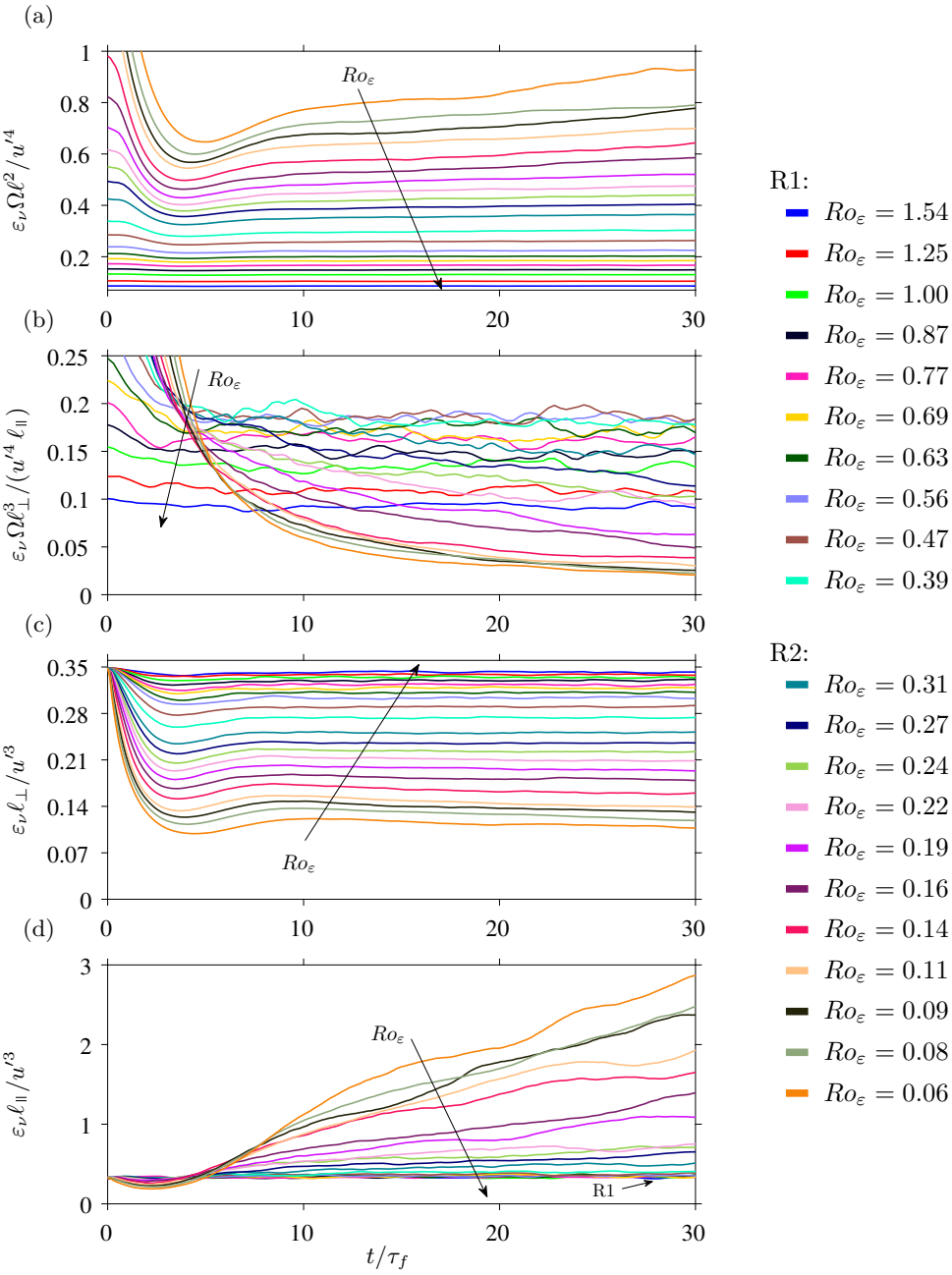

Figure 4.8: Compensated time evolution of the energy dissipation rate for $0.06 < Ro_\varepsilon < 1.54$. Different panels correspond to the different scaling laws found in the literature: (a) Zhou (1995); (b) Weak inertial-wave theory (Galtier, 2003); (c) Critical balance theory (Nazarenko & Schekochihin, 2011); (d) Baqui & Davidson (2015).

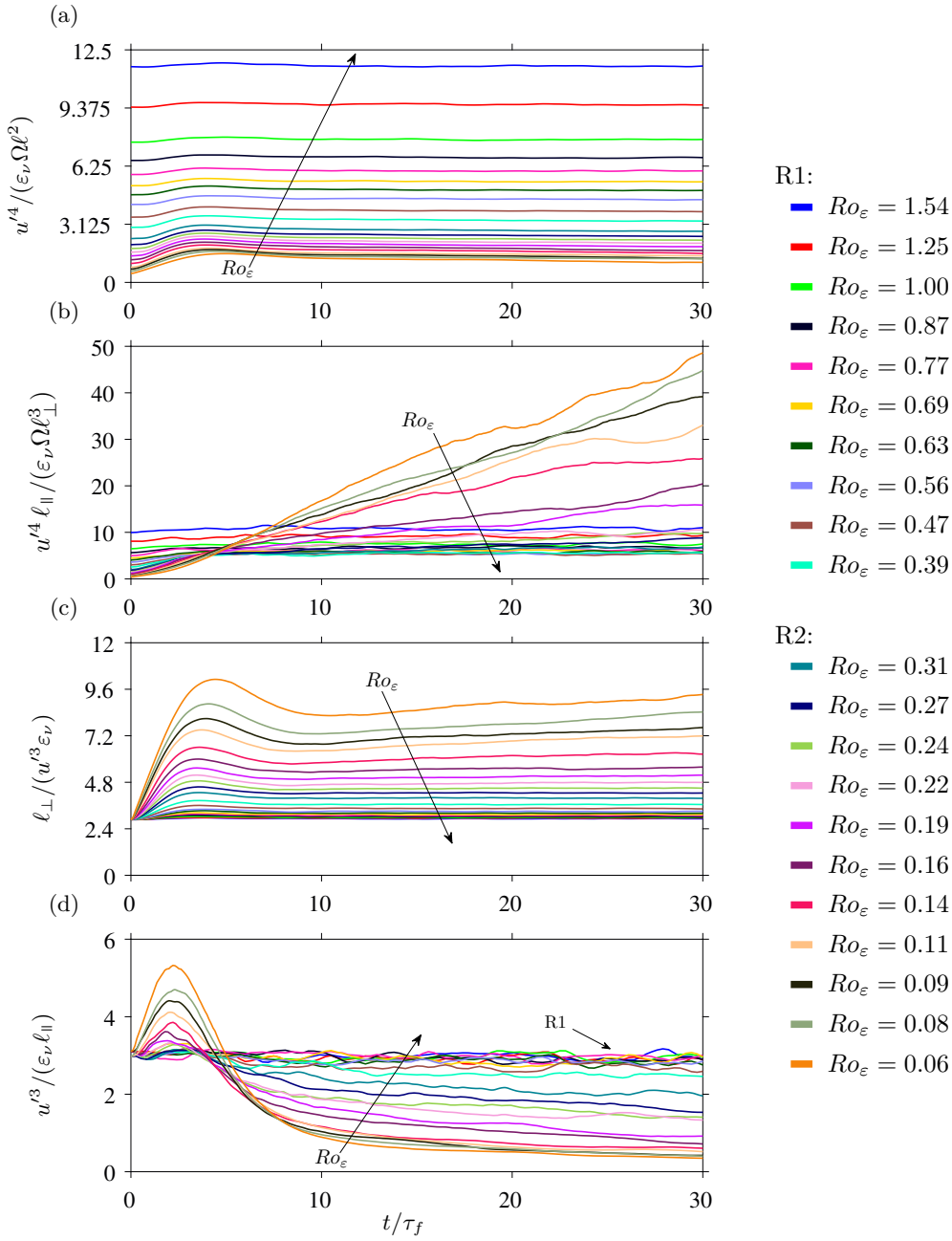

Figure 4.9: Compensated time evolution of the energy dissipation rate as in Fig. 4.8, but plotted as the inverse. Different panels correspond to the different scaling laws found in the literature: (a) Zhou (1995); (b) Weak inertial-wave theory (Galtier, 2003); (c) Critical balance theory (Nazarenko & Schekochihin, 2011); (d) Baqui & Davidson (2015).

From Figs. 4.5d and 4.7b, we observe that $\ell_\perp$ and ε_ν display similar dynamics, although inverted; the evolution of each variable is the opposite of the other. This behavior hints to a dependency of the form $\varepsilon_\nu \sim 1/\ell_\perp$, which can also be justified like in the critical balance theory (Nazarenko & Schekochihin, 2011). Within this theory, the basic idea is that rotation tends to destroy derivatives along the direction of rotation and the advection term is mainly due to the normal velocity gradients and the normal velocity field. Thus, $\ell_\perp$ is taken as the relevant length scale for the nonliner interactions. On the other hand, for the velocity scale, an alternative would be to take information about the transversal velocity fields only as in Baqui & Davidson (2015). Nevertheless, although rotation favors two dimensionalization, the velocity field remains three component and the anisotropy in the Reynolds stress tensor is minimal Yeung & Zhou (1998). For the above reasons, we assume $\tau_{nl} \sim \ell_\perp/u'$, and Eq. (4.9) can be in a preliminary step expressed as

$$\varepsilon_\nu \sim \frac{u'^4}{\ell_\perp^2}\tau_3(\tau_f, \tau_\Omega). \tag{4.11}$$

Now, to determine the relaxation time scale, we rearrange Eq. (4.11) so that τ_3 appears as a function of the other terms and examine its temporal evolution. Figure 4.10a shows $\tau_3 \sim \varepsilon_\nu \ell_\perp^2/u'^4$ over time for all runs. After a transient of approximately $10\,\tau_f$, we observe that the curves for different Ro_ε reach a plateau, with a terminal value that depends on Ro_ε. To determine this dependency, results from Fig. 4.10a are then averaged in the interval $10\,\tau_f < t < 30\,\tau_f$ and the mean value is shown against the corresponding Rossby number in Fig. 4.10b. In the latter figure, the ordinates appear normalized by the nonlinear time scale τ_{nl}^{iso} times $C_\varepsilon^{\text{iso}}$, which is the constant of proportionality of the dissipation law in homogeneous isotropic turbulence. For runs in group R1, $\tau_3/(\tau_{nl}^{\text{iso}}\, C_\varepsilon^{\text{iso}})$ increases with Ro_ε and asymptotically approaches 1, implying that for these Ro_ε the effects of rotation are negligible and the scaling law of homogeneous isotropic turbulence is recovered. Contrarily and more surprising, we see that $\tau_3/(\tau_{nl}^{\text{iso}}\, C_\varepsilon^{\text{iso}})$ follow the power-law Ro_ε^h with $h = 0.62$ for the runs in group R2. Consequently, for this group, we can finally express Eq. (4.11) as

$$\varepsilon_\nu \sim \frac{u'^4}{\ell_\perp^2}(\tau_{nl}^{\text{iso}} Ro_\varepsilon^{0.62}) \sim \frac{u'^3}{\ell_\perp}\left[\left(\frac{\tau_{nl}^{\text{iso}}}{\tau_{nl}}\right) Ro_\varepsilon^{0.62}\right]. \tag{4.12}$$

Equation (4.12) summarizes the effects of rotation for the runs with $0.06 < Ro_\varepsilon < 0.31$, and suggests that in a rotating frame of reference, the disparity between τ_{nl} and τ_{nl}^{iso} increases, such that the ratio $(\tau_{nl}/\tau_{nl}^{\text{iso}})$ shrinks with the inverse of $Ro_\varepsilon^{0.62}$. In other words, Eq. (4.12) implies that the relaxation time scale is $\tau_3 \sim \tau_{nl}^{\text{iso}} Ro_\varepsilon^{0.62}$. Finally, scaling the data in Fig. 4.7b with Eq. (4.12) leads to Fig. 4.11a, where very good agreement is found for all the cases in group R2.

4.4.4. Energy Spectra

With a dissipation law at hand, phenomenological arguments can be further employed to obtain predictions for the scaling exponents of the different energy spectra.

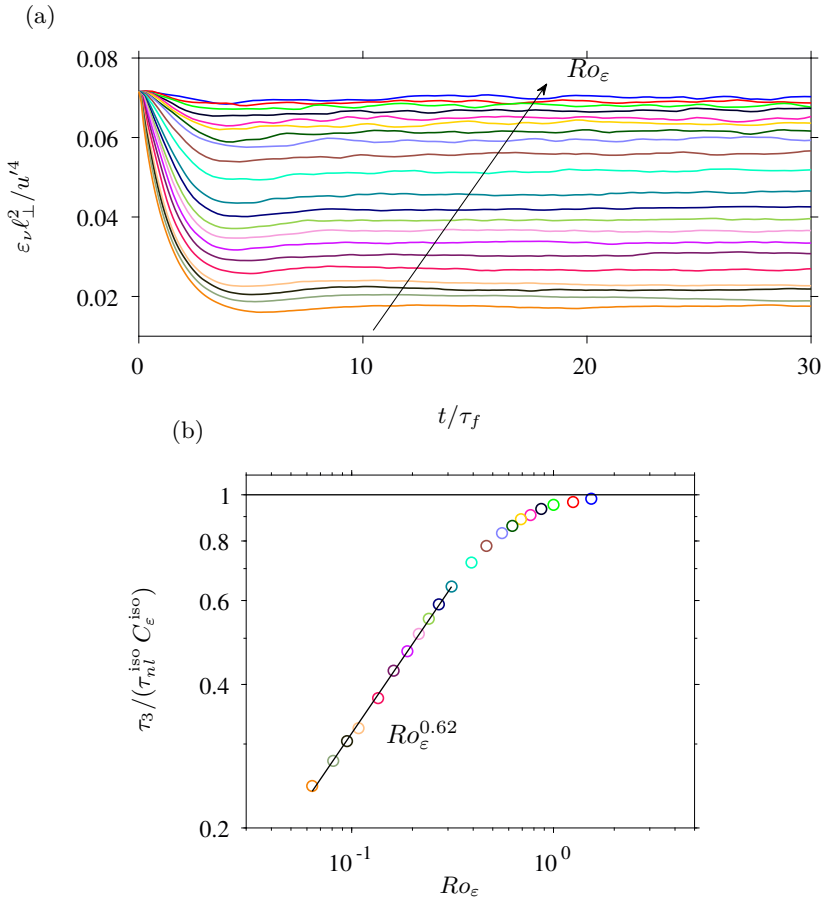

Figure 4.10: Decorrelation (relaxation) time scale τ_3 as function of time (a) and averaged over the interval $10 \leq t \leq 30\,\tau_f$ and normalized by the non-linear time scale τ_{nl} times the proportionality constant $C_\varepsilon^{\rm iso}$(b). Two reference lines are included. The horizontal line at the top signalizes that for large Ro_ε, the relaxation time scale tends to the value of the non-linear time scale of the homogeneous isotropic case. The other line shows the power-law dependency of the type Ro_ε^h with $h = 0.62$ for runs of the group R2.

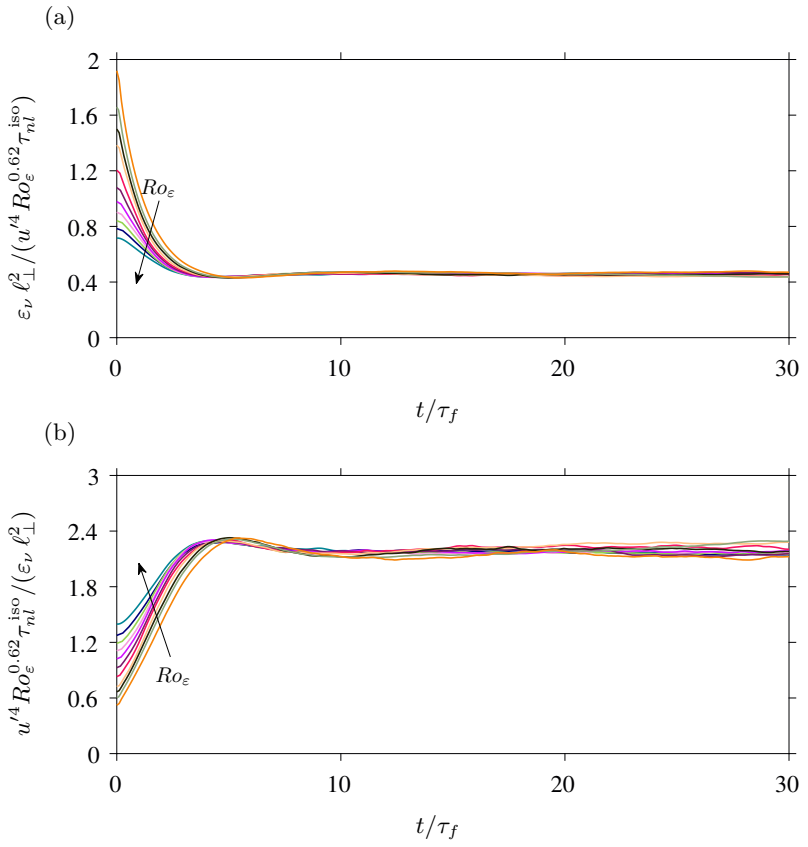

Figure 4.11: Time evolution of the energy dissipation rate scaled according to Eq. (4.12) for $Ro_\varepsilon \leq 0$.

In fact, the different theories presented in Eq. (4.10) are associated with predictions for the kinetic energy spectra. Strictly speaking, the validation of scaling laws for the energy spectra requires data with a well defined inertial range, in which the spectral energy flux is constant and equals ε_ν for a wide range of wavenumbers. In our runs, the latter does not apply due to the relatively low Re_λ, see Fig. 4.12.

If we assume that the energy cascade is local, dimensional analysis leads to (Zhou, 1995)

$$\varepsilon_\nu \sim \left(\frac{\tau_3}{\tau_{nl}^2}\right) \kappa_\parallel \kappa_\perp E(\kappa_\perp, \kappa_\parallel). \tag{4.13}$$

In the equation above, the energy content of a scale of typical size $\ell \sim 1/\kappa$ was assumed to be of the order of $\kappa_\parallel \kappa_\perp E(\kappa_\perp, \kappa_\parallel)$, where $E(\kappa_\perp, \kappa_\parallel)$ is the energy spectra and $\kappa_\perp$ and $\kappa_\parallel$ are the wavenumbers in the normal and longitudinal directions, respectively. Using Eq. (4.12) in Eq. (4.13), we obtain that $E(\kappa_\perp, \kappa_\parallel) \sim B\kappa_\perp^{-2}\kappa_\parallel^{-1}$, with $B = (\varepsilon_\nu Ro_\varepsilon^{-0.62}/\tau_{nl}^{\mathrm{iso}})^{1/2}$, whereas the weak inertial-wave theory of Galtier

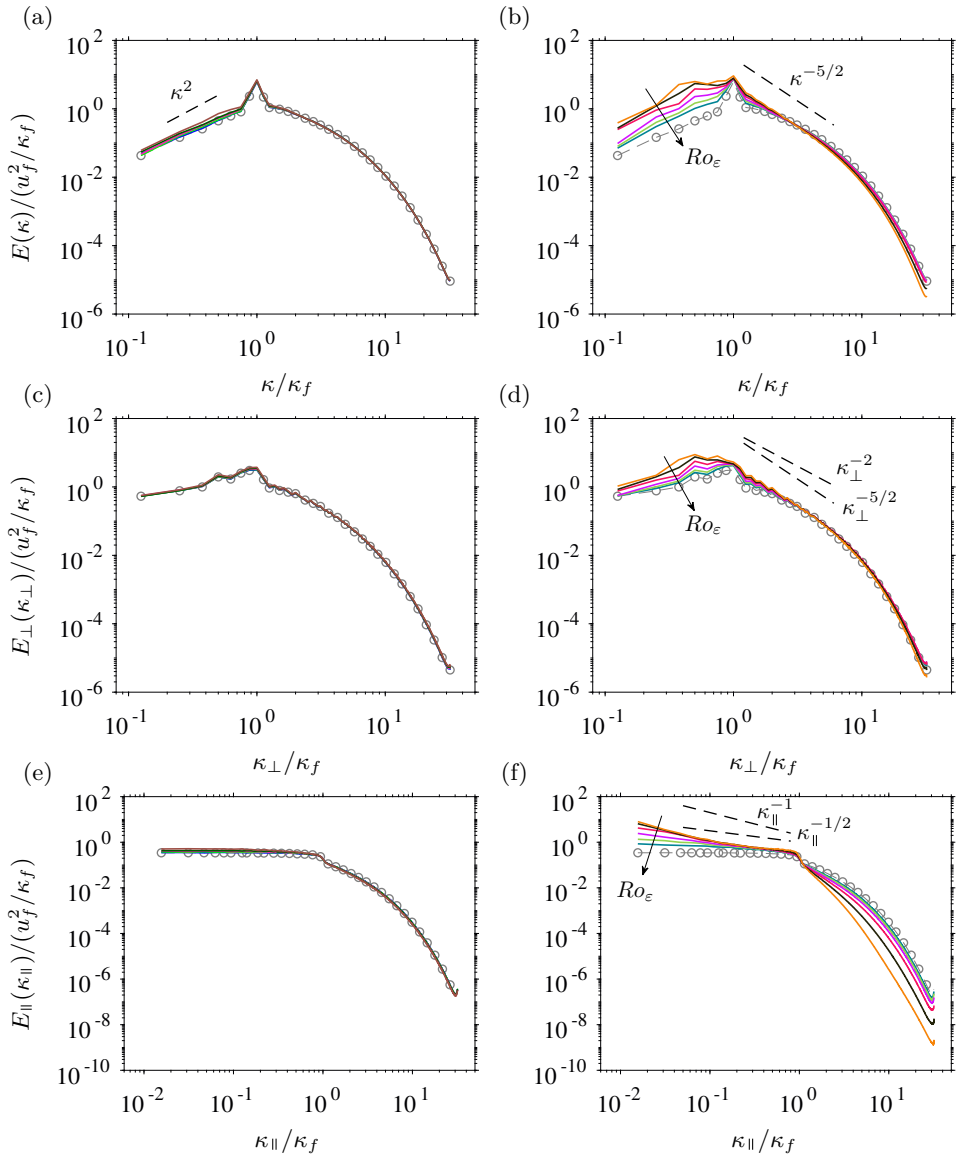

Figure 4.12: Energy spectra at the last instant of time, i.e., $t = 30\,\tau_f$, for every other case in Table 4.2. Left panels show cases of group R1, whereas right panels show cases of group R2. (a-b) Spherical energy spectra; (c-d) normal energy spectra; (e-f) longitudinal energy spectra. The gray dashed lined represents the initial isotropic state (- ⊖ -). Colormap is as in Table 4.2.

(2003) predicts that $E(\kappa_\perp, \kappa_\parallel) \sim \kappa_\parallel^{-1/2} \kappa_\perp^{-5/2}$.

A least-square fit for the case with $Ro_\varepsilon = 0.31$ indicates that $E(\kappa_\perp)$ varies with $\kappa_\perp^{-2.54}$ in the range $1.2 < \kappa_\perp/\kappa_f < 6$ (Fig. 4.12d), and that $E(\kappa_\parallel)$ varies with $\kappa_\parallel^{-0.48}$ in the range $0.05 < \kappa_\parallel/\kappa_f < 0.8$ (Fig. 4.12f). The exponents, however, increase with Ro_ε: for $Ro_\varepsilon = 0.3$ (largest Ro_ε displayed on the right panels of Fig. 4.12), we find that in the same range $E(\kappa_\perp)$ varies with $\kappa_\perp^{-2.17}$ and that $E(\kappa_\parallel)$ changes with $\kappa_\parallel^{-0.34}$. For the runs of group R1 we do not observe any significant changes with respect to the initial isotropic energy spectrum. Differently from the runs in R2, where there is a substantial accumulation of energy for $\kappa < \kappa_f$ (see e.g., Fig. 4.12b), the energy spectra for runs in group R1 are marginally altered with respect to the isotropic initial conditions (see left panels in Fig. 4.12). There is also no wavenumber range with a distinctive scaling, apart from the range $\kappa < \kappa_f$ which scales approximately with κ^2, as in the initial isotropic conditions (Dallas *et al.*, 2015).

5

Inertia-Gravity Waves Breaking in the Middle Atmosphere

Pestana, T., Thalhammer, M., & Hickel, S. 2020 Inertia-Gravity Waves Breaking in the Middle Atmosphere at High-Altitudes: Energy Transfer and Dissipation Tensor Anisotropy. *Journal of the Atmospheric Sciences* **(in press)**

5.1. Background

The inherent multiscale nature of atmospheric phenomena makes accurate numerical weather predictions a challenging task. At least for the near feature, solving the complete set of governing equations is out of reach (Bauer *et al.*, 2015). Parametrization techniques, either based on a simplified physical description of the atmospheric processes or based on statistics (e.g., stochastic parametrization (Berner *et al.*, 2017)) will therefore continue to gain attention. Nevertheless, steady progress in this area requires unveiling the processes driving small-scale atmospheric phenomena. In this regard, Direct Numerical Simulations (DNS) of simplified scenarios can help us understand at least part of the problem.

Among the myriad of processes that take place in the atmosphere, gravity waves have been recognized as an important player for the middle and upper atmosphere. One interesting aspect is that due to instabilities they can break and induce turbulence and dissipation in the overall large-scale flow (gravity wave drag). Furthermore, gravity waves transport energy and momentum from where they are created to regions far away. Typical wavelengths of gravity waves are usually unresolved by the numerical grid, which implies that their effects have to be included in simulations through parametrization. For example, the deposition of momentum and heat dissipation in the large-scale flow are usually based on linear wave theory models, such as those originally introduced by Lindzen (1981), or based on nonlinear wave interactions, as in the Doppler-spread parametrization of Hines (1997).

Several studies have focused on gravity waves giving special attention to the growth of instabilities and the breakdown process. The studies of Andreassen *et al.* (1994); Fritts *et al.* (1994); Isler *et al.* (1994), for instance, were among the first to recognize the full three-dimensional character of the breakdown process and to investigate the structure of the eddy motion, as well as its influence on the transport of momentum and heat. More recently, the focus has been shifted towards expanding the parameter space, while fully resolving the smallest turbulent scales. The DNS by Fritts *et al.* (2009*a*,*b*) considered two gravity waves above and below the threshold for static instability and at Reynolds number of the order of $\mathcal{O}(10^4)$ (based on the wavelength and the buoyancy period); and Fritts & Wang (2013); Fritts *et al.* (2013) analyzed the breakdown of a monochromatic wave due to interaction with vertically-varying fine structure.

Whereas most studies like the ones cited above have focused on high-frequency inertia-gravity waves (HGWs) for which the effects of the Coriolis force can be neglected, little attention has been paid to low-frequency inertia-gravity waves (IGWs). In fact, it can be argued that HGWs are more relevant, since the background frequency due to stratification supersedes the Coriolis parameter in the atmosphere. Nevertheless, the dynamics of gravity waves depend on their frequency, the effects of which must be studied separately (Achatz, 2005, 2007*a*,*b*).

Regarding the breakdown of IGWs, to the best of our knowledge the work of Remmler *et al.* (2013) was the first to present resolved three-dimensional simulations. In that work, the authors considered a statically unstable monochromatic wave superimposed with its primary and secondary perturbations derived from the linear theory studies of Achatz (2007*b*) and Fruman & Achatz (2012). The DNS by

Remmler *et al.* (2013, 2015) showed that the breakdown process constitutes of a sequence of turbulent bursts, accompanied by a rapid reduction of the wave amplitude. Additionally, their analyses indicate that the duration of the breaking events in 3D simulations are shorter than those in typical investigations, which assume a three-component velocity field with a two-dimensional spatial dependency (also known as 2.5D simulations), and that the energy dissipation rate is less homogeneous than for HGWs.

In the present contribution, we build on the work of Remmler *et al.* (2013) and turn attention to the breaking mechanism of IGWs at higher Reynolds numbers. Our aim is to provide high-fidelity simulation data, which, on one hand highlights some of the underlying features of the energy conversion during the breakdown process, and, on the other hand, serves as reference data for models that do not resolve inertia-gravity waves and wave-generated turbulence and instead account for their effects through parametrization. Using the same setup as in Fruman *et al.* (2014) and Remmler *et al.* (2013), we perform DNS at two distinct Reynolds numbers. We start off with flow field visualizations describing the breaking events. Second, we investigate the temporal evolution of the kinetic energy and the available potential energy and of their associated energy dissipation rate, as well as the vertical energy spectra. Last, we turn our focus to the energy transfer process. We analyze it from the aspect of the relevance of each term in the energy budget equation, as well as from the view of energy transfers between the mean and the fluctuating field.

5.2. Methodology

5.2.1. Governing Equations

We consider fluid motion in the Earth's atmosphere governed by the Boussinesq equations on the f-plane:

$$\begin{aligned} \nabla \cdot \mathbf{u} &= 0 \\ \frac{\partial \mathbf{u}}{\partial t} + \mathbf{u} \cdot \nabla \mathbf{u} &= -\nabla p + b\mathbf{n} - f_c \mathbf{n} \times \mathbf{u} + \nu \nabla^2 \mathbf{u} \\ \frac{\partial b}{\partial t} + \mathbf{u} \cdot \nabla b &= -\mathbf{u} \cdot N^2 \mathbf{n} + \alpha \nabla^2 b. \end{aligned} \tag{5.1}$$

Here, $\mathbf{u} = [u, v, w]$ is the velocity field, t denotes time, p is the pressure field, and b is the buoyancy field, which is defined as normalized deviations of the potential temperature T from the vertically averaged temperature $T^*(z)$. That is, $b = g(T - T^*)/T_0$, where T_0 and g are the reference temperature and the magnitude of the gravity field, respectively. Further, the properties of the fluid are the kinematic viscosity ν and the thermal diffusivity α, and $f_c = 2\Omega_E \sin\beta$ is the Coriolis parameter with Ω_E the Earth's angular velocity and β the latitude on the f-plane. The Brunt-Väisälä frequency is $N^2 = (g/T_0)\mathrm{d}T^*/\mathrm{d}z$ and $\mathbf{n}$ is the negative gravity unit vector. The coordinate system for a fixed observer on Earth is $[x', y', z']$.

For vanishing viscosity and thermal diffusivity, Eq. (5.1) admits wave like solutions of the form $\Re\{[\hat{u}, \hat{v}, \hat{w}, \hat{b}] \exp(I\phi)\}$, where $\Re$ denotes the real part, $\hat{u}$, $\hat{v}$, $\hat{w}$ and $\hat{b}$ are complex amplitudes of the velocity and buoyancy field, ϕ is the phase (Achatz

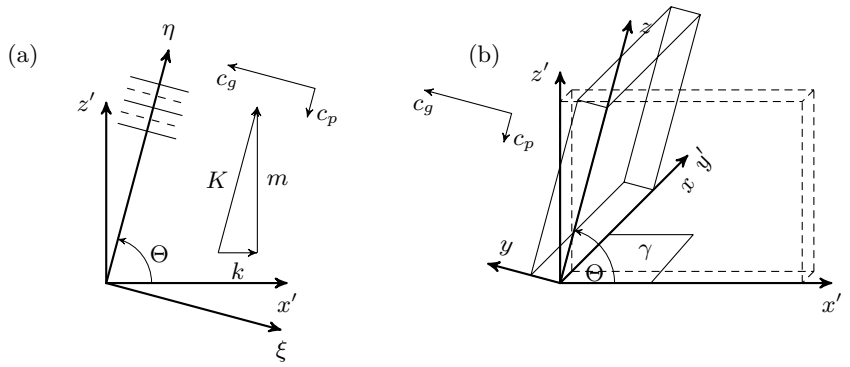

Figure 5.1: Sketch showing the relation between the different coordinate systems and the base wave. Panel (a) shows the rotation of the Earth's coordinate system $[x', y', z']$ about the y'-axis such that the base wavenumber $\mathbf{K}$ is aligned with the vertical axis η. Panel (b) shows the computational domain in the two-times rotated coordinate system $[x, y, z]$.

& Schmitz, 2006), and I the imaginary unit. Here, we will focus on two-dimensional waves that propagate at an angle Θ with the x'-direction (see Fig. 5.1a). In these cases, the gravity wave can be written as

$$[u', v', w', b'] = \Re\left\{a\left[i\frac{\omega}{k}, \frac{f_c}{k}, -i\frac{\omega}{m}, -\frac{N^2}{m}\right]e^{i(kx'+mz'-\omega t)}\right\}, \tag{5.2}$$

where k and m are the components of the base wavenumber vector $\mathbf{K}$, such that the wavelength is $\Lambda = 2\pi/K$ with $K = \|\mathbf{K}\| = \sqrt{k^2+m^2}$. In Eq. (5.2), the wave frequency ω is defined as

$$\omega^2 = N^2\cos^2\Theta + f_c^2\sin^2\Theta, \tag{5.3}$$

and a is a non-dimensional amplitude. For $a = 1$ and $t = 0$ the wave is neutrally stable at its least static stable point, i.e., $\partial b/\partial z' = -N^2$ at $\phi = kx' + mz' = 3\pi/2$; see Yau *et al.* (2004), for example.

Throughout this work, we consider inertia-gravity waves with phase velocity $\mathbf{c_p}$ and group velocity $\mathbf{c_g}$ as illustrated in Fig. 5.1. To ease the representation of the inertia-gravity wave, we introduce a sequence of coordinate transformations, which is better understood by looking at Fig. 5.1b. The first transformation is a counterclockwise rotation by $\pi/2 - \Theta$ around the positive y'-direction, such that in the rotated coordinate system (ξ, y', η), the η-direction is aligned with the wavenumber vector $\mathbf{K}$. The second transformation, on the other hand, simply rearranges the coordinate system through a $\gamma = \pi/2$ counterclockwise rotation around η. This set of transformation leads to the double-rotated coordinate system $[x, y, z]$, which is related to the Earth's coordinate system $[x', y', z']$ by

$$\begin{aligned} x' &= -y\sin\Theta + z\cos\Theta \\ y' &= x \\ z' &= y\cos\Theta + z\sin\Theta. \end{aligned} \tag{5.4}$$

Accordingly, the relation between the velocity field $[u', v', w']$ in the Earth's coordinate frame and the velocity field $[u, v, w]$ in the double-rotated coordinate system is essentially the same as Eq. (5.4), but with the spatial coordinates replaced by the corresponding velocities, since, e.g., $\mathrm{d}x/\mathrm{d}t = u$ and $\mathrm{d}x'/\mathrm{d}t = u'$. Upon substitution in Eq. (5.2), and taking the real-valued part only, it can be shown that the monochromatic inertia-gravity wave assumes the following form:

$$\begin{aligned} u &= \frac{a f_c}{K \cos\Theta} \cos\phi \\ v &= -\frac{a\omega}{K \sin\Theta \cos\Theta} \sin\phi \\ w &= 0 \\ b &= \frac{aN^2}{K \sin\Theta} \cos\phi. \end{aligned} \tag{5.5}$$

Note that $\phi = (kx' + mz' - \omega t) = (Kz - \omega t)$, which can be obtained with the aid of $k = K\cos\Theta$ and $m = K\sin\Theta$.

5.2.2. Numerical Setup

The design of the initial conditions for the simulations uses previous knowledge on the instability of the inertia-gravity waves. Following Achatz (2007*a*), Fruman & Achatz (2012) and Fruman *et al.* (2014), first a normal mode (NM) analysis of the base wave is performed to identify the perturbation with the largest growth rate. The velocity field of this primary perturbation has three non-zero components that vary along the two spatial directions x and z and which is independent of the third coordinate y. Second, a tangent linear stability analysis about the initial

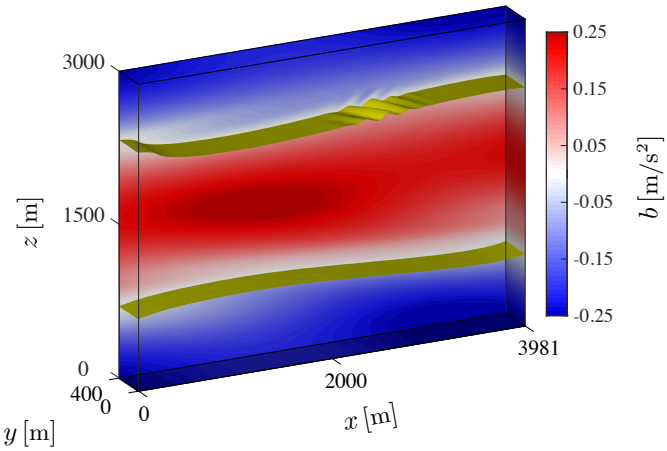

Figure 5.2: Contours of the buoyancy field depicting the initial condition for the simulations of cases IGW81 and IGW72. The yellow isosurfaces ($b = 0$) spanning the x and y-directions outlines the primary and the secondary perturbations of the base wave.

Table 5.1: Physical and numerical parameters for the simulation of cases IGW72 and IGW81.

Domain Size	$L_x = 3981\,\mathrm{m};\ L_y = 400\,\mathrm{m};\ L_z = 3000\,\mathrm{m}$
Wavelength of the basewave	$\Lambda = 3000\,\mathrm{m}$
Wavelengths of the perturbations	$\Lambda_\parallel = 3981\,\mathrm{m};\ \Lambda_\perp = 400\,\mathrm{m}$
Wave Vector Orientation	$\Theta = 89.5°$
Non-dimensional Wave Amplitude	$a = 1.2$
Base Wave Amplitude	$u = 8.97\,\mathrm{m/s};\ v = 14.56\,\mathrm{m/s};\ b = 0.23\,\mathrm{m/s^2}$
Phase Velocity	$\|\mathbf{c_p}\| = -0.106\,\mathrm{m/s}$
Coriolis Parameter	$f_c = 1.367 \times 10^{-4}\,\mathrm{s^{-1}}$
Brunt-Väisälä Frequency	$N = 2 \times 10^{-2}\,\mathrm{s^{-1}}$
Case IGW81:	
Kinematic Viscosity	$\nu = 1\,\mathrm{m^2 s^{-1}}$
Number of Grid Points	$N_p = 2304 \times 246 \times 1728$
Numerical Resolution	$\Delta x = 1.73\,\mathrm{m};\ \Delta y = 1.63\,\mathrm{m};\ \Delta z = 1.74\,\mathrm{m};$
Case IGW72:	
Kinematic Viscosity	$\nu = 0.25\,\mathrm{m^2 s^{-1}}$
Number of Grid Points	$N_p = 3072 \times 294 \times 2304$
Numerical Resolution	$\Delta x = 1.30\,\mathrm{m};\ \Delta y = 1.36\,\mathrm{m};\ \Delta z = 1.30\,\mathrm{m};$

2.5D dynamics developing after perturbing the wave by its leading normal mode is performed to obtain the fully 3D secondary perturbation, which is taken as the singular vector (SV) that maximizes the perturbation growth within the chosen optimization time (5 minutes). The initial conditions are then finally composed of the base wave superimposed with its primary (NM) and secondary (SV) perturbations and are fully three-dimensional owing to the singular vector — see Fig. 5.2 for an illustration of the initial conditions.

Using this technique, we examine two inertia-gravity waves with vertical wavelength $\Lambda = 3000\,\mathrm{m}$ propagating at an inclination $\Theta = 89.5°$ and at different altitudes in the middle atmosphere, namely at 81 km and at 72 km. The corresponding horizontal wavelength of the basewave in the Earth frame of reference is $\Lambda_{x'} = 343\,\mathrm{km}$. The Coriolis parameter is taken from the f-plane approximation for a latitude $\beta = 70°$, i.e., $f_c = 1.367 \times 10^{-4}\,\mathrm{s^{-1}}$, and the Brunt-Väisälä frequency is taken as constant in the range $72 - 81\,\mathrm{km}$ with $N = 2 \times 10^{-2}\,\mathrm{s^{-1}}$. In terms of physical parameters, the only difference between the two cases, henceforth referred to as IGW81 and IGW72, is the kinematic viscosity ν, which we estimate from the US standard atmosphere model for the corresponding altitudes. The Reynolds number based on the wavelength of the base wave Λ and on the buoyancy period $T_b = 2\pi/N$ is $Re = \Lambda^2/(\nu T_b) = 28\,647$ (case IGW81) and $Re = 114\,591$ (case IGW72). In both cases, the ratio of kinematic viscosity to thermal diffusivity is assumed to be

$Pr = \nu/\alpha = 1$, where Pr is the Prandtl number.

The wavelength of the base wave (Λ) defines the extension of the numerical domain in the z-direction, whereas the wavelengths of the perturbations, i.e., the leading NM with $\Lambda_{\parallel} = 3981\,\mathrm{m}$ and the SV with $\Lambda_{\perp} = 400\,\mathrm{m}$, determines the normal (x) and the transversal (y) domain size: $[L_x, L_y, L_z] = [\Lambda_{\parallel}, \Lambda_{\perp}, \Lambda] = [3981, 400, 3000]\mathrm{m}$.

The set of equations Eq. (5.1) are solved numerically using the pseudospectral technique. To compute the spatial gradients, we employ dealiased (2/3-rule) fast Fourier Transforms (Pekurovsky, 2012). For time integration, we use a third-order low-storage Runge-Kutta scheme to integrate the nonlinear, the Coriolis, and the buoyancy diffusivity terms, whereas the viscous forces are integrated exactly using the integrating factor technique (Rogallo, 1977). For comparison, note that in Remmler *et al.* (2013) the spatial gradients are approximated with a 4th order finite volume scheme. Further, as in Remmler *et al.* (2013), we continuously translate the numerical domain along the direction of wave propagation, i.e., z, as if we were following the base wave. The translation velocity equals to the magnitude of the phase-velocity.

The numerical tool is essentially the same as in Pestana & Hickel (2019*b*), with minor modifications to accommodate the solution of an additional scalar transport equation for the buoyancy field. The total number of grid points is $N_p = 2304 \times 246 \times 1728$ in case IGW81 and $N_p = 3072 \times 294 \times 2304$ in case IGW72. The corresponding numerical resolution along the different directions $[\Delta x, \Delta y, \Delta z]$ is $[1.73, 1.63, 1.74]\mathrm{m}$ for IGW81 and $[1.30, 1.36, 1.30]\mathrm{m}$ for IGW72.

For a summary of the physical and numerical parameters, please refer to Table 5.1.

5.3. RESULTS

Before we present the results, let us first introduce some notation. For any variable, the angular brackets represent spatial averages, i.e., $\langle \cdot \rangle_{\mathcal{L}}$ are box-averages, whereas $\langle \cdot \rangle_{xy}$ represent plane averages along the x and y directions. Spatial fluctuations with respect to plane averages are denoted by a prime, e.g., the fluctuation of the velocity in the x-direction is $u' = u - \langle u \rangle_{xy}$. When convenient, we use indices to denote the different Cartesian directions, i.e., the velocity field $[u, v, w]$ is also referred to as $[u_1, u_2, u_3]$. Unless stated otherwise, summation over repeated indices is implied.

Cases IGW72 and IGW81 were integrated in time for 6 h. The total simulated time is slightly shorter than the wave period $T_w = \Lambda/c_p$, which is approximately 8 h. As we will see in the qualitative and quantitative analysis below, the most interesting differences in the breaking behavior of the two cases occur within the simulated first couple of hours.

To asses the sufficiency of the numerical resolution in resolving the smallest scales of turbulence, we estimated the Kolmogorov lengthscale by computing

$$\ell_{kolmo} = \left[\left(\frac{\nu^3}{\varepsilon\, k} \right)^{1/4} \right] \tag{5.6}$$

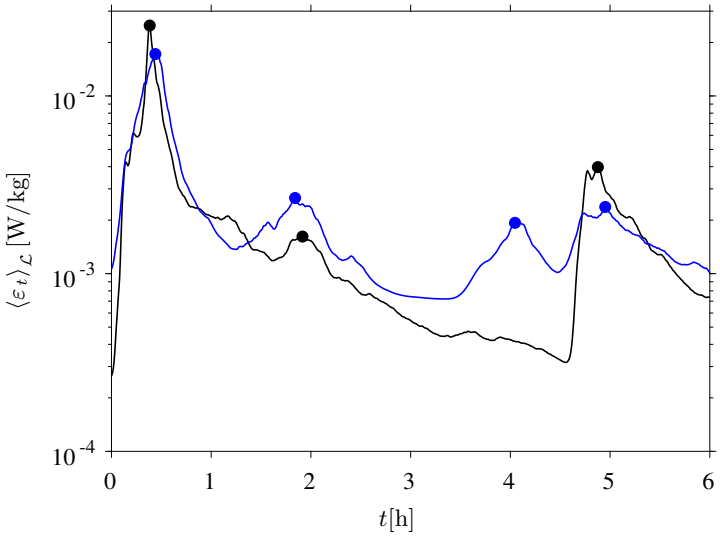

Figure 5.3: Time evolution of the total energy dissipation rate $\langle \varepsilon_t \rangle_{\mathcal{L}}$ for cases IGW81 (—) and IGW72 (—). The filled circles indicate local maxima and the instant of each breaking event.

locally and for every instant of time. In Eq. (5.6), $\varepsilon_k = 2S_{ij}S_{ij}$ is the local kinetic energy dissipation rate, with $S_{ij} = (\partial u_i/\partial x_j + \partial u_j/\partial x_i)/2$ the strain-rate tensor.

We find that for case IGW81, the numerical resolution guarantees that approximately at all times $\Delta < \pi\ell_{kolmo}$ (Kaneda *et al.*, 2003), where Δ is the smallest grid width, i.e., $\Delta = \min\{\Delta x, \Delta y, \Delta z\}$. For case IGW72, the resolution is lower and satisfies, on average, $\Delta < 1.43\pi\ell_{kolmo}$. We are thus confident that both simulations resolve the small-scale turbulent motion and that the results would remain unchanged if the mesh is further refined.

5.3.1. Flow Field Description

A flow field visualization provides us with the general picture of the problem. In addition to several instantaneous snapshots (Figs. 5.4 and 5.5), 2 videos are included as supplementary material (Movie 1 and Movie 2). During the course of the simulation, we observe that bursts of turbulence induce small-scale motion in the overall large-scale flow. In both cases, however, turbulence is not omnipresent; it is instead confined to certain regions of the domain and peculiar of specific time intervals. The main qualitative difference between cases IGW81 and IGW72 is the presence of much finer scales of motion in the latter, a natural consequence of its higher Reynolds number.

The primary and secondary perturbations that define the initial conditions cause the wave to break almost instantly in both cases. The breaking events begin with three-dimensional flow structures developing in the upper-half of the domain where the base wave is least stable, i.e., $\phi = 3\pi/2$ for $z = (3/4)\Lambda = 2250\,\mathrm{m}$ cf. Sec-

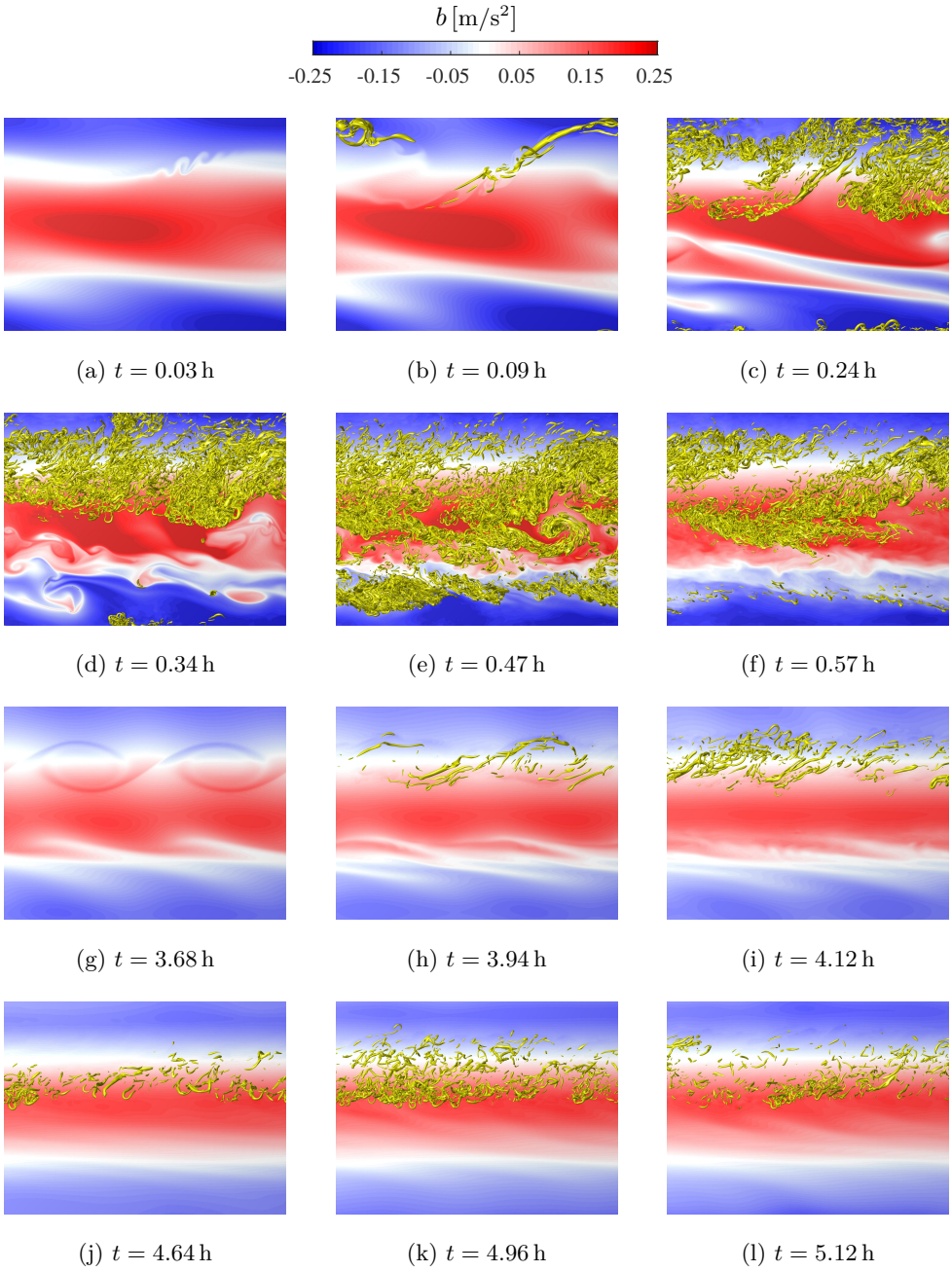

(a) $t = 0.03\,\mathrm{h}$ (b) $t = 0.09\,\mathrm{h}$ (c) $t = 0.24\,\mathrm{h}$

(d) $t = 0.34\,\mathrm{h}$ (e) $t = 0.47\,\mathrm{h}$ (f) $t = 0.57\,\mathrm{h}$

(g) $t = 3.68\,\mathrm{h}$ (h) $t = 3.94\,\mathrm{h}$ (i) $t = 4.12\,\mathrm{h}$

(j) $t = 4.64\,\mathrm{h}$ (k) $t = 4.96\,\mathrm{h}$ (l) $t = 5.12\,\mathrm{h}$

Figure 5.4: Instantaneous flow-field visualizations for case IGW81 showing the isosurfaces $Q = 0.004\,\mathrm{s}^{-2}$ on top of contours of the buoyancy field on the plane $y = 400\,\mathrm{m}$. Panels (a) to (f) correspond to the first breaking event, whereas panels (g) to (i) and panels (j) to (l) correspond to the third and fourth events, respectively.

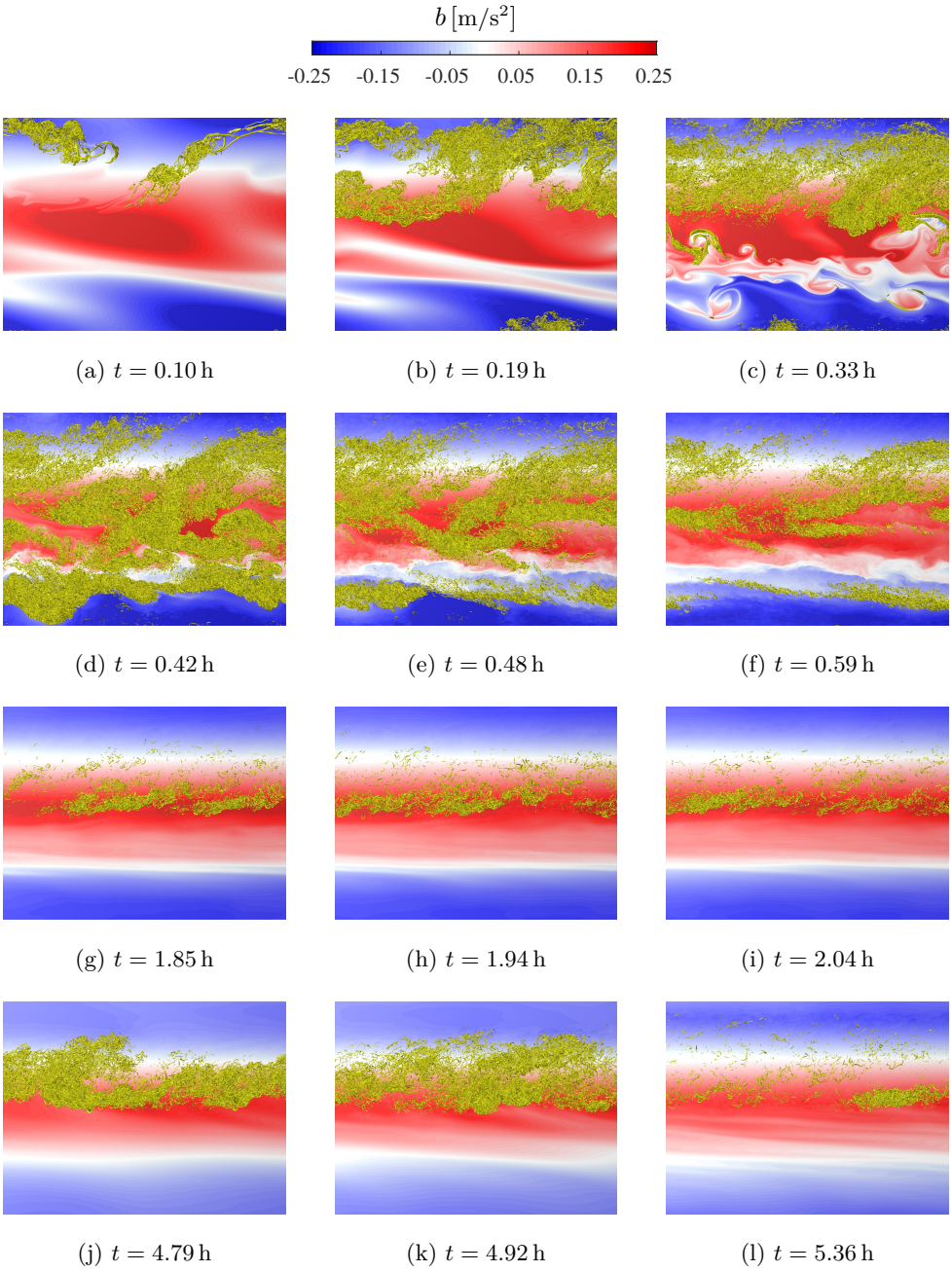

(a) $t = 0.10\,\mathrm{h}$ (b) $t = 0.19\,\mathrm{h}$ (c) $t = 0.33\,\mathrm{h}$

(d) $t = 0.42\,\mathrm{h}$ (e) $t = 0.48\,\mathrm{h}$ (f) $t = 0.59\,\mathrm{h}$

(g) $t = 1.85\,\mathrm{h}$ (h) $t = 1.94\,\mathrm{h}$ (i) $t = 2.04\,\mathrm{h}$

(j) $t = 4.79\,\mathrm{h}$ (k) $t = 4.92\,\mathrm{h}$ (l) $t = 5.36\,\mathrm{h}$

Figure 5.5: Instantaneous flow-field visualizations for case IGW72 showing the isosurfaces $Q = 0.03\,\mathrm{s}^{-2}$ on top of contours of the buoyancy field on the plane $y = 400\,\mathrm{m}$. Panels (a) to (f) correspond to the first breaking event, whereas panels (g) to (i) and panels (j) to (l) correspond to the second and the third events, respectively.

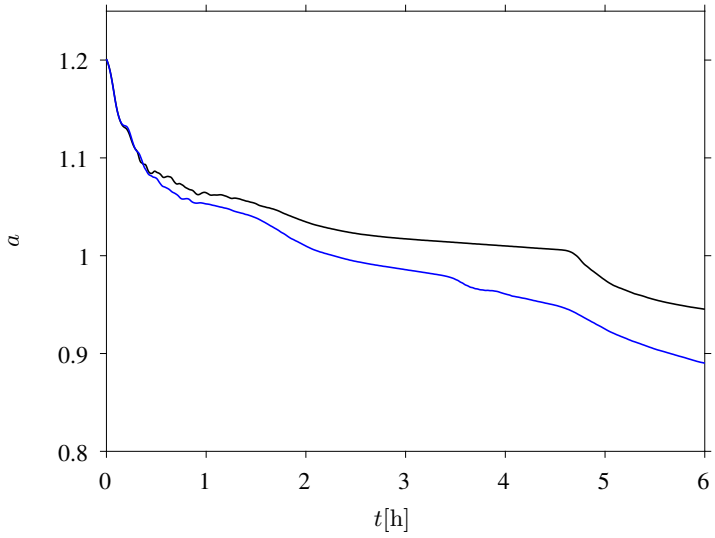

Figure 5.6: Time evolution of the non-dimensional wave amplitude a for cases IGW81 (—) and IGW72 (—).

tion 5.2.1. (Note that the unstable region remains always located in the upper-half of the domain, because the coordinate system is continuously translated with the phase speed). Thereupon, the flow structures are continuously transported horizontally and eventually they spread over the entire domain. Although these features are salient during the first hours of the simulation (Figs. 5.4a to 5.4f and Figs. 5.5a to 5.5f), this sequence of events also reoccurs at later times, but with weaker intensity.

To identify the actual time and the number of breaking events, we follow the temporal evolution of the total energy dissipation rate:

$$\langle \varepsilon_t \rangle_{\mathcal{L}} = 2\nu \langle S_{ij} S_{ij} \rangle_{\mathcal{L}} + \frac{\alpha}{N^2} \left\langle \frac{\partial b}{\partial x_i} \frac{\partial b}{\partial x_i} \right\rangle_{\mathcal{L}}, \tag{5.7}$$

where the first and the second term on the right-hand-side are the kinetic energy dissipation rate $\langle \varepsilon_k \rangle_{\mathcal{L}}$ and the potential energy dissipation rate $\langle \varepsilon_b \rangle_{\mathcal{L}}$, respectively.

The total energy dissipation rate increases significantly at the times for which turbulent spots dominate the flow-field. By following the time evolution of $\langle \varepsilon_t \rangle_{\mathcal{L}}$ (Fig. 5.3), we observe 4 peaks in $\langle \varepsilon_t \rangle_{\mathcal{L}}$ for case IGW81, whereas 3 peaks are seen for case IGW72. By searching for local maxima, we identify the time of each breaking event as $t_{be} = \{0.44; 1.84; 4.05; 4.95\}$ h for IGW81 and $t_{be} = \{0.38; 1.92; 4.88\}$ h for IGW72. Although the evolution of $\langle \varepsilon_t \rangle_{\mathcal{L}}$ is alike during the first breakdown for the two Reynolds numbers, differences in magnitude and duration are evident for the remaining breaking events. For example, for the second breaking event, at around $t = 1.88$ h, $\langle \varepsilon_t \rangle_{\mathcal{L}}$ is approximately 1.6 times larger for case IGW81 than for

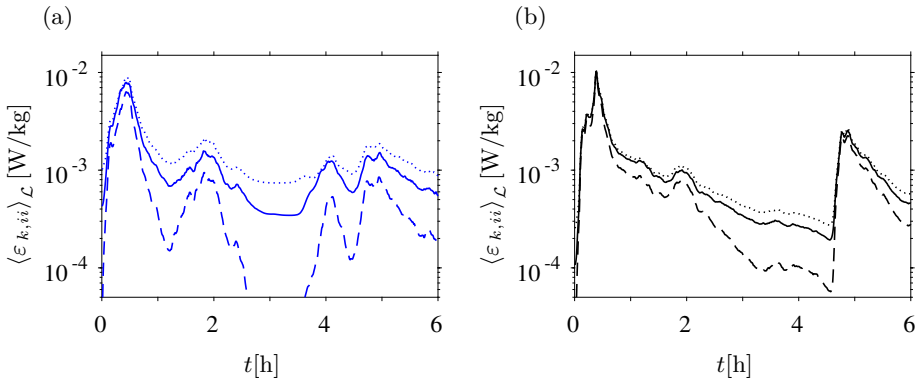

Figure 5.7: Time evolution of the components of the kinetic energy dissipation rate tensor for cases IGW81 (a) and IGW72 (b): $\langle \varepsilon_{k,11} \rangle_{\mathcal{L}}$ (—), $\langle \varepsilon_{k,22} \rangle_{\mathcal{L}}$ (·····) and $\langle \varepsilon_{k,33} \rangle_{\mathcal{L}}$ (- - -).

case IGW72. The inverse is observed however for the last breaking event, at around $t = 5\,\mathrm{h}$, where $\langle \varepsilon_t \rangle_{\mathcal{L}}$ for case IGW72 is larger than for IGW81 by roughly the same factor.

This sequence of breaking events causes the non-dimensional wave amplitude a to decay monotonically with time (Fig. 5.6). For $t \lesssim 0.5\,\mathrm{h}$, $a(t)$ follows the same trend in both cases and decays rapidly. This is probably a consequence of the well-defined initial conditions, which cause the first breaking event to be similar in both cases. At posterior times, the decay rate reduces significantly. Case IGW72 exhibits a slower decay rate, as is expected from a laminar decay: for $Pr = 1$, the non-dimensional wave amplitude of an unperturbed laminar wave evolves as $a_{lam}(t) = a_0, \exp(-\nu K^2 t)$ (Fruman *et al.*, 2014). More interesting, we also notice that the third and fourth breaking for case IGW81 occurs although the non-dimensional amplitude is below the limit for static instability, i.e., $a < 1$. For case IGW72, $a > 1$ for the majority of the simulation time, but during the last breaking event a is also smaller than 1.

5.3.2. Dissipation Tensor Anisotropy

The contributions of the kinetic and the potential energy dissipation rate to $\langle \varepsilon_t \rangle_{\mathcal{L}}$ (Eq. (5.7)) differ strongly between both cases, and varies over time. In fact, Fig. 5.8 shows that the main contributor to $\langle \varepsilon_t \rangle_{\mathcal{L}}$ is $\langle \varepsilon_k \rangle_{\mathcal{L}}$. By comparing the temporal evolution of the kinetic and potential energy dissipation rates, we find from Figs. 5.8a and 5.8b that at the peak of the first breaking event the ratio $\langle \varepsilon_k \rangle_{\mathcal{L}} / \langle \varepsilon_b \rangle_{\mathcal{L}}$ is approximately 1.96 irrespective of the Reynolds number. Nevertheless, the disparity between the two quantities increases at later times. For example, at the last breaking event of case IGW72 the ratio is approximately 16.1.

More information regarding the structure of the energy dissipation tensor is obtained by decomposing it into its individual components along the three Cartesian

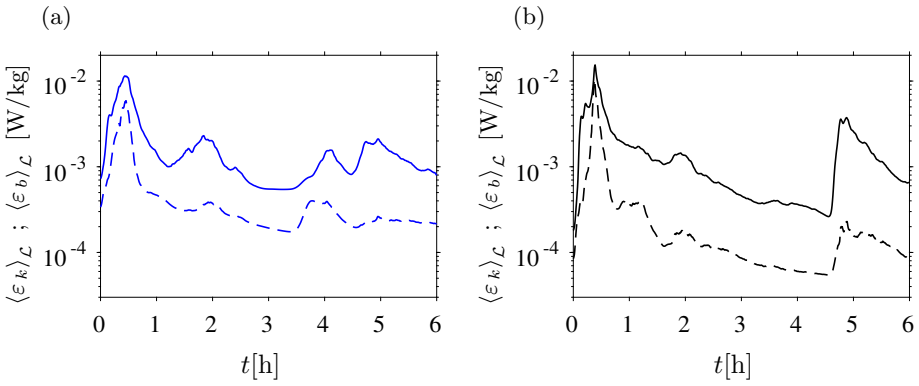

Figure 5.8: Time evolution of the kinetic and potential energy dissipation rate for cases IGW81 (a) and IGW72 (b): $\langle \varepsilon_k \rangle_{\mathcal{L}}$ (—) and $\langle \varepsilon_b \rangle_{\mathcal{L}}$ (- - -).

directions, i.e.:

$$\langle \varepsilon_k \rangle_{\mathcal{L}} = \frac{1}{2} \left(\langle \varepsilon_{k,11} \rangle_{\mathcal{L}} + \langle \varepsilon_{k,22} \rangle_{\mathcal{L}} + \langle \varepsilon_{k,33} \rangle_{\mathcal{L}} \right). \tag{5.8}$$

By assessing the relative importance of each term on the right-hand-side of the equation above (Fig. 5.7), we find that all three components contribute almost equally to $\langle \varepsilon_k \rangle_{\mathcal{L}}$ at instants of time corresponding to the wave breakdown. The later observation, however, is more explicit for the higher Reynolds number case (Fig. 5.7b). Although we also observe the same tendency for the lower Reynolds number (Fig. 5.7a), the difference between the components is still significant. Put together, these results indicate that for increasing Reynolds number, we can expect the energy dissipation tensor to attain an isotropic structure during the phases with high turbulence intensity, while during calmer periods, we can expect the kinetic energy dissipation tensor to have a strongly anisotropic structure. A certainly interesting observation is that the component aligned with the direction of wave propagation has the smallest contribution to the energy dissipation for both cases.

5.3.3. Hovmöller Diagrams

Now, we turn our attention to the distribution of different quantities along the direction of wave propagation. In particular, we look at the spatial distribution of ε_k and ε_b and their relation to the Richardson number (Ri). For this purpose, we average the different quantities over planes normal to the direction of propagation to obtain $\langle \varepsilon_k \rangle_{xy}$, $\langle \varepsilon_b \rangle_{xy}$ and $\langle Ri \rangle_{xy}$. Whereas the kinetic and potential energy dissipation are obtained similarly to Eq. (5.7), the Richardson number follows from the local balance between buoyancy gradients and shear rate. In the Earth's frame of reference, it is given as

$$Ri = \frac{N^2 + \partial b / \partial z'}{(\partial u / \partial z')^2 + (\partial v / \partial z')^2}. \tag{5.9}$$

The Richardson number is computed in the rotated frame of reference $[x, y, z]$ by projection of the gradients.

A first hint towards the spatial distribution of the energy dissipation rate can be obtained from the previous flow-field visualization. For instance, a comparison of the first breaking event in both cases (Figs. 5.4a to 5.4f and Figs. 5.5a to 5.5f) shows that the regions of stronger spatial gradients in the buoyancy field (lower-half of the domain cf. Fig. 5.4c) do not coincide with the location of the eddies. In the upper-half of the domain, the isopycnals are primarily horizontal and neatly separated from each other, whereas the lower-half of the domain shows regions of intense mixing in the buoyancy field and consequently larger spatial gradients.

To confirm these observations, we present in Fig. 5.9 Hovmöller diagrams of $\langle \varepsilon_k \rangle_{xy}$, $\langle \varepsilon_b \rangle_{xy}$ and $\langle Ri \rangle_{xy}$, i.e., their evolution as a function of z and t. From Figs. 5.9a and 5.9d, we see that large values of $\langle \varepsilon_k \rangle_{xy}$ dominate the region $z > 1.5\,\mathrm{km}$ and persist in this location for the entire simulation time. On the contrary, Figs. 5.9b and 5.9e show that high dissipation of potential energy is found for $z < 1.5\,\mathrm{km}$ and it is restricted to $t < 2\,\mathrm{h}$. Overall, we see that the upper-half of the domain is marked by a higher level of turbulence activity (stronger spatial gradients), in agreement with the visualization of finer scales in the same region.

Regardless of the Reynolds number, the regions of intense dissipation of kinetic energy are more likely to be found within an envelope delimited by the stability threshold, i.e., $\langle Ri \rangle_{xy} = 0.25$. Figures 5.9c and 5.9f show that values for which $\langle Ri \rangle_{xy} < 0.25$ are predominantly located in the upper-half of the domain, thus evidencing the unstable nature of the upper-half of the wave domain. For comparison, we superimpose the contour $\langle Ri \rangle_{xy} = 0.25$ on the distribution of $\langle \varepsilon_k \rangle_{xy}$ and $\langle \varepsilon_b \rangle_{xy}$ — see Figs. 5.9a, 5.9b, 5.9d and 5.9e. We observe that $\langle Ri \rangle_{xy} = 0.25$ delineates the region of high kinetic energy dissipation well, indicating a correlation between both quantities.

For these results, there are no significant differences between cases IGW81 and IGW72, apart from the fact that in case IGW72, the regions of intense kinetic energy dissipation are broader and better defined than in case IGW81. Incidentally, as observed by Remmler *et al.* (2013) for case IGW81, Figs. 5.9a and 5.9b also show us that in both cases the last breaking event occurs when remnant turbulence from the first breaking event meets the least unstable region of the base wave. This observation follows from tracking the evolution of a fixed point in the Earth's frame of reference, as represented by the dashed line in that figure. Although case IGW81 shows a clearer region of somewhat high kinetic energy dissipation traveling with the phase speed in the co-moving frame of reference, case IGW72 indicates that an even lower small-scale turbulence activity might be already sufficient to trigger instabilities and be amplified.

5.3.4. Energy Spectra

The distinct turbulence level characteristic of the different time instants is also reflected in both the kinetic and potential energy spectra. In Fig. 5.10 we show the spectra in terms of the vertical wavelength λ_z for both cases. The kinetic and

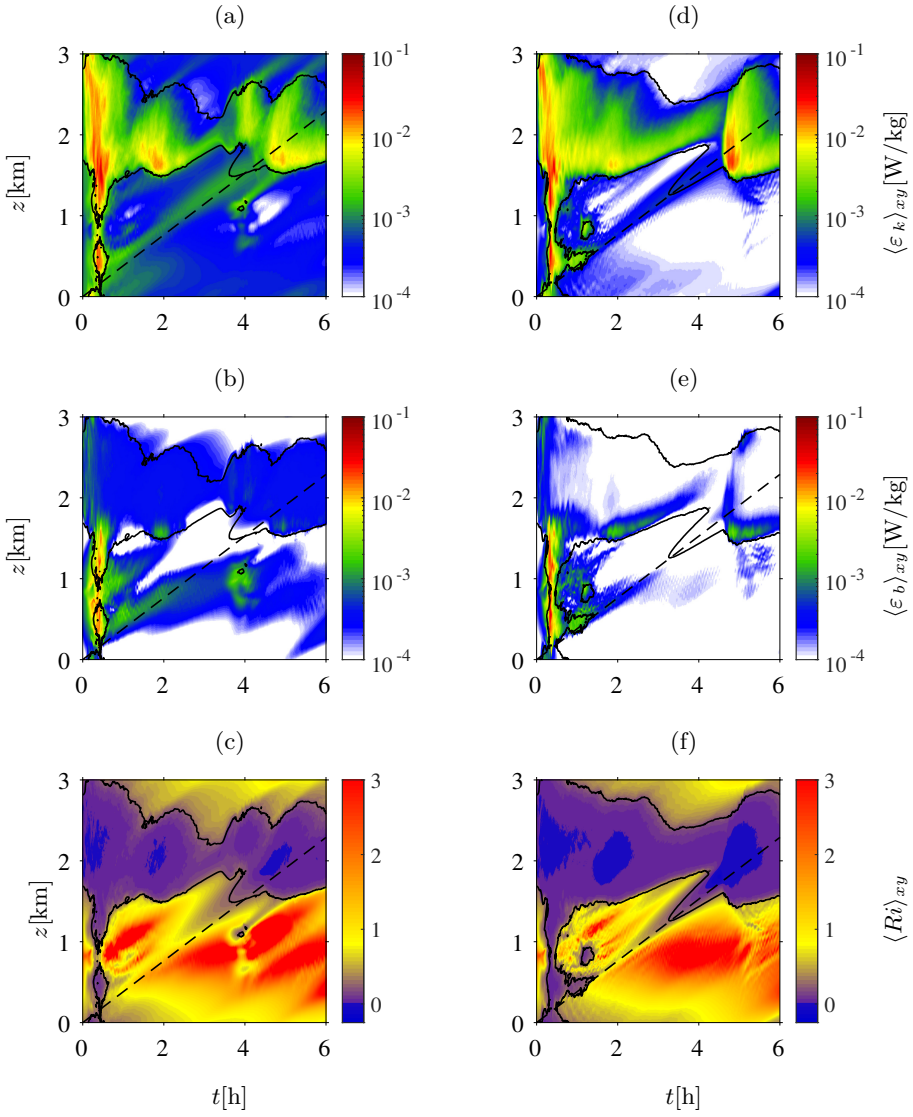

Figure 5.9: Hovmöller plots of the kinetic and potential energy dissipation rates, and the Richardson number. Left and right panels shows cases IGW81 and IGW72, respectively. The black solid line (—) represents the contour line $Ri = 0.25$, and the dashed line (- - -) tracks a fixed position in the Earth's frame of reference.

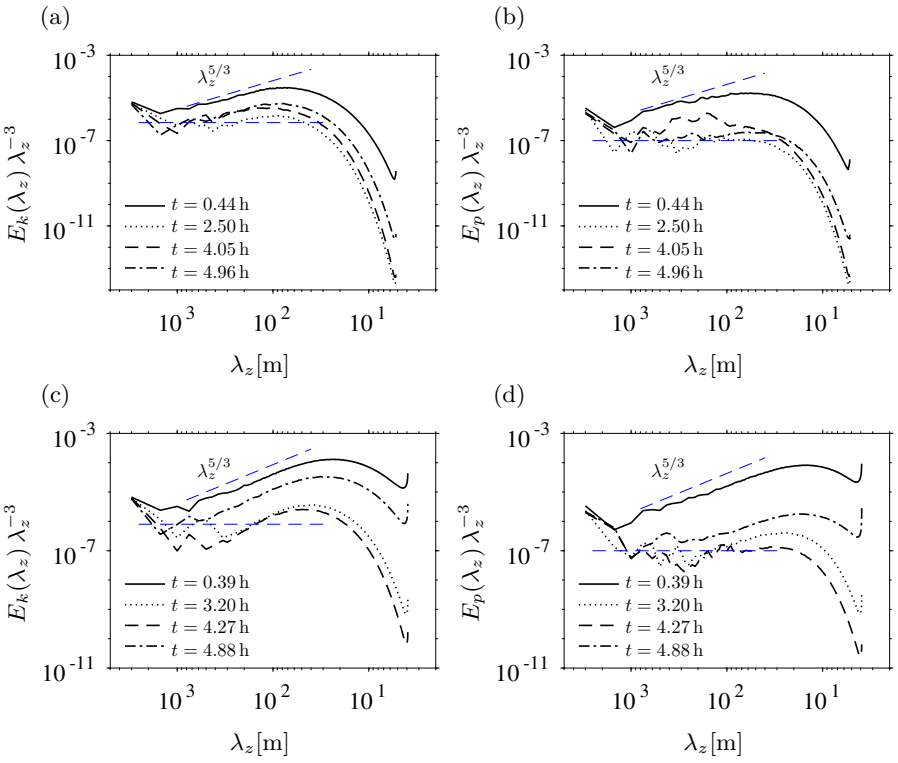

Figure 5.10: Compensated kinetic and potential energy spectra plotted over the vertical wavelength λ_z for different time instants. (a) and (b): case IGW81 (upper panels). (c) and (d): case IGW72 (lower panels). The thin dashed blue lines (- - -) indicates the $\lambda_z^{5/3}$ and λ_z^3 scaling laws.

potential energy spectra, $E_k(\lambda_z)$ and $E_p(\lambda_z)$ respectively, are defined such that

$$\int_{\lambda_z} E_k(\lambda_z)\,\mathrm{d}\lambda_z = \langle K \rangle_{\mathcal{L}} \tag{5.10}$$

and

$$\int_{\lambda_z} E_p(\lambda_z)\,\mathrm{d}\lambda_z = \langle A \rangle_{\mathcal{L}}\,, \tag{5.11}$$

where $K = (u_i u_i)/2$ and $A = b^2/(2N^2)$ are the local kinetic and potential energy. For the following comparison of the energy spectra, we intentionally select two time instants during the breaking event and two additional ones at calmer periods, which correspond to off-peak locations in the evolution of $\langle \varepsilon_t \rangle_{\mathcal{L}}$.

At time instants corresponding to the breaking events, $E_k(\lambda_z)$ and $E_p(\lambda_z)$ scales in good agreement with $\lambda_z^{5/3}$. For instance, in case IGW72 (Figs. 5.10c and 5.10d) we observe that for $t = 0.39\,\mathrm{h}$ and $t = 4.88\,\mathrm{h}$, i.e., approximately during the first and the third breaking events, respectively, $E_k(\lambda_z)$ and $E_p(\lambda_z)$ exhibits a $\lambda_z^{5/3}$ scaling from

$\lambda_z = 37\,\mathrm{m}$ to $\lambda_z = 750\,\mathrm{m}$. On the other hand, the same figure shows that quiescent periods, e.g., $t = 3.20\,\mathrm{h}$ and $4.27\,\mathrm{h}$, the scaling of the energy spectra matches better a λ_z^3 law. Put together, these results suggest that during the breaking events the flow field is isotropic, and follows a Kolmogorov scaling of the type $\lambda_z^{5/3}$, which is canonical for homogeneous isotropic turbulence. Further, the λ_z^3 scaling at calmer periods indicates that buoyancy effects are more relevant during periods of decay rather than during the periods of intense wave breaking, since a λ_z^3 is expected in the inertial-range of strongly stratified flows (Brethouwer *et al.*, 2007; Remmler & Hickel, 2013).

Although the power-law dependencies are best seen in case IGW72 (Figs. 5.10c and 5.10d), their footprint is also clear in case IGW81 (Figs. 5.10a and 5.10b). Therefore, we hypothesize that these power laws should remain for even higher Reynolds numbers.

5.3.5. Kinetic and Potential Energy

Here, we leave the Reynolds number comparison aside and focus on the temporal evolution of the box-averaged kinetic energy and available potential energy, as well as on the evolution of their individual components. We only show results for the high Reynolds number case IGW72, since the qualitative behavior for case IGW81 is essentially the same.

The box-averaged kinetic and potential energy evolve in time according to

$$\frac{\mathrm{d}\langle K\rangle_{\mathcal{L}}}{\mathrm{d}t} - \langle bu_i n_i\rangle_{\mathcal{L}} + \langle \varepsilon_k\rangle_{\mathcal{L}} = 0 \tag{5.12}$$

and

$$\frac{\mathrm{d}\langle A\rangle_{\mathcal{L}}}{\mathrm{d}t} + \langle bu_i n_i\rangle_{\mathcal{L}} + \langle \varepsilon_b\rangle_{\mathcal{L}} = 0. \tag{5.13}$$

Figure 5.11 shows each term of the equations above as a function of time. Not surprisingly, $\mathrm{d}\langle K\rangle_{\mathcal{L}}/\mathrm{d}t$ and $\mathrm{d}\langle A\rangle_{\mathcal{L}}/\mathrm{d}t$ are mostly negative, as it is expected for a decaying wave. This observation is in agreement with the previous flow field visualizations, from which we have already seen that flow structures fade away and are less likely to be found towards the end of the simulation. Nevertheless, Fig. 5.11 shows that for certain time windows there is a surplus of energy that causes positive variations in either the kinetic or the potential energy. From Eqs. (5.12) and (5.13) it is clear that this can only occur when the transfer term $\langle bu_i n_i\rangle_{\mathcal{L}}$ becomes larger than the energy dissipation rate. For the kinetic energy, Fig. 5.11a shows that this is the case for $2\,\mathrm{h} < t < 4\,\mathrm{h}$ (approximately), whereas for the potential energy, Fig. 5.11b shows positive variations of $\mathrm{d}\langle A\rangle_{\mathcal{L}}/\mathrm{d}t$ within the interval $4\,\mathrm{h} < t < 6\,\mathrm{h}$. Further, we also notice that during the breaking events, i.e., when dissipation is highest, potential energy is converted into kinetic energy, whereas the opposite prevails during calmer periods; to see that, contrast for example in Fig. 5.11 the behavior of $\langle bu_i n_i\rangle_{\mathcal{L}}$ at $t \approx 0.5\,\mathrm{h}$ and $t \approx 5\,\mathrm{h}$ with its behavior at $t \approx 3\,\mathrm{h}$.

Now, we analyze the individual contributions of the three Cartesian velocity components to the kinetic energy by following in time $\langle uu\rangle_{\mathcal{L}}$, $\langle vv\rangle_{\mathcal{L}}$ and $\langle ww\rangle_{\mathcal{L}}$, and the buoyancy variance $\langle bb\rangle_{\mathcal{L}}/N^2 = 2\langle A\rangle_{\mathcal{L}}$. Results in Fig. 5.12 show that energy is

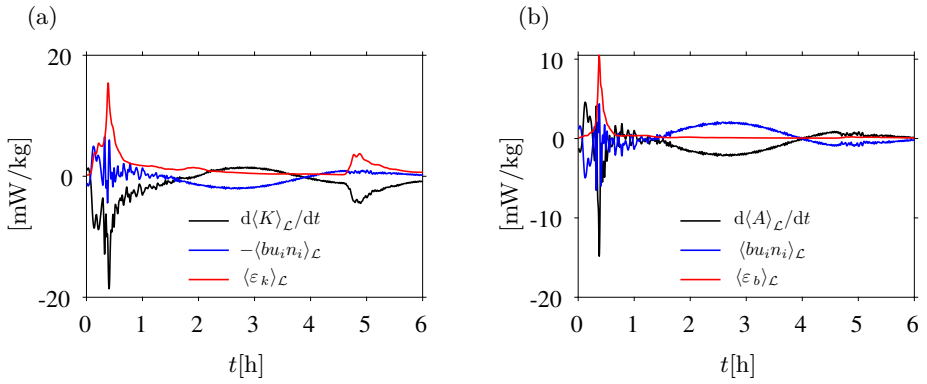

Figure 5.11: Kinetic (a) and potential (b) energy budget as defined in Eqs. (5.12) and (5.13).

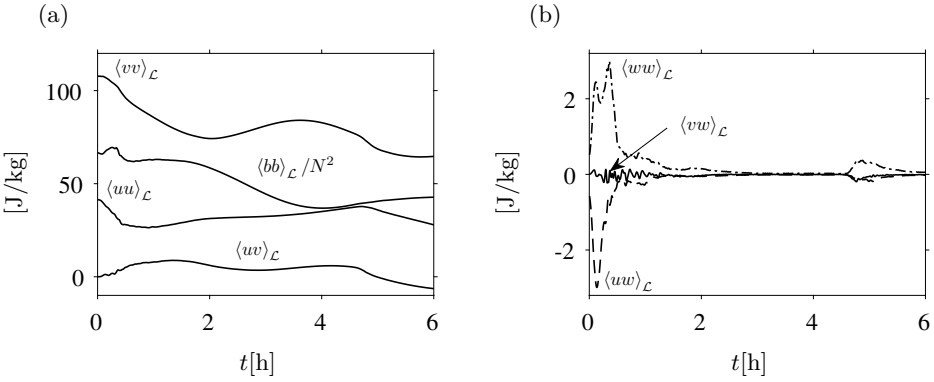

Figure 5.12: Time evolution of the individual components of the kinetic and potential energy and the cross correlations for case IGW72. The data is split in panels (a) and (b) for better visibility.

mostly contained in the $\langle uu\rangle_{\mathcal{L}}$ and $\langle vv\rangle_{\mathcal{L}}$ components. In fact, both of them account for 99% of the total kinetic energy and approximately 69% of the total energy; the potential energy stores the remaining 31% of the total energy. If we focus on the first hour of the simulation, i.e., $t < 0.5\,\mathrm{h}$ (first breaking event), we observe that $\langle uu\rangle_{\mathcal{L}}$ and $\langle vv\rangle_{\mathcal{L}}$ decrease in magnitude, whereas $\langle ww\rangle_{\mathcal{L}}$ and $\langle bb\rangle_{\mathcal{L}}/N^2$ increase. This suggests that during the breaking events energy is transferred to $\langle ww\rangle_{\mathcal{L}}$ and also stored as potential energy. Indeed, at the last breaking event, i.e., $t = 4.88\,\mathrm{h}$, $\langle bb\rangle_{\mathcal{L}}/N^2$ rises once again, although less remarkable than during the first breaking event at $t = 0.38\,\mathrm{h}$.

Regarding the cross correlations, Fig. 5.12 shows that $\langle uv\rangle_{\mathcal{L}}$ is mostly positive, but undergoes a sign change during the third breaking event, $\langle uw\rangle_{\mathcal{L}}$ is slightly negative throughout the whole simulation; $\langle vw\rangle_{\mathcal{L}}$ on the other hand, fluctuates weakly around null (Fig. 5.12b).

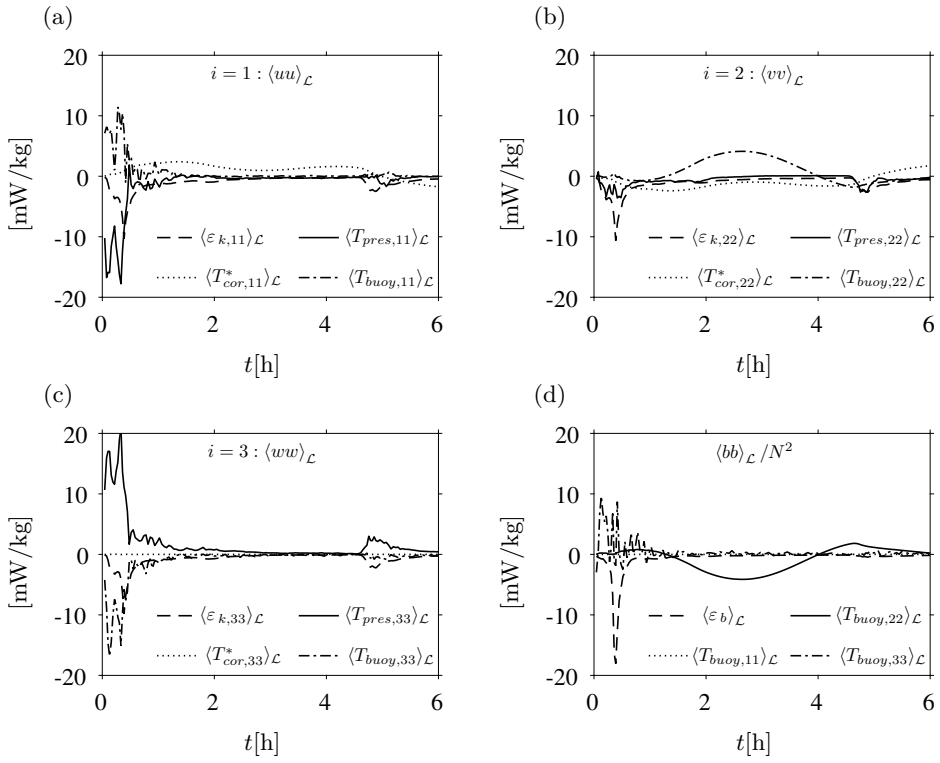

Figure 5.13: Energy budget showing the time evolution of the contribution due to the Coriolis force (T_{cor}), pressure (T_{pres}), buoyancy (T_{buoy}) and dissipation ($\langle \varepsilon_{k,ii} \rangle_{\mathcal{L}}$) for case IGW72. Panels (a) to (c) correspond to $i = \{1, 2, 3\}$ in Eq. (5.14) and panel (d) shows the terms of Eq. (5.15).

5.3.6. The Energy Transfer Mechanism

A more detailed notion of the energy transfer mechanism can be obtained through a energy budget analysis. To this end, we write the (componentwise) evolution equations for the kinetic and potential energy, which are obtained from Eq. (5.1) upon multiplication with the corresponding velocity and buoyancy fields followed by a box-average:

$$\frac{\partial \langle u_i u_i \rangle_{\mathcal{L}}}{\partial t} = \langle T_{pres,ii} \rangle_{\mathcal{L}} - \langle T^*_{cor,ii} \rangle_{\mathcal{L}} + \langle T^*_{buoy,ii} \rangle_{\mathcal{L}} - \langle \varepsilon_{k,ii} \rangle_{\mathcal{L}} \tag{5.14}$$

and

$$\frac{1}{N^2} \frac{\partial \langle bb \rangle_{\mathcal{L}}}{\partial t} = - \langle T_{buoy,11} \rangle_{\mathcal{L}} - \langle T_{buoy,22} \rangle_{\mathcal{L}} - \langle T_{buoy,33} \rangle_{\mathcal{L}} - 2 \langle \varepsilon_b \rangle_{\mathcal{L}} . \tag{5.15}$$

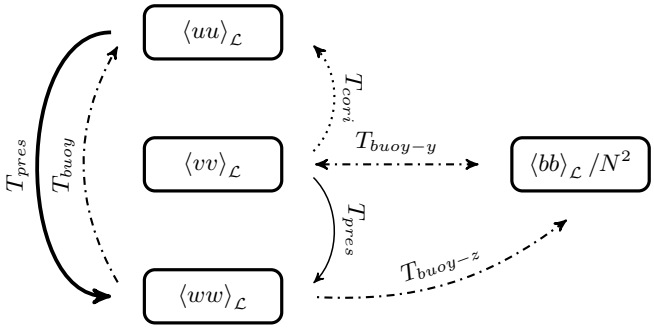

Figure 5.14: Schematic of the energy transfer mechanism and the role of each term during the wave breaking event. Line styles is the same as in Fig. 5.13. The pressure term (T_{pres}) appears as a thicker line to highlight its dominance over the other terms. Note that we have omitted the dissipation in the diagram, since its role is evident.

Equations (5.14) and (5.15) refer to the components of twice the kinetic and potential energy respectively. In Eq. (5.14), no implicit summation over repeated indices is considered, and the subscript i merely indicates the Cartesian direction, i.e., $i = \{1, 2, 3\}$ implies $\{x, y, z\}$. The terms on the right-hand side of Eqs. (5.14) and (5.15) represent the contributions due to the pressure field (T_{pres}), the Coriolis force (T_{cor}), the buoyancy force (T_{buoy}) and the energy dissipation rate. Also, note that a superscript $*$ appears in Eq. (5.14) to indicate the terms that contain contributions from the pressure field, as explained next.

We isolate the influence due to the Coriolis and the buoyant forces in Eq. (5.14) by eliminating their contribution from the pressure field and adding it to their respective transfer terms. That is, first we split the pressure field p, which satisfies the Poisson equation

$$\nabla^2 p = -\nabla \cdot (\mathbf{u} \cdot \nabla \mathbf{u}) - \nabla \cdot (f_c \mathbf{n} \times \mathbf{u}) + \nabla \cdot (b\mathbf{n}), \tag{5.16}$$

such that $p = p_{adv} + p_c + p_b$, where p_{adv}, p_c and p_b are the solutions of Eq. (5.16) considering either the first, second or the third term on the right-hand-side, respectively. Then, we include the effects of p_c and p_b to $T_{cor,ii}$ and $T_{buoy,ii}$, to form $\langle T^*_{cor,ii} \rangle_{xyz}$ and $\langle T^*_{buoy,ii} \rangle_{xyz}$. Hence, $\langle T_{press,ii} \rangle_{xyz}$ in Eq. (5.14) contains only the usual contribution due to p_{adv}. The individual pressure contributions in $\langle T_{press,ii} \rangle_{xyz}$, $\langle T^*_{cor,ii} \rangle_{xyz}$ and $\langle T^*_{buoy,ii} \rangle_{xyz}$ do neither produce nor destroy kinetic energy, but rather redistribute energy between the three velocity components in such a way that the fluid volume is conserved (incompressible flow). The buoyancy term appears in Eq. (5.15) without a $*$, since the pressure field does not play a role in this equation.

The evolution of each term is presented in Fig. 5.13. Figures 5.13a to 5.13c shows the term-by-term energy budget for $i = \{1, 2, 3\}$ and Equation (5.14), whereas Fig. 5.13d presents the results from Eq. (5.15). By individually analyzing the temporal evolution of each term, we find that T_{press} is the main supplier of energy to $\langle ww \rangle_{\mathcal{L}}$; this energy is transferred away from $\langle uu \rangle_{\mathcal{L}}$, as clearly visible during the first breaking event, for which it is evident that $\langle T_{press,11} \rangle$ is negative (Fig. 5.13a) and

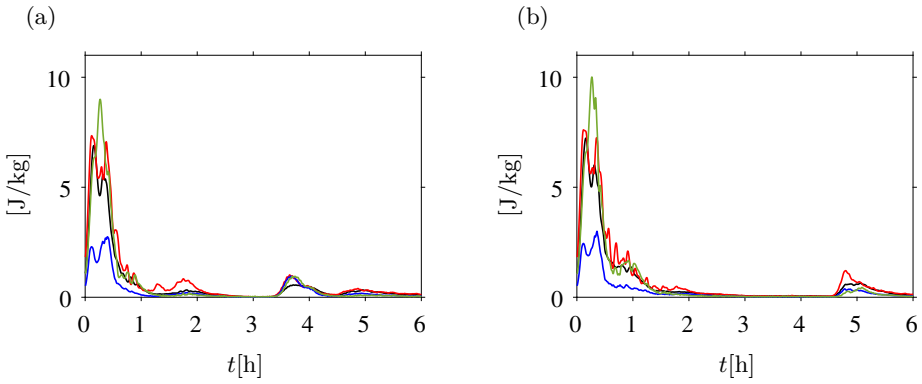

Figure 5.15: Time evolution of the small-scale fluctuation covariances for case IGW81 (a) and case IGW72 (b). Different line colors denote the different terms: $\langle u'u' \rangle_{\mathcal{L}}$ (—), $\langle v'v' \rangle_{\mathcal{L}}$ (—), $\langle w'w' \rangle_{\mathcal{L}}$ (—) and $\langle b'b' \rangle_{\mathcal{L}}/N^2$ (—).

$\langle T_{press,33} \rangle$ is positive with roughly the same magnitude variation in time (Fig. 5.13c). We attribute this fact to the primary instability, which is predominantly aligned with the x and y directions and the main reason for the roll-up of eddies observed prior to the first breaking event.

Regarding the conversion from kinetic to potential energy, we see from Fig. 5.13d that $\langle T_{buoy,33} \rangle_{\mathcal{L}}$ is positive when the wave breaks, and the corresponding $\langle T^*_{buoy,33} \rangle_{\mathcal{L}}$ is essentially negative in Fig. 5.13c. Therefore, we conclude that most of the energy gained by $\langle ww \rangle_{\mathcal{L}}$ through $\langle T_{press,33} \rangle_{\mathcal{L}}$ is converted into potential energy by $\langle T_{buoy,33} \rangle_{\mathcal{L}}$. The difference between the sink $\langle T^*_{buoy,33} \rangle_{\mathcal{L}}$ in the $\langle ww \rangle_{\mathcal{L}}$ balance and $\langle T_{buoy,33} \rangle_{\mathcal{L}}$, which is a source for $\langle bb \rangle_{\mathcal{L}}/N^2$, is due to the pressure contribution which transfers energy to the other components of the kinetic energy, in particular to $\langle uu \rangle_{\mathcal{L}}$. In Fig. 5.14, we include a diagram that summarizes the transfer mechanism and the function/relevance of each term in Eqs. (5.14) and (5.15).

5.3.7. Turbulent Kinetic and Potential Energy

So far, we have looked at the wave breakdown from a global sense, i.e., the velocity and buoyancy fields represented both the decaying base wave and the turbulent structures. Although information about the global quantities are valuable for modeling approaches which do not resolve any scale of the wave, more refined models would probably aim at resolving at least the base wave and parameterizing only small-scale turbulent fluctuations. To this end, we decompose the velocity and the buoyancy field in two contributions: one related to the base wave and a second related to small-scale fluctuations.

To split the fields we first average them over xy-planes and then compute the difference between the average and the local solution, e.g., the x-component of the velocity field is $u(x,y,z) = \langle u \rangle_{xy}(z) + u'(x,y,z)$. Throughout time, the vertical profiles of the mean kinetic and mean potential energy of the large scales, i.e., $\langle u_i \rangle_{xy} \langle u_i \rangle_{xy}/2$ and $\langle b \rangle_{xy} \langle b \rangle_{xy}/(2N^2)$, remain similar to the profiles obtained with

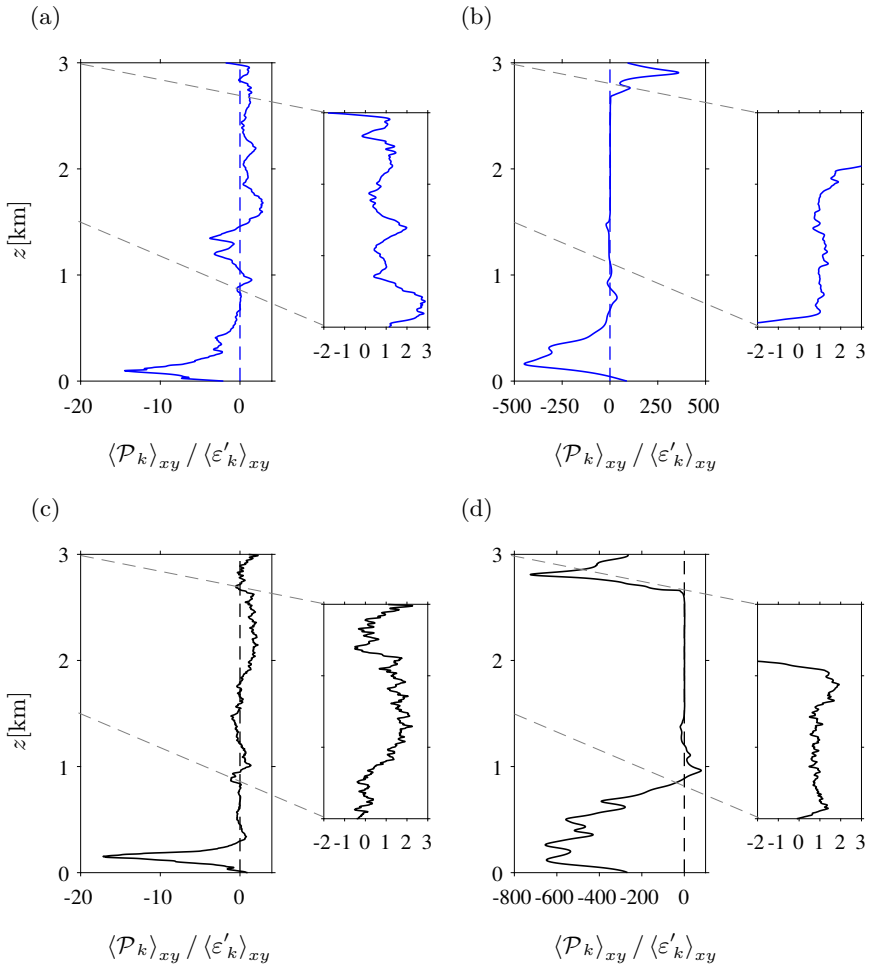

Figure 5.16: Vertical profiles of the ratio between the kinetic energy production and the (pseudo) kinetic energy dissipation rate for case IGW81 (top panels) and for case IGW72 (lower panels). Panels (a) and (c) correspond to the first breaking event for the respective cases, whereas (b) and (d) correspond to the last breaking event.

the full field (not shown). From the terms that constitute the mean kinetic energy, $\langle u \rangle_{xy} \langle u \rangle_{xy}$ is the one that changes the most in time (although modestly). In fact, we already saw in the previous section that this term is the one responsible for supplying energy to the third velocity component.

The temporal evolution of the fluctuation covariances, i.e., $\langle u'u' \rangle_{\mathcal{L}}$, $\langle v'v' \rangle_{\mathcal{L}}$, $\langle w'w' \rangle_{\mathcal{L}}$ and $\langle b'b' \rangle_{\mathcal{L}}/N^2$, shows that during the breaking events there is a significant increase of energy in the small-scale fluctuations, thus consistent with the idea that when the wave breaks, energy is extracted from the base wave (mean flow). This is clear from Fig. 5.15, which also shows that the energy gain by the fluctu-

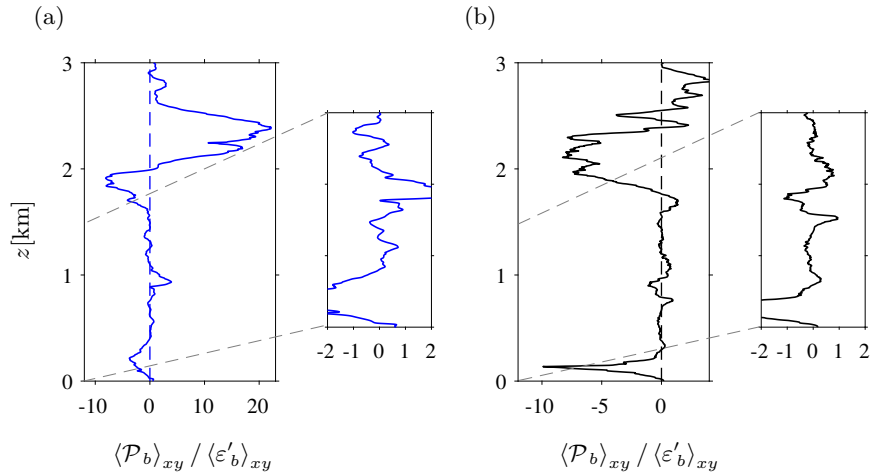

Figure 5.17: Vertical profiles of the ratio between the potential energy production and the (pseudo) potential energy dissipation rate for case IGW81 (left) and for case IGW72 (right). The panels correspond to the first breaking event in both cases.

ations is more pronounced for the first breaking event, implying that this event is indeed stronger than the others.

The split of the velocity field allows us also to explore the energy transfer between the mean and the fluctuating fields. Writing the governing equations for the energy of the mean and the fluctuating fields, one sees that they include coupling terms, namely the production of kinetic and potential energy, which are sink terms for the mean kinetic and potential energy equation, and source terms in the corresponding equation for the energy of the fluctuations. The production of kinetic and potential energy are defined as

$$\langle \mathcal{P}_k \rangle_{xy} = -\langle u_i' u_j' \rangle_{xy} \frac{\partial \langle u_i \rangle_{xy}}{\partial x_j} \tag{5.17}$$

and

$$\langle \mathcal{P}_b \rangle_{xy} = -\frac{1}{N^2} \langle b' u_j' \rangle_{xy} \frac{\partial \langle b \rangle_{xy}}{\partial x_j}, \tag{5.18}$$

respectively. The decomposition also yields the pseudo kinetic and potential energy dissipation rate, which are based on the fluctuations, and are given as

$$\langle \varepsilon'_k \rangle_{xy} = \nu \left\langle \frac{\partial u_i'}{\partial x_j} \frac{\partial u_i'}{\partial x_j} \right\rangle_{xy} \tag{5.19}$$

and

$$\langle \varepsilon'_b \rangle_{xy} = \frac{\alpha}{N^2} \left\langle \frac{\partial b'}{\partial x_j} \frac{\partial b'}{\partial x_j} \right\rangle_{xy} \tag{5.20}$$

respectively. Notice that the above quantities are all functions of the vertical coordinate z and that $\langle \varepsilon'_k \rangle_{xy}$ and $\langle \varepsilon'_b \rangle_{xy}$ are positive quantities, whereas $\langle \mathcal{P}_k \rangle_{xy}$ and

$\langle \mathcal{P}_b \rangle_{xy}$ can assume both positive and negative values. The complete set of equations including all terms that contribute to the evolution of the mean and the fluctuating part can be found in Achatz (2007*b*). We do not include them here, since the other terms do not contribute to the energy exchange between the horizontal mean and the horizontally dependent deviations.

Figures 5.16 and 5.17 shows the production of kinetic and potential energy for cases IGW81 and IGW72 normalized by the corresponding pseudo energy dissipation rate. From Fig. 5.16, we see that in the upper half of the domain, the ratio $\langle \mathcal{P}_k \rangle_{xy} / \langle \varepsilon'_k \rangle_{xy}$ is approximately unity (cf. the zoomed figures). In fact, for the first breaking event of case IGW81 (Fig. 5.16a) the ratio is 1.12 when averaged in the range $1500\,\mathrm{m} < z < 3000\,\mathrm{m}$, while for the last breaking event of case IGW72 (Fig. 5.16d) the averaged ratio in the interval $1500\,\mathrm{m} < z < 2500\,\mathrm{m}$ is 0.97. We do not identify any sign of a local balance between the production and the dissipation of potential energy (Fig. 5.17). Although we only show the results at the first breakdown, similar results are obtained for the other breaking events.

These figures also reveal that the vertical profiles of $\langle \mathcal{P}_k \rangle_{xy}$ and $\langle \mathcal{P}_b \rangle_{xy}$ at the wave breakdown are inhomogeneously distributed in space. The fact that we find both positive as well as negative values of $\langle \mathcal{P}_k \rangle_{xy}$ and $\langle \mathcal{P}_b \rangle_{xy}$ indicates that energy transfers occur from the mean field to the fluctuations, and vice-versa. Specifically for the kinetic energy, we find that $\langle \mathcal{P}_k \rangle_{xy}$ is predominantly positive in the upper half of the numerical domain ($z > 1500\mathrm{m}$). The large ratios of $\langle \mathcal{P}_k \rangle_{xy} / \langle \varepsilon'_k \rangle_{xy}$ observed in Figs. 5.16b and 5.16d are a consequence of the low energy dissipation rate, as already observed in the Hovmöller diagrams in Section 5.3.3.

6

Conclusions

This work has investigated aspects of homogeneous rotating turbulence as well as the breaking behavior of an inertia-gravity wave in the middle atmosphere. To this end, we have employed high-fidelity numerical simulations to explore an yet unvisited part of the physical parameter space. Further studies related to fundamental aspects of turbulence as well as to turbulence modeling will benefit from our results. In the following, we present the main conclusions of the topics covered in this study.

6.1. Homogeneous Rotating Turbulence

In Chapter 3, we investigated through direct numerical simulations the effects of domain size and rotation rate on the energy cascade direction of rotating turbulence. The data here presented adds substantially to previous works, which, in contrast, focused on smaller and shallower domains ($\kappa_f \mathcal{L}_\parallel$ and $\kappa_f \mathcal{L}_\perp < 8$ (Deusebio *et al.*, 2014; Smith *et al.*, 1996)). The presented results, therefore, contribute towards a complete picture of the phase diagram, which unveils the transition from inverse to forward energy cascades through a split energy cascade.

Our results indicate that $\kappa_f \mathcal{L}_\parallel$ is the primary control parameter, provided that Ro_ε is constant and $\kappa_f \mathcal{L}_\perp > 4$. In this scenario, transversal finite-size effects of $\kappa_f \mathcal{L}_\perp$ on the inverse energy transfer ε_{inv} are negligible for our cases with aspect ratio $A_r \geq 1$. For weak rotation with $Ro_\varepsilon \approx 0.31$, transition from a split to a forward cascade was observed at $\kappa_f \mathcal{L}_\parallel \approx 64$. For the strong rotating case, however, although strongly suppressed, a portion of the injected energy ($\varepsilon_{inv} \approx 0.075\,\varepsilon_I$) still cascaded inversely and accumulated at the large scales for $\kappa_f \mathcal{L}_\parallel = 128$.

Results for scaling laws of the energy spectrum are not conclusive, and there is no clear sign of an inertial range over several decades. This is plausible since our initial and isotropic field with $Re_\lambda \approx 68$ does not contain a clear inertial range. In spite of that, the narrow wavenumber region after $\kappa_\perp = \kappa_f$ develops and approaches best a $\kappa_\perp^{-5/2}$ scaling law. Our results also show that, the $\kappa_\perp^{-5/2}$ and $\kappa_\parallel^{-1/2}$ scalings appear at different wavenumber ranges, and that the $\kappa^{-5/2}$ scaling prevails in the 3D energy spectrum, see Fig. 3.8.

In Chapter 4, we investigated the effects of system rotation with Rossby numbers in the range $0.06 \leq Ro_\varepsilon \leq 1.54$ on the evolution of an initial cloud of isotropic eddies.

In contrast to other studies, which have focused on the initial transient immediately after the onset of rotation, we have focused instead on longer time intervals. This was only possible because our DNS were carried out in elongated domains which were 340 times larger than the initial characteristic eddy size.

The classical pictures of rotating turbulence were reproduced, in which we observed the formation of columnar eddies along the axis of rotation and a decrease in the energy dissipation rate. However, by following the evolution of the integral length scales we identified different dynamics that were shown to depend on Ro_ε. This led us to separate our dataset into two groups. While the runs in group R1 did not show any pronounced sign of growth in the integral length scales, for the runs in group R2, $\ell_\parallel$ grew substantially and approximately linearly with time. The latter group of runs can be therefore associated with a regime where the formation of columns predominate, whereas runs of group R1 are closer to homogeneous isotropic turbulence. Furthermore, we found that the growth rate of the columnar eddies in group R2 depends exponentially on Ro_ε, i.e., $\gamma = a \exp(b\, Ro_\varepsilon)$, with $a = 3.90$ and $b = -16.72$.

The energy dissipation rate in the group of runs R1 is well approximated by the scaling law proposed in Baqui & Davidson (2015). For the group R2, which consists of runs at lower Ro_ε, we have shown that the scaling laws currently available in the literature fail to approximate ε_ν. Still, we were able to find a similarity relation for ε_ν in the range $0.06 \leq Ro_\varepsilon \leq 0.31$ by applying the ideas introduced by Kraichnan (1965), in which the spectral transfer time is regarded as composed of two opposing time scales. First, by observing the inverse relation between $\ell_\perp$ and ε_ν, we assumed that $\ell_\perp$ was the relevant length scale to form τ_{nl}. Second, the relaxation time scale τ_3 was shown to depend on a power law of Ro_ε and on τ_{nl}^{iso}, which implies that it is exclusively a function of Ro_ε and of the forcing parameters κ_f and u_f. Thus, we arrived at a similarity law for this Ro_ε range. Scaling ε_ν with $u'^4/(\ell_\perp^2 Ro_\varepsilon^{0.62} \tau_{nl}^{\mathrm{iso}})$ collapsed the data for different Ro_ε into a single curve.

Last, we would like to remark that the results for the case where the rotation rate is highest, i.e., $Ro_\varepsilon = 0.06$, were verified by increasing the numerical resolution and the domain size by a factor of 2 in the direction of rotation. However, whether other dynamics emerge at even lower Ro_ε and the effects of Re_ε remains to be studied. In any case, we hope our numerical investigation contributes to the improvement of turbulence models and stimulates future studies to elucidate and quantify the effects of the Coriolis force on the evolution of a cloud of isotropic eddies in unbounded domains.

6.2. Inertia-Gravity Waves Breaking in the Middle Atmosphere

In Chapter 5, we presented results from fully resolved three-dimensional simulations of a inertia-gravity wave breaking in the middle atmosphere. Two cases were considered, which correspond to two different Reynolds numbers and, accordingly, two different geopotential altitudes.

Both cases IGW81 and IGW72 undergo a sequence of breaking events, which are

marked by a rise in the kinetic energy dissipation rate. The general picture of the wave breakdown is somewhat similar for both Reynolds numbers. Flow field visualization illustrates the outbreak of fine scales of motion in the vertical upper-half of the numerical domain, which are finer in case IGW72 (higher Reynolds number). On the same line, Hovmöller diagrams show that the kinetic energy dissipation rate is more intense in the upper-half of the domain, indicating the dominance of large spatial velocity gradients where the base wave is least stable. The Richardson number can be used as a diagnostic tool to detect these regions.

At the time of wave breakdown, the kinetic energy dissipation rate tensor exhibits an equipartition of dissipation among its individual components, and the vertical kinetic energy spectrum displays a 5/3 scaling for a broad range of wavelengths. At periods in between the breaking events, on the other hand, the kinetic energy dissipation rate tensor is strongly anisotropic, and the vertical kinetic energy spectrum scales with a cubic power law, indicating the relevance of buoyancy effects at these times.

Through an energy budget analysis we saw that the energy transfer mechanism during the wave breakdown is predominantly characterized by energy transfers sustained by pressure field from $\langle uu \rangle_{\mathcal{L}}$ to $\langle ww \rangle_{\mathcal{L}}$, and a subsequent energy conversion into potential energy. The role of the Coriolis force, although less relevant, was also present in shifting energy from $\langle vv \rangle_{\mathcal{L}}$ to $\langle uu \rangle_{\mathcal{L}}$.

Complementing these observations, we also decomposed the velocity and the buoyancy fields into a mean and a fluctuating part. These results shows that the local transfer of kinetic energy between the mean and the fluctuating parts is mainly forward, i.e., from the mean to the fluctuations. In the upper-half of the numerical domain, where fine scales of motion were identified, we found that the pseudo kinetic energy dissipation rate and the kinetic energy production are in roughly in balance during the breaking events.

A

Fictious Forces in a Rotating Frame of Reference

Let F denote a fixed frame of reference and R a frame of reference that rotates with constant velocity around the axis defined by the vector $\mathbf{\Omega}$. In addition to that, let $\hat{\mathbf{e}}_i$ be the unit vectors of the frame F and $\mathbf{g_i}$ of the frame R.

A given vector $\mathbf{c}$ can be then written in any of the reference frames as $\mathbf{c} = c_i\mathbf{e}_i = \tilde{a}_i\mathbf{g_i}$. However, the time derivatives of $\mathbf{c}$ differ because the time derivative of the unit vectors $\mathbf{g}_i$ are different from zero. These derivatives, nevertheless, are connected through the following relation:

$$\frac{\mathrm{d}\mathbf{c}}{\mathrm{d}t} = \frac{\mathrm{d}(c_i\hat{\mathbf{e}}_i)}{\mathrm{d}t} = \frac{\mathrm{d}(\tilde{c}_i\mathbf{g}_i)}{\mathrm{d}t} = \tilde{c}_i\frac{\mathrm{d}\mathbf{g}_i}{\mathrm{d}t} + \frac{\mathrm{d}\tilde{c}_i}{\mathrm{d}t}\mathbf{g}_i. \tag{A.1}$$

In order to evaluate Eq. (A.1), one needs to determine $\mathrm{d}\mathbf{g}_i/\mathrm{d}t$. For that, we first introduce the linear mapping represented by the operator $\mathcal{R}$, which rotates any vector by a given angle θ around an axis with unit vector $\hat{\mathbf{h}}$:

$$\mathcal{R} = \cos(\theta)\mathcal{I} + \sin(\theta)\mathbf{h}^{\times} + (1-\cos(\theta))\hat{\mathbf{h}}\otimes\hat{\mathbf{h}}. \tag{A.2}$$

In the above expression $\mathbf{h}^{\times}$ is the cross product operator, e.g., $\mathbf{h}^{\times}\,\mathbf{c} = \hat{\mathbf{h}}\times\mathbf{c}$. Because the unit vectors $\mathbf{g}_i$ are rotating around the axis defined by $\mathbf{\Omega}$, the linear mapping defined in Eq. (A.2) can be used to determine the unit vectors $\mathbf{g}_i$ at a posteriori time $t+\Delta t$, i.e.,

$$\mathbf{g}_i(t+\Delta t) = \mathcal{R}\mathbf{g}_i(t). \tag{A.3}$$

By definition, $\|\mathbf{\Omega}\| = \Omega = \mathrm{d}\theta/\mathrm{d}t$, which implies that after a relatively small Δt the vectors $\mathbf{g}_i$ have been rotated by an angle $\Delta\theta$. Equation (A.3) can be then written as:

$$\mathbf{g}_i(t+\Delta t) = \cos(\Delta\theta)\mathbf{g}_i(t) + \sin(\Delta\theta)\,(\hat{\mathbf{h}}\times\mathbf{g}_i(t)) + (1-\cos(\Delta\theta))(\hat{\mathbf{h}}\otimes\hat{\mathbf{h}})\mathbf{g}_i(t). \tag{A.4}$$

A

Subtracting $\mathbf{g}_i$ from both sides of Eq. (A.4) and diving by Δt yields

$$\frac{\mathbf{g}_i(t+\Delta t)-\mathbf{g}_i}{\Delta t}=\frac{(\cos(\Delta\theta)-1)}{\Delta t}\mathbf{g}_i(t)+\frac{\sin(\Delta\theta)}{\Delta t}\,(\hat{\mathbf{h}}\times\mathbf{g}_i(t))+\frac{(1-\cos(\Delta\theta))}{\Delta t}(\hat{\mathbf{h}}\otimes\hat{\mathbf{h}})\mathbf{g}_i(t). \quad \text{(A.5)}$$

If we now take the limit $\Delta t\to 0$ in Eq. (A.5) as, we obtain the following relation:

$$\frac{\mathrm{d}\mathbf{g}_i}{\mathrm{d}t}=\Omega\,\hat{\mathbf{h}}\times\mathbf{g}_i=\boldsymbol{\Omega}\times\mathbf{g}_i. \quad \text{(A.6)}$$

Eq. (A.6) is obtained by using L'Hopital's rule, from which follows that the first and the third term of Eq. (A.5) vanish. Now, Eq. (A.1) can be written as:

$$\frac{\mathrm{d}\mathbf{c}}{\mathrm{d}t}=\frac{\mathrm{d}\tilde{c}_i}{\mathrm{d}t}\mathbf{g}_i+\boldsymbol{\Omega}\times(\tilde{c}_i\mathbf{g}_i), \quad \text{(A.7)}$$

and we have an equation that connects the time derivative of a given vector $\mathbf{c}$ between a fixed and a rotating frame of reference.

If $\mathbf{c}$ is taken to be the position vector $\mathbf{r}$, the above relation gives

$$\frac{\mathrm{d}\mathbf{r}}{\mathrm{d}t}=\frac{\mathrm{d}\tilde{r}_i}{\mathrm{d}t}\mathbf{g}_i+\boldsymbol{\Omega}\times(\tilde{r}_i\mathbf{g}_i). \quad \text{(A.8)}$$

Further, introducing $\mathbf{u}_F=\mathrm{d}(r_i\hat{\mathbf{e}}_i)/\mathrm{d}t$ and $\mathbf{u}_R=(\mathrm{d}\tilde{r}_i/\mathrm{d}t)\,\mathbf{g}_i$, we can obtain a relation for the velocity between the fixed and the rotating frame of reference, i.e.,

$$\mathbf{u}_F=\mathbf{u}_R+\boldsymbol{\Omega}\times\mathbf{r}_R. \quad \text{(A.9)}$$

The relation between the acceleration in both frames follows

$$\frac{\mathrm{d}\mathbf{u}_F}{\mathrm{d}t}=\frac{\mathrm{d}}{\mathrm{d}t}(\mathbf{u}_R+\boldsymbol{\Omega}\times\mathbf{r}_R)=\frac{\mathrm{d}}{\mathrm{d}t}\left(\frac{\mathrm{d}\tilde{r}_i}{\mathrm{d}t}\mathbf{g}_i\right)+\boldsymbol{\Omega}\times\frac{\mathrm{d}\mathbf{r}_R}{\mathrm{d}t}. \quad \text{(A.10)}$$

Using Eq. (A.7) and noting that $\mathrm{d}\mathbf{u}_F/\mathrm{d}t=\mathbf{a}_F$ and $\mathrm{d}\mathbf{u}_R/\mathrm{d}t=\mathbf{a}_R$, Eq. (A.10) leads to:

$$\mathbf{a}_F=\mathbf{a}_R+(2\boldsymbol{\Omega}\times\mathbf{u}_R)+\boldsymbol{\Omega}\times(\boldsymbol{\Omega}\times\mathbf{r}_R). \quad \text{(A.11)}$$

B

Inertial Waves: Phase and Group Velocity

Here we briefly present the steps required to obtain the expressions for the phase and group velocity of inertial waves. In a rapidly rotating frame of reference such that the nonlinear forces can be neglected with respect to the Coriolis force, the motion of an incompressible fluid is governed by the linear Navier-Stokes equations. If the viscous effects are also neglected, conservation of linear momentum gives

$$\frac{\partial u_i}{\partial t} + 2\epsilon_{ijk}\Omega_j u_k = -\frac{\partial q}{\partial x_i}, \tag{B.1}$$

and an equation for the vorticity fields follows immediately as:

$$\frac{\partial}{\partial t}\left(\epsilon_{ijk}\frac{\partial u_k}{\partial x_j}\right) = 2\Omega_j \frac{\partial u_i}{\partial x_j} \tag{B.2}$$

Note that Eqs. (B.1) and (B.2) are exactly the same as Eqs. (1.9) and (1.13) and are repeated here in index notation for convenience. Now, applying the operator $\nabla \times (\partial/\partial t)$, i.e.,

$$\left(\nabla \times \frac{\partial}{\partial t}\right)_i = \frac{\partial}{\partial t}\left[\epsilon_{imp}\frac{\partial (\cdot)_p}{\partial x_m}\right], \tag{B.3}$$

to Eq. (B.2) yields the wave-like equation

$$\frac{\partial}{\partial t}\left(\frac{\partial^2 u_i}{\partial x_j \partial x_j}\right) + 4\Omega_p\Omega_j\frac{\partial^2 u_i}{\partial x_p \partial x_j} = 0, \tag{B.4}$$

which can be recast in vector notation as

$$\frac{\partial^2}{\partial t^2}(\nabla^2 \mathbf{u}) + 4\left(\boldsymbol{\Omega}\cdot\nabla\right)^2\mathbf{u} = 0. \tag{B.5}$$

The equation above assumes plane wave solutions of the type

$$\mathbf{u} = \hat{\mathbf{u}}\,\exp[I(\boldsymbol{\kappa}\cdot\mathbf{x} - \sigma t)]. \tag{B.6}$$

By substituting Eq. (B.6) into Eq. (B.5), we can show that the wave frequency must satisfy

$$\sigma^2 \left\|\boldsymbol{\kappa}\right\|^2 = 4(\boldsymbol{\Omega}\cdot\boldsymbol{\kappa})^2, \tag{B.7}$$

and hence

$$\sigma = \pm 2\,\frac{(\boldsymbol{\kappa}\cdot\boldsymbol{\Omega})}{\left\|\boldsymbol{\kappa}\right\|}. \tag{B.8}$$

It follows from the definitions of phase and group velocity that

$$\mathbf{c}_p = \sigma\frac{\boldsymbol{\kappa}}{\left\|\boldsymbol{\kappa}\right\|^2} = \pm 2\,\frac{(\boldsymbol{\kappa}\cdot\boldsymbol{\Omega})}{\left\|\boldsymbol{\kappa}\right\|^3}\boldsymbol{\kappa}, \tag{B.9}$$

and

$$\mathbf{c}_g = \frac{\partial\sigma}{\partial\boldsymbol{\kappa}} = \pm 2\,\frac{\boldsymbol{\kappa}\times(\boldsymbol{\Omega}\times\boldsymbol{\kappa})}{\left\|\boldsymbol{\kappa}\right\|^3}, \tag{B.10}$$

respectively. Eq. (B.10) can be further show to depend on two contributions:

$$\mathbf{c}_g \sim \pm\frac{2}{\left\|\boldsymbol{\kappa}\right\|^3}\left[\boldsymbol{\Omega}\left\|\boldsymbol{\kappa}\right\|^2 - (\boldsymbol{\Omega}\cdot\boldsymbol{\kappa})\boldsymbol{\kappa}\right]. \tag{B.11}$$

Note also that the inertial waves contain a definite helicity. This can be shown by assuming that

$$\boldsymbol{\omega} = \hat{\boldsymbol{\omega}}\exp\left[I(\boldsymbol{\kappa}\cdot\mathbf{x} - \sigma_\omega t)\right], \tag{B.12}$$

where σ_ω is the wave frequency, and enforcing Eq. (B.12) into Eq. (B.2). By doing so, we find that the following relation must be satisfied:

$$\hat{\omega}_i e^{I(\boldsymbol{\kappa}\cdot\mathbf{x}-\sigma_\omega t)}(-\sigma_\omega) = 2(\Omega_j\kappa_j)\hat{u}_i e^{I(\boldsymbol{\kappa}\cdot\mathbf{x}-\sigma t)}, \tag{B.13}$$

from which, with the aid of the relation $\sigma = \pm 2(\Omega_j\kappa_j)/\kappa$, we can show that a possible solution is:

$$\hat{\omega}_i = \mp\left\|\boldsymbol{\kappa}\right\|\hat{u}_i \quad \text{and} \quad \sigma_\omega = \sigma = \pm\frac{2(\boldsymbol{\Omega}\cdot\boldsymbol{\kappa})}{\left\|\boldsymbol{\kappa}\right\|}. \tag{B.14}$$

Therefore, the vorticity and the velocity field are in phase and the helicity is maximum. Waves with positive helicity carry energy in the negative $\mathbf{c}_g$ direction and vice-versa.

B.1. Eigendecomposition of the Curl Operator

In the wavenumber domain, the curl operator can be written in matrix form as

$$\begin{pmatrix} 0 & -\kappa_3 & \kappa_2 \\ \kappa_3 & 0 & -\kappa_1 \\ -\kappa_2 & \kappa_1 & 0 \end{pmatrix}.$$

to make the exponentials match in Eq. (B.13), σ_ω must equal σ.

The mode matrices used to diagonalize the curl operator are constructed from its eigenvectors and read

$$\mathcal{Q} = \frac{1}{\xi}\begin{pmatrix} (\kappa_2^2+\kappa_3^2) & (\kappa_2^2+\kappa_3^2) & [2\kappa_1^2(\kappa_2^2+\kappa_3^2)]^{1/2} \\ (-\kappa_1\kappa_2 - I\left\|\boldsymbol{\kappa}\right\|\kappa_3) & (-\kappa_1\kappa_2 + I\left\|\boldsymbol{\kappa}\right\|\kappa_3) & [2\kappa_2^2(\kappa_2^2+\kappa_3^2)]^{1/2} \\ (-\kappa_1\kappa_3 + I\left\|\boldsymbol{\kappa}\right\|\kappa_2) & (-\kappa_1\kappa_3 - I\left\|\boldsymbol{\kappa}\right\|\kappa_2) & [2\kappa_3^2(\kappa_2^2+\kappa_3^2)]^{1/2} \end{pmatrix}$$

and

$$\mathcal{Q}^{-1} = \frac{1}{\xi}\begin{pmatrix} (\kappa_2^2+\kappa_3^2) & (-\kappa_1\kappa_2 + I\left\|\boldsymbol{\kappa}\right\|\kappa_3) & (-\kappa_1\kappa_3 - I\left\|\boldsymbol{\kappa}\right\|\kappa_2) \\ (\kappa_2^2+\kappa_3^2) & (-\kappa_1\kappa_2 - I\left\|\boldsymbol{\kappa}\right\|\kappa_3) & (-\kappa_1\kappa_3 + I\left\|\boldsymbol{\kappa}\right\|\kappa_2) \\ [2\kappa_1^2(\kappa_2^2+\kappa_3^2)]^{1/2} & [2\kappa_2^2(\kappa_2^2+\kappa_3^2)]^{1/2} & [2\kappa_3^2(\kappa_2^2+\kappa_3^2)]^{1/2} \end{pmatrix},$$

where $\xi = [2\left\|\boldsymbol{\kappa}\right\|^2(\kappa_2^2+\kappa_3^2)]^{1/2}$.

C

The Pseudospectral Method in Short

Spectral method is a numerical technique employed to approximate the solution of partial differential equations. The basic idea consists in approximating a desired field by expanding it in terms of orthogonal basis functions, and seeking for the coefficients of the expansion. Because we will deal exclusively with homogeneous flows, we will consider only basis functions that are trigonometric polynomials, i.e., we restrict ourselves to Fourier series representations. A much deeper discussion on spectral methods is given in Canuto *et al.* (2006*a*,*b*); Karniadakis & Sherwin (2005). Here, our aim is only to highlight the most important steps taken when converting a partial differential equation into an dynamical equation. To illustrate the inner-workings of spectral methods, let us restrict ourselves to the Burgers' equations. Although the Burgers' equation is one-dimensional, it shares similarities with the full Navier-Stokes equations, as it degenerates from the former.

Consider an arbitrary field $u(x_1)$, not necessarily the velocity field, which evolves in time according to

$$\frac{\partial u}{\partial t} + u\frac{\partial u}{\partial x_1} = 0. \tag{C.1}$$

Further, let us assume that the initial condition $u(x_1, t = 0)$ is known and that Eq. (C.1) is valid on the periodic domain $\mathcal{L}_1 = [0, 2\pi]$; the subscript in x_1 denotes the first and only Cartesian direction. The basic idea is to find an approximated solution u^N, which is written as a series expansion. In our case, in form of a truncated Fourier series, i.e.,

$$u^N(x_1, t) = \sum_{\kappa=-N_1/2}^{N_1/2-1} \hat{u}(\kappa_1, t)\, e^{I\kappa_1 x_1}, \tag{C.2}$$

where N_1 is the number of degrees of freedom, $\hat{u}_{\kappa_1}$ are the Fourier coefficients, I is the unity imaginary number, $\phi_{\kappa_1} = e^{I\kappa_1 x}$ are the basis functions and κ_1 are the wavenumbers. Because Eq. (C.2) is just an approximation to the true solution, we can not expect it to satisfy Eq. (C.1) exactly for a given set of coefficients. The

measure of the error in approximating u by u^N can be computed by defining a residual function in connection with Eq. (C.2):

$$R(x_1,t) = \frac{\partial u^N}{\partial t} + u^N \frac{\partial u^N}{\partial x}, \tag{C.3}$$

which obviously returns null if $u = u^N$.

The idea now is to find relations for the coefficients of the expansion by imposing a weak condition to $R(x_1,t)$ with the aid of trial functions ψ_p, such that the integral of the weighted residual over the entire domain is zero:

$$\int_{\mathcal{L}_1} R(u_1^N)\psi_p \,\mathrm{d}x_1 = 0. \tag{C.4}$$

Although we are free to choose the trial functions, some specific choices turns out to be more convenient. For instance, a straightforward choice, typical of Fourier-Galerkin methods, is to pick trial functions that are polynomials orthogonal to the basis functions, i.e., $\psi_{\kappa'} = (1/2\pi)e^{-I\kappa_1' x_1}$. Hence Eq. (C.4) becomes

$$\frac{1}{2\pi}\int_{\mathcal{L}_1}\left[\frac{\partial u^N}{\partial t} + u^N\frac{\partial u^N}{\partial x_1}\right] e^{-I\kappa_1' x_1}\,\mathrm{d}x_1 = 0. \tag{C.5}$$

Using the orthogonality relation between trial and test functions, i.e.,

$$\int_{\mathcal{L}_1}\phi_{\kappa_1}(x_1)\,\psi_{\kappa_1'}(x_1)\,\mathrm{d}x_1 = \frac{1}{2\pi}\int_{\mathcal{L}_1} e^{I\kappa_1 x_1}e^{-I\kappa_1' x_1}\,\mathrm{d}x_1 = \delta_{\kappa_1,\kappa_1'}\,, \tag{C.6}$$

where $\delta_{\kappa_1,\kappa_1'}$ is the Kronecker's delta, Eq. (C.5) is converted into an ordinary differential equation for the coefficients of the expansion.

$$\frac{\mathrm{d}\hat{u}_1(\kappa_1)}{\mathrm{d}t} + \sum_{\kappa_1'+\kappa_1''=\kappa_1}\hat{u_1}(\kappa_1')\hat{v}(\kappa_1'') = 0. \tag{C.7}$$

In the equation above, $\hat{v}$ are the Fourier coefficients of $\partial u^N/\partial x_1$, and their relation to $\hat{u}$ can be obtained from differentiation of Eq. (C.2). Given the initial conditions, we can integrate Eq. (C.7) in time, and posteriorly use the coefficients in Eq. (C.2) to yield the approximate solution for any (x_1,t). Note however that Eq. (C.7) contains a summation term on its left-hand-side. This term represents a convolution sum and it appears due to the nonlinear character of Eq. (C.1), i.e., due to $u(\partial u/\partial x_1)$.

If we think of developing a computational code to numerically solve Eq. (C.7), we will note that the convolution sum requires a large number of operations to be evaluated. In fact, the number of operations is proportional to the square of the number of degrees of freedom. This number can easily become large, especially if we plan to consider three-dimensional problems; in such cases the number of degrees of freedom are already of the order of N^3. Nevertheless, this cost can be remedied if we use the pseudospectral method as introduced by Orszag (1969).

The pseudospectral method consists of first transforming $\hat{u}$ and $\hat{v}$ in to the wavenumber domain using the Discrete Fourier Transform (DFT) back to physical

space. Then, building the product $s = uv = u(\partial u/\partial x_1)$ in physical space, and subsequently transforming $s(x_1)$ to Fourier space to obtain $\hat{s}(\kappa_1)$. Such procedure is cheaper since the number of operations required to compute the DFTs scale $N \log_2 N$ instead of N^2 as required by the convolution sum. The reduction in the number of operations however comes at a cost, and this approach is not "clean", in the sense that it leads to an equation which is slightly different than Eq. (C.7):

$$\frac{\mathrm{d}\hat{u}(\kappa)}{\mathrm{d}t} + \underbrace{\sum_{\kappa'+\kappa''=\kappa} \hat{u}(\kappa')\hat{v}(\kappa'')}_{\hat{s}(\kappa_1)} + \underbrace{\sum_{\kappa'+\kappa''=\kappa\pm N} \hat{u}(\kappa')\hat{v}(\kappa'')}_{\text{aliasing errors}} = 0. \tag{C.8}$$

When comparing Eq. (C.7) with Eq. (C.8), we note that an extra summation term is present on the left-hand-side. While the Fourier-Galerkin approximates the real solution and introduces only truncation errors (Eq. (C.7)), the pseudospectral method includes aliasing errors in addition to the truncation errors. (Eq. (C.8)).

Several techniques for removing aliasing errors (de-aliasing techniques) are present in the literature, e.g., the 3/2 rule and the technique of shifted grids. If applied together with the pseudospectral method, these techniques lead to a formulation that is equivalent to the one obtained by the Fourier-Galerkin approximation. That is, Eq. (C.8) becomes equivalent to Eq. (C.7).

Among other properties of spectral methods, spectral convergence is maybe the most attractive. Spectral convergence means that convergence to the exact solution is faster than any finite power of $1/N$. For this reason, spectral methods are commonly chosen for simulating turbulent homogeneous flows where every scale of motion needs to be resolved. The use of spectral methods can reduce the number of required degrees of freedom, if compared to the resolution required by classical methods such as finite-differences or finite-volumes.

D

Exact Integrating Factor

In this appendix, we refresh the idea behind the exact integrating factor technique. As an example, we consider the one-dimensional ODE:

$$\frac{\mathrm{d}u}{\mathrm{d}t} + f(t)u = G(u), \tag{D.1}$$

where t denotes time, u is a given variable (not necessarily the velocity), and $f(t)$ and $G(u)$ are two arbitrary functions.

The objective is to find a function, say $M(t)$, such that the linear term $f(t)u$ and the temporal derivative can be brought together into a single operator, i.e., we want a $M(t)$ that allows us to rewrite Eq. (D.1) as:

$$\frac{\mathrm{d}(uM(t))}{\mathrm{d}t} = M(t)G(u). \tag{D.2}$$

Following Boyce *et al.* (2017), this can be achieved by first multipling Eq. (D.1) by $M(t)$, i.e.,

$$M(t)\frac{\mathrm{d}u}{\mathrm{d}t} + M(t)f(t)u = M(t)G(u), \tag{D.3}$$

and equating the left-hand-sides of Eq. (D.2) and Eq. (D.3). This step leads to

$$M(t)\frac{\mathrm{d}u}{\mathrm{d}t} + u\frac{\mathrm{d}M}{\mathrm{d}t} = M(t)\frac{\mathrm{d}u}{\mathrm{d}t} + M(t)f(t)u \tag{D.4}$$

$$u\frac{\mathrm{d}M}{\mathrm{d}t} = M(t)f(t)u \tag{D.5}$$

$$0 = u\left(\frac{\mathrm{d}M}{\mathrm{d}t} - M(t)f(t)\right), \tag{D.6}$$

from which follows that the term inside the parenthesis in Eq. (D.6) is zero and that, apart from an additive constant,

$$M(t) = \exp\left(\int f(\tau)\,\mathrm{d}\tau\right). \tag{D.7}$$

Thus Eq. (D.1) is analagous to

$$\frac{\mathrm{d}}{\mathrm{d}t}\left(ue^{\int f(\tau)\,\mathrm{d}\tau}\right) = e^{\int f(\tau)\,\mathrm{d}\tau}G(u). \tag{D.8}$$

E

How to Combine the Effects of Rotation

Here, we show how the two terms that stems from the Coriolis effects can be brought together. These terms appear in the Navier-Stokes when written in the wavenumber domain. In particular, we made reference to these terms in Eq. (2.10), and we repeat them here for convenience:

$$\left[2\epsilon_{ijk}\Omega_j\hat{u}_k - 2\frac{\kappa_i\kappa_m}{\|\boldsymbol{\kappa}\|^2}\epsilon_{mjk}\Omega_j\hat{u}_k\right]. \tag{E.1}$$

First, let us introduce the vector $\mathbf{n} = \boldsymbol{\kappa}/\|\boldsymbol{\kappa}\|$ which allows us to rewrite the first term involving the angular velocity as

$$2\epsilon_{ijk}\Omega_j\hat{u}_k = 2\epsilon_{ijk}\Omega_j\hat{u}_k n_p n_p, \tag{E.2}$$

since the norm of $\mathbf{n}$ is unity. Furthermore, by using the fact that the velocity field is solenoidal, i.e., $\kappa_p\hat{u}_p = n_p\hat{u}_p = 0$, it can be shown that

$$\begin{aligned} 2\epsilon_{ijk}\Omega_j\hat{u}_k n_p n_p &= 2\epsilon_{ijk}\Omega_j\hat{u}_k n_p n_p - 2\epsilon_{ijk}\Omega_j n_k\hat{u}_p n_p && \text{(E.3)}\\ &= 2\epsilon_{ijk}\Omega_j(\hat{u}_k n_p - n_k\hat{u}_p)n_p && \text{(E.4)}\\ &= 2\epsilon_{ijk}\Omega_j(\epsilon_{mlq}\hat{u}_l n_q\epsilon_{mkp})n_p, && \text{(E.5)} \end{aligned}$$

in which we made use of $\epsilon_{mkp}\hat{u}_k n_p\epsilon_{mlq} = (\delta_{kl}\delta_{pq} - \delta_{kq}\delta_{pl})\hat{u}_k n_p$. Continuing from Eq. (E.5) and expanding the product of the permutation symbols, we obtain:

$$\begin{aligned} 2\epsilon_{ijk}\Omega_j\hat{u}_k n_p n_p &= 2(\delta_{ip}\delta_{jm} - \delta_{im}\delta_{jp})(\epsilon_{mlq}\Omega_j n_p\hat{l} n_q) && \text{(E.6)}\\ &= 2n_i\epsilon_{jlq}\Omega_j n_q\hat{u}_l - 2\epsilon_{ilq}\Omega_p n_p\hat{u}_l n_q && \text{(E.7)}\\ &= 2n_i n_q\epsilon_{qjl}\Omega_j\hat{u}_l + 2\Omega_p n_p\epsilon_{iql}\hat{u}_l n_q. && \text{(E.8)} \end{aligned}$$

Now, combining Eqs. (E.2) and (E.8) we obtain

$$\left[2\epsilon_{ijk}\Omega_j\hat{u}_k - 2\frac{\kappa_i\kappa_m}{\|\boldsymbol{\kappa}\|^2}\epsilon_{mjk}\Omega_j\hat{u}_k\right] = 2n_i n_q\epsilon_{qjl}\Omega_j\hat{u}_l + 2\Omega_p n_p\epsilon_{iql}\hat{u}_l n_q - 2n_i n_m\epsilon_{mjk}\Omega_j\hat{u}_k \tag{E.9}$$

and finally

$$\left[2\epsilon_{ijk}\Omega_j\hat{u}_k - 2\frac{\kappa_i\kappa_m}{\|\boldsymbol{\kappa}\|^2}\epsilon_{mjk}\Omega_j\hat{u}_k\right] = 2\Omega_p n_p \epsilon_{iql}\hat{u}_l n_q. \tag{E.10}$$

Bibliography

Achatz, U. 2005 On the role of optimal perturbations in the instability of monochromatic gravity waves. *Physics of Fluids* **17** (9), 094107.

Achatz, U. 2007*a* Modal and Nonmodal Perturbations of Monochromatic High-Frequency Gravity Waves: Primary Nonlinear Dynamics. *Journal of the Atmospheric Sciences* **64** (6), 1977–1994.

Achatz, U. 2007*b* The Primary Nonlinear Dynamics of Modal and Nonmodal Perturbations of Monochromatic Inertia–Gravity Waves. *Journal of the Atmospheric Sciences* **64** (1), 74–95.

Achatz, U. & Schmitz, G. 2006 Shear and Static Instability of Inertia–Gravity Wave Packets: Short-Term Modal and Nonmodal Growth. *Journal of the Atmospheric Sciences* **63** (2), 397–413.

Alexakis, A. & Biferale, L. 2018 Cascades and transitions in turbulent flows. *Physics Reports* **767-769**, 1–101.

Alvelius, K. 1999 Random forcing of three-dimensional homogeneous turbulence. *Physics of Fluids* **11** (7), 1880.

Andreassen, Ø., Wasberg, C. E., Fritts, D. C. & Isler, J. R. 1994 Gravity wave breaking in two and three dimensions: 1. Model description and comparison of two-dimensional evolutions. *Journal of Geophysical Research* **99** (D4), 8095.

Baqui, Y. B. & Davidson, P. A. 2015 A phenomenological theory of rotating turbulence. *Physics of Fluids* **27** (2), 025107.

Bardina, J., Ferziger, J. H. & Rogallo, R. S. 1985 Effect of rotation on isotropic turbulence: computation and modelling. *Journal of Fluid Mechanics* **154**, 321–336.

Bartello, P., Métais, O. & Lesieur, M. 1994 Coherent structures in rotating three-dimensional turbulence. *Journal of Fluid Mechanics* **273**, 1–29.

Batchelor, G. K. 1953 *The Theory of Homogeneous Turbulence*. Cambridge University Press.

Bauer, P., Thorpe, A. & Brunet, G. 2015 The quiet revolution of numerical weather prediction. *Nature* **525** (7567), 47–55.

Benavides, S. J. & Alexakis, A. 2017 Critical transitions in thin layer turbulence. *Journal of Fluid Mechanics* **822**, 364–385.

Berner, J., Achatz, U., Batté, L., Bengtsson, L., Cámara, A. d. l., Christensen, H. M., Colangeli, M., Coleman, D. R. B., Crommelin, D., Dolaptchiev, S. I., Franzke, C. L. E., Friederichs, P., Imkeller, P., Järvinen, H., Juricke, S., Kitsios, V., Lott, F., Lucarini, V., Mahajan, S., Palmer, T. N., Penland, C., Sakradzija, M., von Storch, J.-S., Weisheimer, A., Weniger, M., Williams, P. D. & Yano, J.-I. 2017 Stochastic Parameterization: Toward a New View of Weather and Climate Models. *Bulletin of the American Meteorological Society* **98** (3), 565–588.

Boffetta, G. & Ecke, R. E. 2012 Two-Dimensional Turbulence. *Annual Review of Fluid Mechanics* **44** (1), 427–451.

van Bokhoven, L. J. A., Clercx, H. J. H., van Heijst, G. J. F. & Trieling, R. R. 2009 Experiments on rapidly rotating turbulent flows. *Physics of Fluids* **21** (9), 096601.

Boyce, W. E., DiPrima, R. C. & Meade, D. B. 2017 *Elementary Differential Equations and Boundary Value Problems*. John Wiley & Sons.

Boyd, J. P. 2001 *Chebyshev and Fourier Spectral Methods*, 2nd edn. Dover Publications.

Brethouwer, G., Billant, P., Lindborg, E. & Chomaz, J.-M. 2007 Scaling analysis and simulation of strongly stratified turbulent flows. *Journal of Fluid Mechanics* **585**, 343–368.

Buzzicotti, M., Aluie, H., Biferale, L. & Linkmann, M. 2018 Energy transfer in turbulence under rotation. *Physical Review Fluids* **3** (3), 034802.

Cambon, C. & Jacquin, L. 1989 Spectral approach to non-isotropic turbulence subjected to rotation. *Journal of Fluid Mechanics* **202**, 295–295.

Cambon, C., Mansour, N. N. & Godeferd, F. S. 1997 Energy transfer in rotating turbulence. *Journal of Fluid Mechanics* **337**, 303–332.

Canuto, C., Hussaini, M. Y., Quarteroni, A. & Zang, T. A. 2006*a* *Spectral Methods: Evolution to Complex Geometries and Applications to Fluid Dynamics*. Springer-Verlag Berlin Heidelberg.

Canuto, C., Hussaini, M. Y., Quarteroni, A. & Zang, T. A. 2006*b* *Spectral Methods: Fundamentals in Single Domains*. Springer-Verlag Berlin Heidelberg.

Cardesa, J. I., Vela-Martín, A. & Jiménez, J. 2017 The turbulent cascade in five dimensions. *Science* **357** (6353), 782–784.

Celani, A., Musacchio, S. & Vincenzi, D. 2010 Turbulence in More than Two and Less than Three Dimensions. *Physical Review Letters* **104** (18), 184506.

Chouippe, A. & Uhlmann, M. 2015 Forcing homogeneous turbulence in direct numerical simulation of particulate flow with interface resolution and gravity. *Physics of Fluids* **27** (12), 123301.

Comte-Bellot, G. & Corrsin, S. 1971 Simple Eulerian time correlation of full- and narrow-band velocity signals in grid-generated, 'isotropic' turbulence. *Journal of Fluid Mechanics* **48**, 273–337.

Dallas, V., Fauve, S. & Alexakis, A. 2015 Statistical Equilibria of Large Scales in Dissipative Hydrodynamic Turbulence. *Physical Review Letters* **115** (20), 204501.

Davidson, P. A., Kaneda, Y., Moffatt, K. & Sreenivasan, K. R. 2011 *A Voyage Through Turbulence*. Cambridge University Press.

Davidson, P. A., Kaneda, Y. & Sreenivasan, K. R. 2013 *Ten Chapters in Turbulence*. Cambridge University Press.

Davidson, P. A., Staplehurst, P. J. & Dalziel, S. B. 2006 On the evolution of eddies in a rapidly rotating system. *Journal of Fluid Mechanics* **557**, 135–144.

Delache, A., Cambon, C. & Godeferd, F. 2014 Scale by scale anisotropy in freely decaying rotating turbulence. *Physics of Fluids* **26**, 025104.

Deusebio, E., Boffetta, G., Lindborg, E. & Musacchio, S. 2014 Dimensional transition in rotating turbulence. *Physical Review E* **90** (2), 023005.

Dugas, R. 2012 *A History of Mechanics*. Dover Publications.

Eswaran, V. & Pope, S. 1988 An examination of forcing in direct numerical simulations of turbulence. *Computers & Fluids* **16** (3), 257–278.

Ferziger, J. H. & Perić, M. 2002 *Computational Methods for Fluid Dynamics*. Springer-Verlag Berlin Heidelberg.

Frisch, U. 1995 *Turbulence: The Legacy of A. N. Kolmogorov*. Cambridge University Press.

Fritts, D. C., Isler, J. R. & Andreassen, Ø. 1994 Gravity wave breaking in two and three dimensions: 2. Three-dimensional evolution and instability structure. *Journal of Geophysical Research* **99** (D4), 8109.

Fritts, D. C. & Wang, L. 2013 Gravity Wave–Fine Structure Interactions. Part II: Energy Dissipation Evolutions, Statistics, and Implications. *Journal of the Atmospheric Sciences* **70** (12), 3735–3755.

Fritts, D. C., Wang, L., Werne, J., Lund, T. & Wan, K. 2009*a* Gravity Wave Instability Dynamics at High Reynolds Numbers. Part I: Wave Field Evolution at Large Amplitudes and High Frequencies. *Journal of the Atmospheric Sciences* **66** (5), 1126–1148.

Fritts, D. C., Wang, L., Werne, J., Lund, T. & Wan, K. 2009*b* Gravity Wave Instability Dynamics at High Reynolds Numbers. Part II: Turbulence Evolution, Structure, and Anisotropy. *Journal of the Atmospheric Sciences* **66** (5), 1149–1171.

Fritts, D. C., Wang, L. & Werne, J. A. 2013 Gravity Wave–Fine Structure Interactions. Part I: Influences of Fine Structure Form and Orientation on Flow Evolution and Instability. *Journal of the Atmospheric Sciences* **70** (12), 3710–3734.

Fruman, M. D. & Achatz, U. 2012 Secondary Instabilities in Breaking Inertia–Gravity Waves. *Journal of the Atmospheric Sciences* **69** (1), 303–322.

Fruman, M. D., Remmler, S., Achatz, U. & Hickel, S. 2014 On the construction of a direct numerical simulation of a breaking inertia-gravity wave in the upper mesosphere. *Journal of Geophysical Research* **119** (20), 11613–11640.

Gaensler, B. M., Haverkorn, M., Burkhart, B., Newton–McGee, K. J., Ekers, R. D., Lazarian, A., McClure–Griffiths, N. M., Robishaw, T., Dickey, J. M. & Green, A. J. 2011 Low-Mach-number turbulence in interstellar gas revealed by radio polarization gradients. *Nature* **478** (7368), 214–217.

Galtier, S. 2003 Weak inertial-wave turbulence theory. *Physical Review E* **68** (1), 015301(R).

Godeferd, F. S. & Moisy, F. 2015 Structure and Dynamics of Rotating Turbulence: A Review of Recent Experimental and Numerical Results. *Applied Mechanics Reviews* **67** (3), 030802.

Greenspan, H. P. 1968 *The Theory of Rotating Fluids*. Cambridge University Press.

Hickel, S., Adams, N. A. & Domaradzki, J. A. 2006 An adaptive local deconvolution method for implicit LES. *Journal of Computational Physics* **213** (1), 413–436.

Hines, C. O. 1997 Doppler-spread parameterization of gravity-wave momentum deposition in the middle atmosphere. Part 1: Basic formulation. *Journal of Atmospheric and Solar-Terrestrial Physics* **59** (4), 371–386.

Hopfinger, E. J., Browand, F. K. & Gagne, Y. 1982 Turbulence and waves in a rotating tank. *Journal of Fluid Mechanics* **125**, 505–534.

Hunt, J. C. R., Wray, A. A. & Moin, P. 1988 Eddies, streams, and convergence zones in turbulent flows. In *Proceedings of the Summer Program (Center for Turbulence Research)*, pp. 193–208.

Ibbetson, a. & Tritton, D. J. 1975 Experiments on turbulence in a rotating fluid. *Journal of Fluid Mechanics* **68**, 639–672.

Ishihara, T., Gotoh, T. & Kaneda, Y. 2009 Study of High–Reynolds Number Isotropic Turbulence by Direct Numerical Simulation. *Annual Review of Fluid Mechanics* **41** (1), 165–180.

Isler, J. R., Fritts, D. C., Andreassen, Ø. & Wasberg, C. E. 1994 Gravity wave breaking in two and three dimensions: 3. Vortex breakdown and transition

to isotropy. *Journal of Geophysical Research* **99** (D4), 8125.

Jacquin, L., Leuchter, O., Cambon, C. & Mathieu, J. 1990 Homogeneous turbulence in the presence of rotation. *Journal of Fluid Mechanics* **220**, 1–52.

Jiménez, J., Wray, A. A., Saffman, P. G. & Rogallo, R. S. 1993 The structure of intense vorticity in isotropic turbulence. *Journal of Fluid Mechanics* **255**, 65–90.

Kaneda, Y., Ishihara, T., Yokokawa, M., Itakura, K. & Uno, A. 2003 Energy dissipation rate and energy spectrum in high resolution direct numerical simulations of turbulence in a periodic box. *Physics of Fluids* **15** (2), L21.

Karniadakis, G. E. & Sherwin, S. J. 2005 *Spectral/hp Element Methods for Computational Fluid Dynamics: Second Edition*. Oxford University Press.

Kraichnan, R. H. 1965 Inertial-Range Spectrum of Hydromagnetic Turbulence. *Physics of Fluids* **8** (7), 1385.

Landau, L. D. & Lifshitz, E. M. 1959 *Fluid Mechanics*. Pergamon Press.

Lindzen, R. S. 1981 Turbulence and stress owing to gravity wave and tidal breakdown. *Journal of Geophysical Research* **86** (C10), 9707.

Linkmann, M. & Dallas, V. 2017 Triad interactions and the bidirectional turbulent cascade of magnetic helicity. *Physical Review Fluids* **2** (5), 1–17.

Matthaeus, W. H. & Zhou, Y. 1989 Extended inertial range phenomenology of magnetohydrodynamic turbulence. *Physics of Fluids B* **1** (9), 1929.

Miller, V., Tilghman, M. & Hanson, R. 2014 The Hidden Complexities of the Simple Match. *APS Gallery of Fluid Motion* **V0012**.

Mininni, P. D., Alexakis, A. & Pouquet, A. 2009 Scale interactions and scaling laws in rotating flows at moderate Rossby numbers and large Reynolds numbers. *Physics of Fluids* **21** (1), 015108.

Mininni, P. D., Rosenberg, D. & Pouquet, A. 2012 Isotropization at small scales of rotating helically driven turbulence. *Journal of Fluid Mechanics* **699**, 263–279.

Moffatt, H. K. 2014 Note on the triad interactions of homogeneous turbulence. *Journal of Fluid Mechanics* **741**, R3.

Mohanan, A. V., Bonamy, C. & Augier, P. 2019 FluidFFT: Common API (C++ and Python) for Fast Fourier Transform HPC Libraries. *Journal of Open Research Software* **7**, 10.

Moisy, F., Morize, C., Rabaud, M. & Sommeria, J. 2011 Decay laws, anisotropy and cyclone-anticyclone asymmetry in decaying rotating turbulence. *Journal of Fluid Mechanics* **666**, 5–35.

Morinishi, Y., Nakabayashi, K. & Ren, S. Q. 2001 New DNS algorithm for

rotating homogeneous decaying turbulence. *International Journal of Heat and Fluid Flow* **22** (1), 30–38.

Nazarenko, S. 2011 *Wave Turbulence*. Springer Berlin Heidelberg.

Nazarenko, S. V. & Schekochihin, A. A. 2011 Critical balance in magneto-hydrodynamic, rotating and stratified turbulence: towards a universal scaling conjecture. *Journal of Fluid Mechanics* **677**, 134–153.

Orszag, S. A. 1969 Numerical Methods for the Simulation of Turbulence. *Physics of Fluids* **12** (12), II–250.

Orszag, S. A. & Patterson, G. S. 1972 Numerical Simulation of Three-Dimensional Homogeneous Isotropic Turbulence. *Physical Review Letters* **28** (2), 76–79.

Pekurovsky, D. 2012 P3DFFT: A Framework for Parallel Computations of Fourier Transforms in Three Dimensions. *SIAM Journal on Scientific Computing* **34** (4), C192–C209.

Pestana, T. & Hickel, S. 2019*a* Direct Numerical Simulations of Forced Homogeneous Rotating Turbulence in Vertically Extended Domains. *4TU.Centre for Research Data* **Dataset**.

Pestana, T. & Hickel, S. 2019*b* Regime transition in the energy cascade of rotating turbulence. *Physical Review E* **99** (5), 053103.

Pope, S. B. 2000 *Turbulent Flows*. Cambridge University Press.

Proudman, J. 1916 On the Motion of Solids in a Liquid Possessing Vorticity. *Proceedings of the Royal Society of London* **92** (642), 408–424.

Remmler, S., Fruman, M. D. & Hickel, S. 2013 Direct numerical simulation of a breaking inertia-gravity wave. *Journal of Fluid Mechanics* **722** (2013), 424–436.

Remmler, S. & Hickel, S. 2013 Spectral structure of stratified turbulence: direct numerical simulations and predictions by large eddy simulation. *Theoretical and Computational Fluid Dynamics* **27**, 319–336.

Remmler, S., Hickel, S., Fruman, M. D. & Achatz, U. 2015 Validation of Large-Eddy Simulation Methods for Gravity Wave Breaking. *Journal of the Atmospheric Sciences* **72** (9), 3537–3562.

Reynolds, O. 1883 An Experimental Investigation of the Circumstances Which Determine Whether the Motion of Water Shall Be Direct or Sinuous, and of the Law of Resistance in Parallel Channels. *Philosophical Transactions of the Royal Society of London* **174**, 935–982.

Rogallo, R. S. 1977 An ILLIAC program for the numerical simulation of homogeneous incompressible turbulence. Technical Memo 73. NASA.

S. C. Dickinson, R. L. 1982 Oscillating-grid turbulence including effects of rota-

tion. *Journal of Fluid Mechanics* **126**, 315–333.

Sagaut, P. & Cambon, C. 2018 *Homogeneous Turbulence Dynamics*, 2nd edn. Springer International Publishing.

Seshasayanan, K. & Alexakis, A. 2018 Condensates in rotating turbulent flows. *Journal of Fluid Mechanics* **841**, 434–462.

Smith, L. & Waleffe, F. 1999 Transfer of energy to two-dimensional large scales in forced, rotating three-dimensional turbulence. *Physics of Fluids* **11** (6), 1608.

Smith, L. M., Chasnov, J. R. & Waleffe, F. 1996 Crossover from Two- to Three-Dimensional Turbulence. *Physical Review Letters* **77** (12), 2467–2470.

Staplehurst, P. J., Davidson, P. A. & Dalziel, S. B. 2008 Structure formation in homogeneous freely decaying rotating turbulence. *Journal of Fluid Mechanics* **598**, 81–105.

Tang, S. L., Antonia, R. A., Djenidi, L., Danaila, L. & Zhou, Y. 2018 Reappraisal of the velocity derivative flatness factor in various turbulent flows. *Journal of Fluid Mechanics* **847**, 244–265.

Taylor, G. 1921 Experiments with Rotating Fluids. *Proceedings of the Royal Society of London* **100** (703), 114–121.

Tolstov, G. & Silverman, R. 1976 *Fourier Series*. Dover Publications.

Valente, P. C. & Dallas, V. 2017 Spectral imbalance in the inertial range dynamics of decaying rotating turbulence. *Physical Review E* **95**, 023114.

Van Atta, C. W. & Antonia, R. A. 1980 Reynolds number dependence of skewness and flatness factors of turbulent velocity derivatives. *Physics of Fluids* **23** (2), 252.

Waleffe, F. 1993 Inertial transfers in the helical decomposition. *Physics of Fluids* **5**, 677.

Yau, K.-H., Klaassen, G. P. & Sonmor, L. J. 2004 Principal instabilities of large amplitude inertio-gravity waves. *Physics of Fluids* **16** (4), 936–951.

Yeung, P. K. & Zhou, Y. 1998 Numerical study of rotating turbulence with external forcing. *Physics of Fluids* **10** (11), 2895.

Yoshimatsu, K., Midorikawa, M. & Kaneda, Y. 2011 Columnar eddy formation in freely decaying homogeneous rotating turbulence. *Journal of Fluid Mechanics* **677**, 154–178.

Zeman, O. 1994 A note on the spectra and decay of rotating homogeneous turbulence. *Physics of Fluids* **6** (10), 3221.

Zhou, Y. 1995 A phenomenological treatment of rotating turbulence. *Physics of Fluids* **7** (8), 2092.

Afterword

The final form of this book is a product of my explorations in the past four and a half years, and of the influence I have had from colleagues, friends and family. I have often said that the downside of living in Delft is the fact that nearly everybody in the city is somehow linked to the University, which makes it hard for one to disconnect from work. In hindsight, I must admit that the upside is that it allowed me to be part of a diverse and unique community from which I could learn a great deal. I would like to use this space to thank some of the people who have contributed to this journey. Please forgive me already in advance for any memory lapse.

I would like to start by expressing my genuine gratitude to my promotor Prof. Hickel for the close supervision and assistance in these past years. Your eye for details inspired my research and it was a pleasure to work under your guidance. During this time you were not only a supervisor but also a friend. The moments we shared outside the working environment will always be remembered. My thanks are also naturally extended to your family, Susi and Carl, who were always so kind when I was around.

I would also like to take the chance to thank Dr. Alexakis for receiving me in Paris, despite not really knowing me in beforehand. Our technical discussions influenced significantly the final form of my research. I would like to thank the other committee members as well for providing meaningful feedback to this book.

Starting upstairs in HSL 1.01, the different generations deserve separate words. To the older generation, Martin, Zeno, Rakesh, Shaafi, Wouter and Bepe, I can say that it was comforting to have you guys around to share the struggles and the small victories. To the younger ones, Sagar, Jordi, Luis, Allesandro, David, Mohamad, Gabriel, Weibo, Varun, Constantin, Xiadong, Christoph, Jun, Edoardo, Alex and Yi, thanks for the relaxing moments and for our extended lunch discussions on all kinds of topics. Luis and Tjana, thanks for the close friendship especially in the past months.

Going downstairs to the ground floor, I would like to thank Colette, the unofficial lab head, and also Nancy for making the life of the PhD-Council much easier. I would also like to thank all staff members. Our interactions, whether around the coffee machine or not, were also appreciated.

One more floor down, towards the basement, and I remember to thank Matthias and Arun. I hope I was of help to you during your Master's thesis. Thanks for letting me have my first experiences as a supervisor.

Now, leaving the HSL and crossing the street, first with a stop in *de Atmosfeer*, I would like to thank Daduí, Johan and Marsil, those few (or not so few) beers made this journey lighter. I always knew you guys had the keys to that place.

Entering the main building, I remember Fabrício and Pedro and their valuable friendship. Thanks and hope to see you guys soon. Also thanks to Marc and Jeffrey

for teaching me that Saturn has 82 moons. And of course I cannot forget to mention the old and new members of the PhD-Council. It was definitely rewarding to be part of this group. Here, a special mention to Inés. Our coffee breaks driven by complaints about whatever stood in front of us were just therapy — thank you!

Cycling home and passing by the tennis courts, I am reminded of Davide. Our tennis matches followed by reflections about life and its meaning have a special place in my memory. Sorry for not being able to put up a game at your level. Next time, please do not make me volley. This way I might stand a chance!

And a quick detour passing by the LSL reminds me of the many funny moments with Alberto, Theo and Jacopo. Thank you guys.

Arriving in the city center, a warm thanks goes to Floor and Freek, with whom many Sundays were spent exploring different parts of the city, although we often ended in the same place. Thanks again for embracing an outsider which after these years can still not properly read a menu in Dutch. Sorry Floor, but I will always have to ask: What is actually *tosti Doerak*? And thanks to Aline and Amaury, but please do not invite me for afternoon coffees anymore. You know how it ends.

Finally at home, Michal and Marta, it was a pleasure to have shared the flat with you. I would like to especially thank Marta for the friendship and for the relaxing dialogues. Your cheerful approach to life is contagious.

Outside Delft, a few words must be reserved for my dearest friends from Karlsruhe. Chris, Yoshi, Michael and Agathe, I was certainly recharged and motivated after each of our encounters. Thanks for reminding me what research is about and for being such idealists.

Finally, the last words are reserved for my closest ones. My parents Maria Alexandrina and Reynam, and my sister Morgana, thank you for your constant support and love. My life partner Hanna, thank for your trust.

Tiago Pestana
July 27, Stockholm

About the Author

by Hanna Virtanen

Tiago Cabral Santos Pestana was born in the sunny beachside Brazilian city of Salvador, Bahia the same year walls in Europe were torn down. Early on, Tiago showed to be curious and driven by understanding the (yet for him) unknown. This led him to pursue a degree in mechanical engineering, although he often says he should have studied either computer science or physics.

Tiago received his Bachelor's degree in Mechanical Engineering at the Federal University of Bahia (Brazil) in 2011, with his final thesis project being awarded the national prize by the *Euvaldo Lodi Institute*. His curiosity for different topics in life, cultures and languages led him to fledge away from his hometown. First to Germany, when he was awarded a scholarship from a European-Brazilian consortium to spend one year of his Bachelor's at the Technical University of Munich, and then later to Karlsruhe, where he obtained his Master's degree in Theoretical Mechanical Engineering in 2015 from the Karlsruhe Institute of Technology with majors in fluid mechanics and thermodynamics — for his Master's thesis he was awarded the *Ehrensenator-Huber-Preis*. Following his experience in Germany and in order to further satisfy his curious vein, he moved to the Netherlands to pursue a PhD at the Technical University of Delft.

Outside of academia Tiago enjoys sports in general, especially tennis and football, reading, talking and traveling.

Scientific Contributions

Journal Articles

4. Pestana, T., Thalhammer, M., & Hickel, S. 2020 Inertia-Gravity Waves Breaking in the Middle Atmosphere at High-Altitudes: Energy Transfer and Dissipation Tensor Anisotropy. *Journal of the Atmospheric Sciences* **(in press)**

3. Pestana, T. & Uhlmann, M. & Kawahara, G. 2020 Can preferential concentration of finite-size particles in plane Couette turbulence be reproduced with the aid of equilibrium solutions? *Physical Review Fluids* **5** (3), 034305

2. Pestana, T. & Hickel, S. 2020 Rossby Number Effects on Columnar Eddy Formation and the Energy Dissipation Law in Homogeneous Rotating Turbulence. *Journal of Fluid Mechanics* **885**, A7

1. Pestana, T. & Hickel, S. 2019 Regime transition in the energy cascade of rotating turbulence. *Physical Review E* **99** (5), 053103.

Conference Proceedings

5. Hickel, S., Gnanasundaram A. K., & Pestana, T. 2019 A One Equation Explicit Algebraic Subgrid-Scale Stress Model. *International Symposium on Turbulence and Shear Flow Phenomena* Southampton, UK.

4. Gnanasundaram A. K., Pestana, T., & Hickel, S. 2019 A Priori Investigations into the Construction and the Performance of an Explicit Algebraic Subgrid- Scale Stress Model. *International Symposium on Turbulence and Shear Flow Phenomena* Southampton, UK.

3. Pestana, T.& Hickel, S. 2018 Linear Growth of Columnar Eddies in Forced Rotating Homogeneous Turbulence: a Convergence Study. *European Fluid Mechanics Conference* Vienna, Austria.

2. Pestana, T., Thalhammer, M., & Hickel, S. 2018 Energy Transfer and Dissipation Tensor Anisotropy in Atmospheric Turbulence. *Engineering Turbulence Modelling and Measurements* Montpellier, France.

1. Pestana, T. & Hickel, S. 2017 Confinement Effects on the Inverse Energy Cascade in Homogeneous Rotating Turbulence. *Direct and Large-Eddy Simulation*, Pisa, Italy.

TU Delft
ISBN 978-94-6366-306-9